

AD-755 475

A HOLOGRAPHIC AND ACOUSTICAL INVESTIGATION  
OF A PLATE VIBRATING UNDERWATER

Rudolph E. Croteau, Jr.

Naval Underwater Systems Center  
Newport, Rhode Island

24 October 1972

DISTRIBUTED BY:

**NTIS**

National Technical Information Service  
U. S. DEPARTMENT OF COMMERCE  
5285 Port Royal Road, Springfield Va. 22151

AD 755475

# A Holographic and Acoustical Investigation of a Plate Vibrating Underwater

RUDOLPH E. CROTEAU, JR.  
*Submarine Sonar Department*



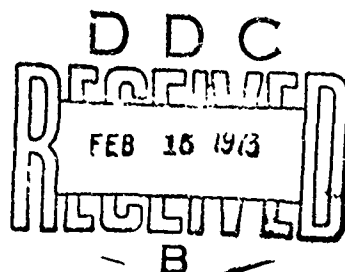
**COLOR ILLUSTRATIONS REPRODUCED  
IN BLACK AND WHITE**

24 October 1972

**NAVAL UNDERWATER SYSTEMS CENTER**

Approved for public release; distribution unlimited.

Reproduced by  
NATIONAL TECHNICAL  
INFORMATION SERVICE  
U S Department of Commerce  
Springfield VA 22151



Vol. (1) to NUSC Ltr. LA152-105

R17

## ADMINISTRATIVE INFORMATION

This study was originally prepared as a dissertation in partial fulfillment of the requirements for the degree of Doctor of Philosophy in Ocean Engineering at the University of Rhode Island. The report was prepared under Task IV of NUSC Project No. A-120-20, "AN/BQQ-5 System Development," Principal Investigator, J. R. Pratt (Code SA1), and Navy Subproject and Task No. S2332-15432, Program Manager, CDR W. Trueblood (NAVSHIPS PMS-385).

ACCESSION for	
NTIS	White Section <input checked="" type="checkbox"/>
E O	Buff Section <input type="checkbox"/>
UNCLASSIFIED	<input type="checkbox"/>
JUSTIFICATION	
BY	
DISTRIBUTION/AVAILABILITY CODES	
Dist.	A.A.L. and/or SPECIAL
A	

REVIEWED AND APPROVED: 24 October 1972

*(C. A. Spero, Jr.)*

**C. A. Spero, Jr.**  
Director of Systems Development

Inquiries concerning this report may be addressed to the author,  
New London Laboratory, Naval Underwater Systems Center,  
New London, Connecticut 06320

UNCLASSIFIED

Security Classification

## DOCUMENT CONTROL DATA - R &amp; D

Security classification of title, body of abstract and indexing annotation must be entered when the overall report is classified

1. ORIGINATING ACTIVITY (Corporate author) Naval Underwater Systems Center Newport, Rhode Island 02840		2a. REPORT SECURITY CLASSIFICATION <b>UNCLASSIFIED</b>	
		2b. GROUP	
3. REPORT TITLE <b>A HOLOGRAPHIC AND ACOUSTICAL INVESTIGATION OF A PLATE VIBRATING UNDERWATER</b>			
4. DESCRIPTIVE NOTES (Type of report and inclusive dates) <b>Research Report</b>			
5. AUTHOR(S) (First name, middle initial, last name) <b>Rudolph E. Croteau, Jr.</b>			
6. REPORT DATE <b>24 October 1972</b>		7a. TOTAL NO. OF PAGES <b>168 172</b>	7b. NO. OF REFS <b>23</b>
8a. CONTRACT OR GRANT NO.  b. PROJECT NO <b>A-120-20</b> <b>S2332-15432</b>  c.  d.		9a. ORIGINATOR'S REPORT NUMBER(S)  <b>4447</b>  9b. OTHER REPORT NO(S) (Any other numbers that may be assigned this report)	
10. DISTRIBUTION STATEMENT  <b>Approved for public release; distribution unlimited.</b>			
11. SUPPLEMENTARY NOTES		12. SPONSORING MILITARY ACTIVITY  <b>Department of the Navy</b>	
13. ABSTRACT  <p>An elaborate experiment was undertaken to determine the interrelationships between dynamic surface deformation (whose data were obtained through optical interferometric holography) and the resulting radiated acoustic pressure pattern. Following analytical derivations and the development of a suitable algorithm, it was concluded that one hologram, by itself, does not contain sufficient information to make accurate predictions of acoustic patterns. Suggestions are made regarding follow-up investigations for the determination of the gradient of the surface deformation.</p> <p>The holographic data were successfully employed in predicting the maximum dynamic bending stresses over the vibrating surface. This technique holds great promise for further application.</p>			

DD FORM 1473

1 NOV 65

(PAGE 1)

S/N 0102 014 6600

UNCLASSIFIED  
Security Classification

UNCLASSIFIED

Security Classification

14 KEY WORDS	LINK A		LINK B		LINK C	
	ROLE	WT	ROLE	WT	ROLE	WT
Optical Holography Underwater Acoustics Plate Vibrations Underwater Dynamic Bending Stress Acoustic-Displacement Interaction						

ib

## ABSTRACT

An elaborate experiment was undertaken to determine the interrelationships between dynamic surface deformation (whose data were obtained through optical interferometric holography) and the resulting radiated acoustic pressure pattern. Following analytical derivations and the development of a suitable algorithm, it was concluded that one hologram, by itself, does not contain sufficient information to make accurate predictions of acoustic patterns. Suggestions are made regarding follow-up investigations for the determination of the gradient of the surface deformation.

The holographic data were successfully employed in predicting the maximum dynamic bending stresses over the vibrating surface. This technique holds great promise for further application.

### ACKNOWLEDGMENTS

The author expresses his appreciation to the many fine people who assisted in this investigation:

To the Long-Term Training Committee, New London Laboratory, Naval Underwater Systems Center (NUSC/NL), which provided the authority and funding that made this investigation possible and the guidance and administrative assistance.

To my major professor, Dr. Herman Sheets, who provided the technical guidance for most of the investigation and oversaw the entire study from its inception to publication.

To Dr. Frederick DiNapoli, a member of the author's committee, who provided guidance for the theoretical acoustics portion of the dissertation.

To Dr. Harold Knickle, another member of the author's committee, who steadfastly followed the investigation and offered advice and assistance through our frequent conversations.

To Mr. Cameron Johnson (NUSC/NL), who provided the technical guidance and assistance for all the holographic studies.

To Mr. Robert Kindl (NUSC/NL), who assisted in the design of the acoustic measurement system and the subsequent analysis of the results.

To Mr. Gerald Mayer (NUSC/NL), who provided administrative assistance in several of the experimental phases.

To my NUSC/NL supervisors: Messrs. Beverly Burnham and Richard Carson and Dr. Howard Schloemer, who provided direct administrative assistance and support.



## TABLE OF CONTENTS

I. INTRODUCTION . . . . .	1
II. DESIGN OF THE EXPERIMENT . . . . .	4
A. Overall Objectives . . . . .	4
B. Design and Construction of the Mechanical Apparatus . . . . .	6
C. Instrumentation . . . . .	13
III. CONDUCT OF THE EXPERIMENT . . . . .	31
A. Initial Holographic Studies . . . . .	31
B. Acoustic-Holographic Experiment at the Water Tower . . . . .	39
C. Comprehensive Investigation of the Various Plate Resonances . . . . .	44
D. Broad Spectrum Acoustic Measurement of the Radiating Surface . . . . .	51
IV. ANALYTICAL PREDICTION OF THE ACOUSTIC PATTERN USING A HOLOGRAPHIC INPUT . . . . .	58
A. Introductory Remarks . . . . .	58
B. Converting the Holographic Data into Displacement . . . . .	58
C. Predicting the Acoustic Pressure at an Arbitrary Point in the Far Field . . . . .	67
D. Development of the Algorithm . . . . .	73
E. Comparison of the Predicted and Measured Patterns . . . . .	83
V. WHY AN OPTICAL HOLOGRAM WAS INSUFFICIENT FOR ACOUSTIC PREDICTION . . . . .	85
A. Monopole Patterns at Dodge Pond . . . . .	85
B. Equivalent Plane-Wave Motion . . . . .	89
C. Fresnel Diffraction Region . . . . .	95
D. Monopole Domination of the Far-Field Patterns Over-rides the Holographic Contribution . . . . .	98

VI. ANALYTICAL PREDICTION OF THE DYNAMIC BENDING STRESSES IN THE PLATE . . . . .	101
A. Introductory Remarks . . . . .	101
B. Stress Prediction Along a Bar with Known Displacements . . . . .	102
C. Development of the Algorithm . . . . .	105
D. Analysis of Results . . . . .	109
VII. CONCLUSIONS . . . . .	112

#### APPENDICES

A. Details of the Measurement Sphere . . . . .	115
B. The Holographic Fringe Data Corresponding to Row 5 . . . . .	117
C. FORTRAN IV Listing, "Prediction of the Far-Field Acoustic Pattern of a Vibrating Source Using a Holographic Input" . . . . .	119
D. FORTRAN IV Listing, "Calculations of the Maximum Bending Stresses Through Any Desired Horizontal and/or Vertical Sections of a Vibrating Plate, Using a Holographic Input" . . . . .	123
E. References Cited . . . . .	127

## LIST OF TABLES

Table	Page
1. Tape Recorder Inputs . . . . .	27
2. Modal Frequencies for a Clamped-Edge Plate Vibrating in Water at 68°F . . . . .	49
3. Shift in Resonant Frequencies due to Change in Water Temperature . . . . .	51
4. Relationship Between Dark Fringe Number, Root of the Bessel Function, and Displacement . . . . .	66

## LIST OF ILLUSTRATIONS

Figure	Page
1. Sound Box on Tripod at Bottom of Water Tower . . . . .	129
2. Rotator on Drawbridge at Top of Water Tower . . . . .	129
3. Looking Down Into the Water Tower . . . . .	130
4. Electronic Instrumentation . . . . .	130
5. Portion of the Acoustic Instrumentation . . . . .	131
6. Remaining Portion of Instrumentation . . . . .	132
7. Raw Acoustic Data . . . . .	133
8. Time-Filtered Acoustic Data . . . . .	133
9. (5, 5) Mode, 9240 Hz, Obtained at the Water Tower . . . .	134
10. Laboratory Holography Arrangement . . . . .	135
11. Laboratory Holography Arrangement, as Viewed From Above . . . . .	136
12. View of Radiating Surface as Seen Through the Photographic Plate Holder . . . . .	136
13. Details of Drag and Kiting Angles . . . . .	137
14. Water Tower Holography Arrangement, Outside of the Tower . . . . .	138
15. Laser Illumination of the Radiating Surface . . . . .	138
16. Laboratory Holographic Studies Using Sound Box Excitation . . . . .	139
17. Real-Time Holographic Investigation, (3, 3) Mode . . . .	139
18. (3, 3) Mode, 3195 Hz, Obtained in the Laboratory . . . .	140
19. Resonance Determination Using Fiber-Optic Probe . . . . .	141
20. (2, 3) Mode, 2633 Hz, Obtained in the Laboratory . . . .	142

Figure	Page
21. (4, 2) Mode, 2677 Hz, Obtained in the Laboratory . . . .	143
22. Plate Modal Frequencies, 68°F . . . . .	144
23. Comparison of the Acoustic Patterns Obtained from the Water Tower with Those Obtained at Dodge Pond . . . . .	145
24. On-Axis Acoustic Pressure . . . . .	146
25. On-Axis Acoustic Pressure Continued . . . . .	147
26. Far-Field Test, 1731 Hz . . . . .	148
27. Far-Field Test, 9240 Hz . . . . .	149
28. General Shape of $J_0(\alpha)$ and $J_0^2(\alpha)$ . . . . .	150
29. Displacement Versus Fringe Number . . . . .	151
30. Radiation from a Piston Set in a Plane Wall . . . . .	152
31. Location of Points P and Q . . . . .	153
32. Resolution of the Vector R . . . . .	154
33. Resolution of the Vector $d\phi$ . . . . .	155
34. Comparison of the Acoustic Patterns Predicted from the Holographic Data with those Predicted by Plane- Wave Behavior of the Radiating Surface . . . . .	156
35. Details of the Sound Box . . . . .	157
36. Geometry of $\beta_1$ , $\beta_2$ , and $\beta_3$ . . . . .	158
37. Bending Stress Across Row 24 . . . . .	159
38. Bending Stress Down Column 34 . . . . .	160

## I. INTRODUCTION

The interaction of vibration, noise and sound has recently become of substantial interest. Holographic techniques permit studies of this interaction in both air and liquids on an experimental basis. The radiation of sound from complicated structures such as ship hulls and sonar baffles is of obvious importance to the U. S. Navy. The mathematical prediction of this sound is extremely complicated, usually requiring gross assumptions of boundary conditions, source distributions, and other influencing factors. As a result, only the rather simple geometric forms with idealized excitations have been completely solved. It is the purpose of this research to implement the use of a modern measurement tool, optical interferometric holography, to provide accurate real-world data on surface displacement for a vibrating plate excited through a fluid coupled system, and to predict from this data the far-field acoustic pressure pattern. The experimental data are presented and are compared with predicted estimates using modifications of the most applicable equations.

Since there is no published information on this topic, the necessity of making either simultaneous or consecutive holographic and acoustic measurements on the same source with all parameters held constant became of paramount importance. Fortunately, another Naval experiment was to be performed within a few months at the huge (100-foot-high by 50-foot-diameter) water tower at the Naval reservation in White Oaks, Maryland, the only known location where sequential

acoustical and holographic measurements could be performed. The investigator was allowed to "piggy-back" on this higher priority experiment. This arrangement optimizes Naval research funding, but places severe restrictions on the secondary investigation. This investigation had to be very carefully planned and constructed, with emphasis on reliability, because the investigator was given only two days to perform his experiment! Calibration of the electronic instrumentation and cable dynamics did not interfere with the priority investigation; thus, these preliminaries were performed during the week preceding the two days of final calibration, holographic investigation, and acoustic measurement.

This dissertation will cover in detail the experimental design and its governing rationale. One of the most important decisions was the design of the sound source. The surface of investigation was purposely selected to be a clamped-edge 6-inch by 9-inch rectangular plate, which could be analytically divided into 3149 square elements.

That portion of the field of holography will be discussed which is required to make interferometric holograms and to analyze their results.

An algorithm, programmed in FORTRAN IV, is developed to predict the acoustic patterns based upon holographic (or other displacement) information. It was necessary in this derivation, and in other parts of this dissertation, to modify basic equations previously developed for circular transducers, inasmuch as similar equations were not available for square-shaped radiators.

Other portions of the research show the results of an in-depth eigenvalue (natural frequency) determination for the

vibrating surface using holography.

Comprehensive acoustic investigations at the NUSC/NL Dodge Pond acoustic calibration facility demonstrate the validity of the acoustic measurements made under remote control at the water tower. They also show that the sound source being investigated behaved like a monopole radiator throughout the frequency range of 200 through 12,000 Hz. This result was unexpected since both dipole and quadripole radiation had been expected at certain eigenvalues. An extensive analytical investigation revealed the probable reason why this occurred and also why the predicted acoustic patterns using holographic input data did not compare with the actual measured patterns.

In order to support assumptions made in the section on hologram interpretation, an algorithm was developed to predict the maximum dynamic bending stress at any point on the vibrating surface, using the holographic data. The results are highly encouraging. Accuracy assessments show the calculated data to be as accurate as conventional techniques which yield only single-point information.

Suggestions are made for follow-up investigations in the acoustic-holographic area involving the determination of the gradient of surface displacement.

The stress-holographic area is very promising, and its use could open the doors to many experiments which, until now, were hindered by thermal gradients and other physical constraints.



## II. DESIGN OF THE EXPERIMENT

### A. Overall Objectives

The radiation of acoustic energy from vibrating surfaces is a subject of intensive investigation in many sectors of the scientific community. Aerospace technology has brought significant advances in the study of vibration. It is now possible to measure the amplitude and spectrum of vibrating surfaces by use of laser interferometry (1), without disturbing that surface with other physical attachments. Research in underwater sound propagation has prompted the development of advanced mathematical techniques for the prediction of the far-field acoustic patterns radiated by vibrating objects based upon knowledge of their near-field pressure distributions (2). It is the premise of this dissertation to investigate the possibility of predicting these far-field patterns based upon knowledge of the near-field displacement information available through optical holographic interferometry. Since no theoretical or empirical information could be found in the literature regarding the use of this modern measurement tool for the solution of the long-standing acoustic problem, considerable care was required in the design of this largely experimental study.

In order to investigate the adequacy of holographic information for the determination of far-field acoustic pressures, several experimental constraints became evident. Primarily, the holographic and acoustic measurements must be made either concurrently or sequentially with no changes made to the experimental apparatus between the

two sets of measurements. This would guarantee against aliasing the data due to the introduction of unexpected variables. Secondly, the radiating surface to be investigated should be two-dimensional so that one hologram could sufficiently describe all motion on the surface. Three-dimensional radiators would require several holograms to completely describe all motion. To do this would require moving the radiator with respect to the laser, thus violating the first constraint. Also, the radiating surface must be small enough, and its operating frequency high enough, to allow the hydrophones to be placed in the acoustic far field, but still within the confines of the water tower (100 feet high by 50 feet in diameter). Lastly, to obtain clear holograms, it is imperative that there be almost no relative motion between the laser and the base-plane of the radiating surface.<sup>1</sup>

The holographic measurements were made according to the technique used by Johnson and LeBlanc (3). A heavy optical table of granite and steel pipe was firmly placed on the concrete apron which surrounds the outside of the 100-foot-high water tower at its base. The laser and other pieces of optical instrumentation were arranged on this polished surface at the proper height to allow the laser beams to pass through some portholes in the tower wall and illuminate the radiating surface. This surface, pointed toward the portholes, was supported on an 8-foot-high tripod of heavy steel pipe, whose feet were firmly implanted at the center of the bottom of the tower. Since the tower diameter is 50 feet, the distance between the laser and the object was slightly less than 30 feet. The holographic

---

<sup>1</sup>In this experiment, relative motion in the order of .00001 cm could cause fringe smearing.

procedure will be described in detail in section III.

When a satisfactory hologram was obtained, the acoustic pressure was accurately measured in the far field over a sphere of 8-foot radius, the center of which coincided with the center of the radiating surface. Thus, all acoustic energy leaving the radiating surface was measured. The acoustic measurement technique was carefully developed to avoid creating currents in the water (which might cause relative motion) and to provide an exact description of the three-dimensional pressure pattern radiated by the surface.

The limited time available to prepare this experiment required maximum utilization of equipment, instrumentation, and techniques that were readily available, and of proven reliability. Whenever special apparatus was built for this experiment, off-the-shelf components were used extensively to minimize machining and assembly time.

#### B. Design and Construction of the Mechanical Apparatus

As was stated previously, the radiating surface must be two-dimensional and small enough in size to allow for accurate far-field acoustic measurements to be made within the 50-foot-diameter tower. Since the tripod (constructed for another experiment) was 8 feet high and spherical acoustic measurements were desired, then an 8-foot radius sphere seemed appropriate. Peterson and Gross (4) indicate that the far-field (spherical spreading) condition can be assumed for finite sized radiators when:

$$R \geq 4D \quad (1)$$

where  $R$  = radius of test sphere

$D$  = largest (diagonal) dimension of the radiator.

Since  $R = 8$  feet (2)

then  $D \leq 2$  feet. (3)

A clamped-edge rectangular plate was chosen as the radiating source. The overall frontal dimensions were 10 inches by 13 inches (16.4-inch diagonal).

In order to ascertain that clear holograms would be obtained (low relative motion between the optical bench and the radiating surface base-plane) a heavy steel ring was utilized to clamp the edge of the radiating section on all four sides. To maximize its strength, this rectangular ring was cut from a single piece of steel plate, 2 inches thick, and then the center portion was milled out to yield a 6-inch by 9-inch opening. This relative 2 by 3 configuration would ensure complicated modal patterns across the vibrating surface. It is the complicated radiators which cannot easily be handled using standard analytical techniques. To this heavy monolithic frame, the radiating surface was attached by means of epoxy glue. The center portion of this surface (6 inches by 9 inches) was free to vibrate, but the edges were held securely (as proven by the holograms) providing the necessary base-plane.

How to excite the radiating surface was the next major problem. It could be driven by an electromechanical "shaker" mounted inside a sealed air cavity in back of the plate. The design, procurement, and testing of such a cavity could not possibly be accomplished in the given time span. It is quite easy to excite plates underwater by acoustic methods, i.e., using a transducer in the water behind the plate; but, it would be impossible to separate that component of the far-field acoustic pressure coming from the

radiating surface from that coming directly from the transducer. Clearly, a baffle could be placed around the plate. Unfortunately, for the expected high frequency to be used (8 kHz to 10 kHz) the baffle would have to be constructed of approximately 5-inch-thick lead or 9-inch-thick steel plating! The weight and design of the support structure for such a baffle were obviously prohibitive.

The excitation method selected was to place a small, thick, heavy, non-vibrating box around the transducer and bolt the plate-ring combination to its open front. The box would be free-flooding to allow for acoustic coupling from transducer to water to plate. Care was taken in the design of the box to force the acoustic energy to leave the cavity through the thin (0.125-inch) radiating plate rather than through the other five sides of the parallelepiped. Figure 1 shows the box (white) with the plate-ring (gold) bolted to its front and sitting on the black steel tripod at the bottom of the water tower. The box is tilted upward in the direction from which the laser beams will come through the portholes. Additional portholes and depth markings can be seen on the far side of the tower.

The exterior surface of the box was constructed from 0.5-inch steel plate continuously welded on all seams creating a very stiff structure. After extensive surface preparation, including the use of special primers and adhesives, the interior surface was covered with Lord XLD-500 Damping Tile. This viscoelastic material (1 inch thick) converts a large percentage of vibrational energy into heat and thereby reduces the magnitude of the vibrations of the surface to which it is attached. The great weight of this material also serves to mass-load the structure and thereby reduce vibrations even more.

Ungar (5) reported that the efficiency of damping tiles is improved if they are constrained in "sandwich" construction. Therefore, another layer of steel plate (0.125 inch thick) was cemented over the tiles on the interior of the box. Care was taken that these septum plates did not touch each other. A 0.25-inch gap was maintained between adjacent plates to prevent the transmission of vibrations from one plate to another. The entire box was painted with anti-rust paint to prevent discoloration of the highly filtered water in the tower.

An additional provision to reduce box vibration was provided by lining the box with an acoustical mismatch material. Nitrogen impregnated neoprene foam, 0.5 inch thick, was cut to tightly fit inside the damped box. The captured nitrogen bubbles in this foam serve as an effective barrier to the transmission of sound in water. By adding the foam, the amount of acoustic energy reaching the septum plates was greatly reduced, compared to that which impinged on the 6-inch by 9-inch radiating "window."

The plate-ring was bolted to the box with six cap screws (0.375-inch diameter), which were tightened into tapped holes in steel bars welded at the mouth of the box. By cutting the foam material to be slightly longer than necessary, the foam was compressed upon tightening of the bolts and served as an acoustic seal between the box and the plate-ring face. Lifting eyes were screwed into the top and three leveling screws were provided on the bottom of the box. The latter prevented any rocking of the box on the tripod. A Masra AN/SQS-23 type transducer was located in the box, with its cable coming out through a hole in the back. "Scotchlite" reflective tape was cemented to the radiating surface and to one side and the top of

the box. This tape has the appearance of a movie screen and greatly enhances the hologram brightness.

As can be seen from the above descriptions, several acoustic techniques involving the most modern materials have been utilized to maximize sound radiation through the 6-inch by 9-inch "window" while simultaneously reducing the radiation of acoustic energy from the other five sides of the box. This design permits the accurate holographic recording of the radiating surface displacement and minimizes the contamination of the resulting acoustic energy by vibrations from other sides of the box.

There are many techniques that can be used to measure the three-dimensional acoustic pressure pattern coming from a finite-sized radiating device. All of these techniques require taking the measurements in the far field over an imaginary surface of known geometry, the simplest of which being a sphere. One could obtain a spherical pattern by using many hydrophones positioned in the centers of equi-area segments on the sphere. Obviously the support structure to hold these hydrophones, as well as their cost, availability, and differences in sensitivity, would preclude such a technique. To reduce these latter problems, the optimum choice is to move a single calibrated hydrophone over the measurement surface in such a manner that its position, relative to the radiating device, is always precisely known.<sup>2</sup>

Since an accurate and reliable polar recorder was available,

---

<sup>2</sup>This approach is applicable only for time-invariant experiments, a condition which was assumed and subsequently monitored throughout the measurement phase.

it was decided to describe the three-dimensional pressure pattern by using an ensemble of two-dimensional polar plots. The sphere was divided into many (either 17 or 33) horizontal slices similar to the parallels of latitude on the globe. The top and bottom patterns, corresponding to the poles on the globe, are single point measurements. All other patterns are generated by rotating the hydrophone about the vertical axis through the sphere, with a radius ( $\Delta r$ ) and a height ( $\Delta h$ ) either above or below the equator such that the hydrophone travels along the surface of the 8-foot measurement sphere. Each of these polar patterns, which are called "contours" of the sphere, was made at equi-spaced  $\Delta h$ 's such as every foot or every half-foot. For each value of  $\Delta h$ , there is a particular value of  $\Delta r$ . That contour which corresponds to the equator of the sphere (i.e.,  $\Delta h = 0$ ,  $\Delta r = 8$  feet) lies in the same horizontal plane as the center of the radiating surface. All other contours are parallel to the equator; a positive  $\Delta h$  denotes a contour above the equator, a negative for one below the equator. Appendix A graphically describes the measurement sphere and contains a table listing the  $\Delta h$ 's and their respective  $\Delta r$ 's.

An adjustable rotator was designed and built for this experiment in order to move the hydrophone along any desired contour, at a smooth and controlled rate. Since the rotator had to be placed above the water (to minimize currents in the tower) it was necessary to suspend about 100 feet of cable from the rotator arm to the small LC-10 hydrophone. To minimize the problems caused by cable dynamics (i.e., drag angle and "kiting") the rotator was designed to make one revolution in 4.25 minutes. This very low speed allowed the hydrophone to act much like a simple plumb bob when the cable was weighted



with lead and copper pipe. At this speed, the moving hydrophone behaved in an orderly fashion with a  $12^\circ$  drag angle and no "kiting." The term kiting is taken to mean the tendency of the hydrophone to circumscribe a circle of radius different than the radius at the driven end of the cable. Details of the in situ determination of the cable dynamics will be covered in section III.

The rotator consists essentially of a heavy motor-driven vertical shaft to which a lightweight 10-foot arm is horizontally attached. The hydrophone cable passes through a long slot in the arm and over a carriage which secures it. The carriage, in turn, can be clamped anywhere along the arm, thus providing for rotation of the hydrophone cable through any desired radius up to 8 feet. Figure 2 and figure 3 show the rotator clamped to the end of the "drawbridge" that extends over the center of the surface of the water tower. The heavy, 2-inch-diameter steel shaft is held in position by thrust bearings mounted on the top and bottom of an open-sided welded steel box. Rotation of the shaft is provided by an ac induction motor driving a double worm-gear speed reducer. The output of the reducer is connected via chain drive to a large sprocket. A simple positive engagement clutch couples the sprocket to the vertical shaft. This clutch was formed by mounting short steel pins into the top of a steel ring clamped to the shaft. The sprocket hole was slightly over-bored and, when engaged, the sprocket would lie on the ring. Torque is transmitted to the steel pins via matching holes in the sprocket. The close-up photograph, figure 3, also shows the 60 Hz synchro attached to the top of the shaft. This synchro drives a matching servomechanism in the polar recorder. Also visible is a small arm, clamped to the

side of the box. A microswitch is mounted on the end of this arm. At a certain angle of rotation the switch rides over a magnetic bar riding on the sprocket providing start-stop indications for the instrumentation. A close inspection will reveal the small black hydrophone cable passing over the brass carriage at the end of the arm. The white marks on this cable are spaced 1 foot apart providing the  $\Delta h$  information. Two large planks were bolted to the bottom of the rotator box. These planks, in turn, were clamped to the end of the drawbridge using threaded rods through cross pieces above the planks and below the drawbridge.

The rotator performed flawlessly throughout the experiment, thereby proving the reliability of the massive, off-the-shelf component design. The radiating box, sitting on the tripod at the bottom of the tower, performed its intended task by providing a measured 23 dB reduction in acoustic energy from the front to the back. This corresponds to an energy ratio of 200 to 1. The decibel (dB) method of measurement will be treated in detail in the next subsection.

### C. Instrumentation

In the free-field measurement of acoustic power, continuous excitation of the source is possible since all energy transmitted leaves the measurement sphere and none comes back into it. When the measurement must take place in water with adjacent reflecting boundaries (air, sand, steel, etc.), care must be taken to measure only that energy which leaves the measurement sphere. Pulse techniques have been developed which discriminate against reflected sound by taking advantage of the time differential between the direct and

reflected energies received by the hydrophone. A brief verbal description of pulsed systems in general and their important parameters will be presented first. The actual measurement system employed at the water tower will be detailed in the remaining portion of this subsection.

The essential items in any pulsed system are a keyed transmitter, a gated receiver, and a timing generator that coordinates the opening of the receiver gate based on the time since the last transmitted pulse. Usually, the duration of transmitted pulse, the pulse repetition rate, and the opening and closing of the receiver gate are all separately controllable. The pulse duration is usually determined by the pulse frequency, the excitation method, the type of energy detector, and the nearness of reflecting surfaces. Most detecting instrumentation needs at least 10 cycles of oscillation to function accurately. At the common frequencies of 1000, 5000, and 10,000 Hz, this corresponds to 10, 5, and 1 msec, respectively. Often, the excitation source requires a few cycles of oscillation before it stabilizes at a uniform magnitude. (This condition existed for the transducer-box plate combination used in this experiment and will be further discussed within this subsection.) The nearness of the reflecting surfaces usually limits pulse duration. It is desirable to stop transmitting before the first portion of the reflected energy arrives at the hydrophone. This provides a clearly discernible interval between the direct and reflected pulses. These same surfaces control the pulse repetition rate. It is desirable that all of the reflected energy be absorbed, scattered, or otherwise diminished before the next transmitted pulse begins. In the water tower, the

energy seen by the hydrophone due to a single pulse 6 msec pulse decayed exponentially and was undetectable after 250 msec. A pulse repetition rate of 1 per second was selected in this instance.

The receiver gate, controlled by the timing generator, is usually adjusted to "open," i.e., to allow energy to be measured, only after the initial pulse transients have subsided. The gate is "closed" before the transmitted pulse ends to avoid the shut-off transients which are normally quite extended. It would be reasonable, for example, to measure only the middle 3 msec of a 5 msec pulse. The timing generator also keys the transmitter at the desired repetition rate and pulse duration.

The complete instrumentation system used in this experiment was composed of several interdependent subsystems: pulsing, measurement, position control, calibration, and automatic data reduction. Most of the system is shown in figure 4. The unit resting on the wooden box on the left is the precision polar recorder. A 7-channel AM-FM tape recorder is shown on a table between the two racks. The light green units in the middle of the first rack are the heart of the system, the acoustic pulsing equipment. Figure 5 and figure 6 provide the details for the interconnection of most of the system components. For clarity, power supply and tape recorder connections have been omitted from these diagrams. The tape recording will be covered in detail later beginning on page 26.

The following description of the pulsing subsystem shown in figure 5 starts at the point of the acoustic data input, the Atlantic Research LC-10 hydrophone at the top left corner. This is the hydrophone that is made to travel over the measurement sphere. The

zigzag in its cable indicates considerable line length (approximately 140 feet). The data input shares a two-position switch with the calibration input that will be discussed on page 23. In normal operation the hydrophone can be considered to be, essentially, directly connected to an adjustable gain Ithaco "low-noise" preamplifier. This type of ac amplifier was developed especially for the accurate processing of low voltage signals coming from capacitive sources such as hydrophones.

The output of this amplifier appears at test point 1 (TP 1). If the oscilloscope in the center of figure 5 is connected to TP 1, the oscillogram shown in figure 7 will result. The oscilloscope is triggered concurrently with the initiation of transmitter keying. Approximately 1.7 msec later (within 3 percent of the time it takes for acoustic energy to propagate 8 feet in fresh water at 20°C), the first oscillations can be seen at the left of the first large burst of energy. Within a few cycles, this energy builds up then peaks and levels out at a fairly constant value for about a 2-msec period. It then begins to rise a little (possibly due to constructive interference from the bottom of the tower) peaking and then decaying slightly until the pulse is turned off. Total pulse duration is a little more than 6 msec. A lengthy decay transient can be observed between the end of the transmitted pulse and the arrival of the first major reflection (the other large burst of energy). This first major reflection occurs roughly 11.5 msec after the start of pulse transmission. This corresponds to a two-way travel distance of about 50 feet, and therefore it must have been reflected from the tower wall 25 feet away. It should be noted that the reflected energy is only 1.4 dB lower than the direct

arrival. This indicates near-perfect reflection from the walls, i.e., almost no absorption there and, moreover, the focusing effect of the walls. For simple spherical spreading, the intensity of the acoustic pressure would be expected to diminish by about 7 dB over the 40 feet of additional travel distance. These high-strength reflections clearly demonstrate the need for pulse-type measurements within enclosed test environments. Once the pulse system parameters were fixed, oscillograms such as those seen in figures 7 and 8 would be reproduced exactly the same pulse-after-pulse. Whatever physical phenomena were occurring did so in the same fashion for every transmitted pulse.

As was stated earlier, it took about 250 msec before the reverberations, i.e., reflected pulses in the tank, decayed to acceptable levels. The most likely eventual sink for the transmitted acoustic energy was the mud at the bottom of the tower. This long decay time (250 msec) is equivalent to 1200 feet of acoustical energy propagation. The pulses could bounce back and forth from top to bottom of the tower 6 times in this duration. These vertical oscillations are initially set up by the horizontal reflections and reflections impinging on the tripod (and thereby causing energy scatter), and by the initial beaming of the acoustic energy upward at  $10^\circ$  from the horizontal (the upward orientation of the box can be seen in figure 1). This upward beaming causes the reflected pulse to bounce back and forth in zigzag fashion up the tower, gaining about 9 feet in height for each crossing of the 50-foot diameter. It is expected that all normal modes of this closed acoustic cavity (the water tower) were excited within the first 100 msec.

Figure 7 clearly indicates the energy contamination in our

measurement environment. Steps must now be taken to time-domain filter all of the energy to yield only that portion which is believed to come solely from the radiating surface. This function is performed by the Scientific-Atlanta (S-A) receiver gate, the next component in the pulsing system. Triggering information from the S-A timing generator allows this "gate" to open only for a brief instant and then close again. The receiver gate, like many other pieces of sophisticated electronic equipment, operates with maximum accuracy and minimum distortion only when its output terminals are connected to a specified impedance. Scientific-Atlanta has designed these particular units to match a  $75 \Omega$  resistance; therefore, this load was placed across the output terminals of the receiver gate. The gated output appears at TP 2 and is shown in the oscillogram in figure 8. It is important to note that no changes in oscilloscope settings were made between figures 7 and 8. Both traces started with the initiation of a transmitted pulse. Figure 3 shows that the receiver gate opened for only 1 msec, and that this duration coincided with the 2-msec period of constant value which was reached in figure 7 after the start-up transients subsided. This small portion of the original transmitted pulse will be the only acoustic energy measured from this point on. When the hydrophone was held stationary, as well as the transmitter pulse parameters, the oscillogram seen in figure 8 was exactly duplicated once every second.

The timing generator (near the center of figure 5) controls the entire pulsing sequence. Within this unit are located the controls for adjusting pulse repetition rate, pulse duration, and the receiver gate opening and closing. Auxiliary outputs provide for

synchronizing the oscilloscope triggering with the initiation of a transmitted pulse. Other portions of the pulsing subsystem include the generation of a precisely controlled pulse that is subsequently amplified and sent to the Massa AN/SQS-23 type transducer element located in the box at the bottom of the tower. Pulse generation begins at the Hewlett-Packard (H-P) oscillator (shared with the calibration subsystem). For calibration purposes the oscillator output is held at 1.00 Vrms and at the desired pulse frequency as shown by the counter. This signal passes through the S-A transmitter gate only as long as the triggering information from the timing generator persists. It will be noted that this type of function is identical to that performed by the receiver gate. After passing through a 75  $\Omega$  load the pulse as seen at TP 4 will be a uniform amplitude tone burst of exact duration, e.g., 6 msec, at the desired pulse repetition rate, e.g., 1 pulse per second.

A brief digression is in order at this point regarding the use of the decibel (dB) measurement system. Historically, acoustic measurements have normally been made in logarithmic units, because of the large range of values which are encountered. The usual logarithmic base is "10" rather than the base "e" used by mathematicians. The unit of measurement is the dB defined by Beranek (6) and many others as

$$\begin{aligned} \text{Electrical Power Level} &= 10 \log_{10} \frac{W_1}{W_2} \\ \text{in dB} \end{aligned} \quad (4)$$

where  $W_1$  and  $W_2$  are two electrical powers. If the resistance across which each of these powers is measured is identical, then



$$\text{Electrical Power Level} = 20 \log_{10} \frac{V_1}{V_2} \quad (5)$$

in dB,

where  $V_1$  and  $V_2$  are the voltages across the similar resistances.

It is most convenient to set the denominator as a unity reference value, e.g., 1 Vrms; then

$$\text{Electrical Power Level} = 20 \log_{10} V_1 \quad (6)$$

in dB//1 Vrms.

A similar technique is used in acoustics (for example, Officer (7)) where, in wave propagation through a single media, the two resistances or rather the real parts of the acoustic impedances are the same.

$$\text{Acoustic Intensity Level}^3 = 20 \log_{10} \frac{P_1}{P_2} \quad (7)$$

in dB,

where  $P_1$  and  $P_2$  are the acoustic pressures across the same characteristic impedance again. Using a unity reference value of 1 dyne per square cm (which is identical to 1  $\mu$ bar), we have

$$\text{Acoustic Intensity Level} = 20 \log_{10} P_1 \quad (8)$$

in dB//1  $\mu$ bar.

Throughout this dissertation, voltages will usually be described in dB//1 Vrms and acoustic pressures always in dB//1  $\mu$ bar.

Since making logarithmic adjustments on linear instrumentation such as conventional voltmeters and resistor banks is time consuming and error prone, logarithmic attenuators are used extensively in

---

<sup>3</sup>Intensity is defined as the average energy flow through a unit area perpendicular to the direction of flow.

acoustic measurements. These attenuators will drop the signal value across the unit by any incremental number of dB which might be desired, usually by the setting of two 10-position switches (for changes from 0 to 99 dB). A Davon attenuator was used following the transmitter gate to control the pulse amplitude. For accuracy reasons, a 600  $\Omega$  load is used for impedance stabilization. The tone burst is then cabled to a MacIntosh 200-watt linear amplifier; its gain control set roughly at midrange. The tone burst at the output of this amplifier was maintained at a constant 10.0 Vrms (as seen at TP 5). Rapid reductions of this output voltage in 10 dB steps could be accomplished by changing the attenuator. The 10 volt tone burst was sent down approximately 180 feet of type DSS-3 transducer cable to the AN/SQS-23 transducer element. This completes the operation of the pulsing subsystem.

The measurement subsystem begins at TP 2, at the top-center of figure 5. The signal at this point is the time-filtered acoustic data seen in figure 8. This approximately 1 msec tone burst at 9240 Hz contains about 10 cycles of oscillation. The frequency 9240 Hz was utilized because it produced the best quality hologram at the water tower. A NUSC/NL designed logarithmic amplifier was used to convert this linear ac pulse to another ac pulse whose output is proportional to the logarithm (to the base 10) of the input value. The amplitude of this logarithmic pulse is detected by a conventional Dranetz sampling voltmeter (referred to as the "Pulse Detector" in figure 5), whose sample duration is controlled by the timing generator to be the same width and coherent in time with the logarithmic pulse entering it. The "DC OUTPUT" of this pulse detector is a dc voltage proportional to

the logarithm of the rms value of the time-filtered pulse shown in figure 8. All that remains is to record this value on the B&K polar recorder as a function of hydrophone position. Since this string of measurement instrumentation was not designed by their individual manufacturers to be compatible in this configuration, it was necessary to add a buffer stage between the pulse detector and the polar recorder. This stage consists of a NUSC/NL designed and produced dc amplifier with a controllable dc bias level at its input to offset the +2 volt dc reference level which is present at the "DC OUTPUT" of the pulse detector even during the absence of signal. The B&K polar recorder was operated in the linear condition. An iterative process involving gradual changes between the recorder's input gain control, and the dc bias level enabled the recorder to be calibrated to match the pre-printed lines on the polar graph paper.

The position-control subsystem provides the information to synchronize the rotation of the hydrophone on a single contour with the rotation of the plotting table on the polar recorder. This was accomplished by means of 60-Hz servomechanisms. A synchro (transmitter) was directly coupled to the heavy rotating shaft. As the shaft rotated the synchrorotor winding relative to the three stationary stator windings, 3-phase, 60-Hz, electrical power was sent from the stator through about 50 feet of cable to a matching servo receiver-motor within the polar recorder. In this manner, the plotting table would follow the shaft motion at any speed and in either direction. Synchro-zeroing, i.e., the initial aligning of the plotting table with a reference shaft position, was accomplished by rotating the synchro housing itself. Once the synchro was zeroed, the housing was held

stationary throughout the remainder of the experiment.

The calibration subsystem will encompass the last few remaining blocks on figure 5. The same H-P oscillator used to generate the transmitted pulse is also used for calibration. This guarantees that, once a transmission frequency has been selected, the entire system will be calibrated using that same frequency. The 1.0 Vrms output of the oscillator is passed through an H-P attenuator and an H-P ac voltmeter and is subsequently substituted for the hydrophone input during calibration, at the input to the Ithaco low-noise preamplifier. To stabilize the oscillator output voltage, some attenuation was always present in the H-P attenuator. In order to calibrate the system, the variable gain control on the Ithaco preamplifier was set at 0 dB, i.e., no amplification and no attenuation. With 10 dB set on the H-P attenuator, the polar recorder's gain control and the dc amplifier's bias control were adjusted to place the recorder stylus on a convenient line near the edge of the polar graph paper. In this case the +35 dB line was selected for ease of calibration. This line would now represent -10 dB referenced to 1 Vrms. Another 10 dB was then added in the H-P attenuator and the stylus moved toward the center of the paper. If it did not fall exactly on another desired preprinted line, the recorder gain control was changed to accommodate this. Unfortunately this would upset the bias level; therefore both controls were adjusted again and again until finally one could step from 10 dB to 50 dB on the H-P attenuator and the stylus would dutifully follow each 10 dB decrease, pausing over the preprinted lines which were to represent 10 dB steps.

This total system calibration does not depend upon knowledge

of nor adjustment of the many controls which lie in the chain between the input and the output. All that is required is that once calibrated, no internal controls need be adjusted. The only exception to this rule was the variable gain control on the Ithaco preamplifier. It had been set to 0 dB during calibration. When the hydrophone was then connected in place of the calibration circuitry, the pulse level was much below -10 dB referenced to 1 Vrms. This caused the stylus to move all the way to the center of the polar paper. Since the hydrophone was in the position of suspected highest acoustic pressures, the Ithaco preamplifier gain was adjusted to place the stylus near the highest calibration line. This gain setting (+30 dB) was recorded on the polar chart and remained constant at that level for the duration of the test. By means of this calibration technique, the following simple formula can be used to determine the exact voltage that must have been present on the hydrophone cable for any particular point on the polar chart:

$$V_C + G_I = L + C, \quad (9)$$

where

$V_C$  = voltage level on the cable in dB//1 Vrms

$G_I$  = gain setting on Ithaco preamplifier

$L$  = level recorded on polar chart

$C$  = calibration factor (-45 dB).

The calibration factor stems from the initial calibration which set -10 dB on the H-P attenuator to correspond with the +35 dB line on the chart. Thus, for this setting,

$$-10 \text{ dB} + 0 = +35 \text{ dB} - 45 \text{ dB}. \quad (10)$$

The calibration factor is strictly a function of an arbitrary input level (-10 dB) and an arbitrary chart position (+35 dB). Once set, however, this factor (-45 dB) is a constant throughout the experiment.

Figure 6 contains portions of the automatic data reduction subsystem. This subsystem was designed to provide for an almost completely independent measurement system to serve as a backup for the primary hard-copy polar recorder output. The backup system could be used to avoid data loss due to any instrument failure in the primary chain. Moreover, if the failure occurred near the end of the chain, e.g., the pulse detector or the polar recorder, that properly processed data at the beginning and midpoints of the chain would also be saved in order to reduce the subsequent processing of data in the backup system. The only common items required for both the primary and backup modes (shown in figure 5) are the adjustable gain Ithaco low-noise preamplifier and the LC-10 hydrophone that was rotated around the sound source. Since neither of these pieces is immune to failure, two spare LC-10 hydrophones and an additional Ithaco preamplifier were on hand during the experimentation. Rather than allowing these "spares" to remain "on the shelf" during the testing, one of the LC-10 hydrophones and the low-noise preamplifier were utilized to monitor the time stationarity of the experiment. This hydrophone (called the reference hydrophone) was suspended from the drawbridge approximately 10 feet from the rotator. The hydrophone was held stationary about 10 feet above the bottom of the tower by a white line tied to a small weight. This line is readily visible in figure 1 on the left side. Close inspection will reveal the small

white spot near the top of the line that is the stainless steel base of the reference hydrophone. Once arbitrarily placed, this hydrophone was never moved throughout the duration of the testing. The gain of the preamplifier was adjusted to give an output pulse amplitude of about 1 Vrms, when the AN/SQS-23 transducer was driven at 10 Vrms. This output (nearly identical to figure 7) was visually monitored, on the oscilloscope, frequently during the test and indicated no change in transmitted pulse level with time.

The heart of the automatic data reduction subsystem, the 7-channel tape recorder, was not shown in figures 5 and 6 to avoid clutter of these diagrams by the many interconnecting cables to the recorder. The alternative method employed was to label all important test points, especially those points where information was recorded. The instrumentation quality tape recorder utilized was an Ampex CP-100. It records and reproduces on seven parallel tracks along a 1/2-inch tape. The user has the option of which recording mode, either direct or frequency modulation (FM), he desires on each channel individually. Each mode has certain advantages. In the FM mode, frequencies as low as 0 Hz, i.e., dc voltage, can be accurately recorded. The highest usable frequency is tape speed dependent and at 30 inches per second, input filters attenuate the signals sharply above 10 kHz. In the direct mode, the lowest usable frequency is about 100 Hz, but its upper limit is 125 kHz. The dynamic range of the FM mode is 45 dB whereas that of the direct mode is only 30 dB. Both modes will record accurately only if their input levels are held to 1 Vrms or less (e.g., in the direct mode, accurate linear response can be obtained from 0.032 V (-30 dB//1 Vrms) through 1.0 Vrms). The

standard 10.5-inch-diameter tape reel contained 2500 feet of 1.5-mil mylar base tape. This quality tape is thicker and more reliable than the standard 1-mil tapes. Operating at a tape speed of 30 inches per second, one reel of tape is limited 15 minutes of recording time. Since one rotation of the hydrophone required 4.25 minutes, three "runs" could be comfortably recorded on each reel.

The recording heads for each channel are divided into two groups; one stack of heads contains channels 1, 3, 5, and 7, and the other stack has channels 2, 4, and 6. The two stacks are physically displaced by 1.5 inches along the tape. This displacement of adjacent channels accounts for the low "cross talk" between these channels. In making pulse measurements, where timing is important, this displacement in space amounted to a 50 msec separation in time. Care was taken to record those items of information where signal synchronization is important, on the same stack. Table 1 indicates what type of information was recorded on each channel, the recording mode utilized, and the test point from which this information was obtained.

TABLE 1  
TAPE RECORDER INPUTS

Channel	Test Point	Mode	Information
1	8	FM	Time Code
2	4	FM	Transmitted Pulse
3	6	Direct	Sampling Frequency
4	1	FM	Received Pulse
5	3	FM	Pulse Detector Output
6	9	FM	Reference Pulse
7	7	Direct	Voice and Start-Stop



Signal synchronization is required between the transmitted pulse, the received pulse, and the reference pulse (from the reference hydrophone); thus, these pulses were recorded from the same stack on channels 2, 4, and 6, respectively. For the planned automatic data reduction using the facilities of the NUSC/NL Computer Laboratory, the beginning of the transmitted pulse would initiate a time-counting sequence which, upon a preset count, would allow the digitizing of the received pulse to begin. Likewise, the digitizing could be stopped at any count. In effect we have computer-controlled time-filtering; the same function is obtained in the pulsing subsystem. Similarly, the time-stationarity of the experiment could be measured and verified by use of the reference pulse.

The rate at which the received pulse is digitized was established by recording a 100 kHz signal on channel 3. This "sampling frequency" was set well above the minimum or Nyquist rate of 2 times the highest frequency to be analyzed (see Deutsch (8)). The use of 100 kHz guarantees at least 10 points per oscillation in the 10-kHz limited acoustic data. This same 100 kHz signal was cabled through a microswitch on the rotating shaft back to channel 7 to provide overall start-stop information for the computer. Before each run, the clutch would be disengaged on the shaft and the arm positioned to a mechanical starting point. After the shaft had rotated at least 90 degrees, by means of the gear drive, the microswitch (shown in figure 6) would close denoting the electrical starting point. The computer, sensing a 100 kHz signal, would then begin the analysis. The switch would remain closed for several seconds then open again. This latter opening would not, however, initiate any

action in the pre-instructed computer. As the shaft made one full revolution past the electrical starting point, the switch would close again causing the computation to be terminated. Since the start-stop information occupied less than half a minute per revolution, channel 7 was also used for voice recording of the run and instrument parameters. Figure 6 shows an Astatic crystal microphone connected to a Burr-Brown preamplifier. This combination produced enough voltage for satisfactory voice recording and instantaneous playback through a small loudspeaker. The loudspeaker could also be attached to the tape recorder output, a useful feature for picking out a certain section of data from the reel during the set-up and calibration phases of the experiment. Since the Burr-Brown preamplifier filters all signals well below 100 kHz there was no possibility for the voice input to trigger the computer "on" or "off." These instructions could only result from the narrowband detection of a few seconds of continuous 100 kHz signal.

The Systron-Donner time code generator shown in figure 6 is the last major piece of instrumentation. Its purpose was to provide a continuous indication of the time of day for use in the automatic data reduction subsystem. The hour, minute, and second are contained in the binary coded modulation of a 1 kHz carrier frequency. The pulse-type modulation occurs at a rate of 100 pulses per second. The particular code employed is of the standard type developed by the White Sands Missile Range (9), Inter-Range Instrumentation Group (IRIG). Format B has been adopted by the Naval Underwater Systems Center and many other facilities. The output of the time code generator was too high for direct input into the tape recorder. A 10-1 resistor pad of "L" configuration was assembled within a small

steel box (to minimize the reception of electromagnetic noise). This pad reduced the output voltage of the time code generator by a factor of 10, thereby placing it within the proper range for recording. This time information would be used by the computer to calculate hydrophone rotation angle in lieu of the synchro positioning information. The electrical start-stop information, the elapsed time, and the constant rotation rate of 1 revolution in 4.25 minutes is sufficient for the precise calculation of hydrophone position. The time code generator provided for the measurement of elapsed time. A similar pad is shown in figure 5 at the output of the pulse detector, and it serves an identical purpose.

### III. CONDUCT OF THE EXPERIMENT

#### A. Initial Holographic Studies

Concurrent with the construction of the mechanical apparatus and the assembly of the electronic instrumentation, a brief investigation was undertaken to find a suitable clamped-edge plate resonant mode between 8-10 kHz. The 6-inch by 9-inch plate has many resonant modes (which will be dealt with in detail later in this section); however, it was necessary to restrict attention at this time to finding a suitable mode high enough in frequency to guarantee far-field acoustic propagation at 8 feet (8 kHz), and yet low enough to be compatible with the tape recorder (10 kHz).

At any arbitrary frequency, one can obtain a hologram of the vibrating surface. Usually, this hologram will be highly complicated, being a combination of two or more resonant modes. Using small (10-20 Hz) changes in the plate excitation frequency, one of these modes will become more dominant. By trial and error, the experimenter can normally close in on this particular resonant mode. Holograms of resonant modes are highly symmetrical about their horizontal and vertical axis.

Figure 9 shows the (5, 5) mode of the 6-inch by 9-inch clamped-edge plate. To interpret this hologram, consider the group of black fringes in the lower left corner. These fringes are analogous to the lines at equal elevation, i.e., contour lines on a topographical map. On such a map the small circular fringe in the center would represent

the top of a mountain. Larger fringes surrounding the peak represent the mountain contours at different altitudes. Similarly on the hologram, the small circular black fringe represents that portion of the vibrating plate which had the greatest local displacement from its static condition. The static condition (base-plane) is the plane formed by the clamped edge and in figure 9 is seen as a white border surrounding the fringe patterns.

The particular small group of fringes being discussed would be labeled the (1, 1) or "oil can" mode if they alone completely covered the vibrating surface. To visualize the relationship between this area and those adjacent to it, assume that at some arbitrary instant of time this small area were at its peak outward displacement. The two groups of fringes immediately adjacent to it must, at that same instant, be at the peak of their inward displacements. This results from several factors: (1) the actual displacement values are very small (one fringe is approximately equal to  $36(10^{-6})$  inches, (2) the maximum angle between an adjacent peak and valley is less than  $0.003^\circ$ , and (3) the slope transition between this peak and valley must be smooth. The first two conditions assure us that the plate is being stressed well within its elastic region and no permanent surface deformation is occurring. (Proof that the bending stresses are well within the elastic limit will be shown in section VI.) If the third condition did not hold, a sharp change in slope at the base-plane would produce severe fatigue at these points, thereby causing the plate to rupture in a short time--something which did not happen over the estimated  $50(10^6)$  cycles of operation during this experiment.

If one labels the phase of the lower left group as "+" then

the two groups next to it can be labeled as "-." Furthermore, those groups adjacent to the "-." groups must be "+." This technique can be continued until all groups are labeled, with the result that every "+" group will be surrounded by "-." groups, thus demonstrating the consistency of this interpretation. Moreover, at any arbitrary instant of time, all "+" groups will be going in while the "-." will be going out, or vice versa. These groups will change direction at the rate of the excitation frequency (roughly 9,000 times per second). The time-average of the displacement across this surface will produce a two-dimensional standing-wave pattern analogous to the electrical standing wave patterns observed in radar waveguides.

A hologram is recorded on a photographic plate when coherent light impinges on that plate from two synchronized sources, the light from one of these sources having been reflected from the object under investigation. The diffraction pattern caused by interference between these reference and object beams is recorded on the photographic plate. When viewed in normal (incoherent) light, the plate appears dark with a thin rainbow through it. When illuminated by a coherent light source, e.g., an expanded laser beam, the object can be seen in three dimensions. Changing the viewing angle allows one to see other parts of the object which are hidden from other viewing directions. If, during the exposure of the photographic plate, the object is moved, black interference fringes, occurring at approximately  $1/2$  wavelength intervals of displacement, will be superimposed over the image of the object. This latter type of procedure is referred to as interferometric holography. When the object is vibrated in simple harmonic manner, its surface spends most of the time at the maximum

and minimum points of displacement. The black interference fringes are produced by the destructive interference of the diffraction patterns produced on the plate during these times of maximum and minimum displacement.

Many difficulties arise in the taking of holograms. Of primary importance are: the exclusion of all ambient light during exposure of the photographic plate, operation in the proper exposure range for the particular emulsion, careful control of object vibration amplitude, and suppression of the relative motion between the optical components and the object's reference or base-plane. Control of ambient light in the laboratory is accomplished through the careful design of special light-tight, windowless rooms. Labyrinth entrances, door seals, and flat black paint on all surfaces provide for a dark, non-reflecting optical environment. At the water tower, all portholes were covered with opaque black plastic, as was the surface of the tank. Furthermore, holograms were made only at night.

There are many different types of photographic plate emulsions. The type utilized at NUSC/NL is of the highest scientific grade (Agfa-Gevaert No. 10E56). This emulsion has an operating curve of light transmission versus exposure which is nearly linear in its central region. It becomes necessary to carefully bias the emulsion into this linear region in order to obtain holograms with the best resolution. The bias is usually controlled by the amplitude of the reference beam with respect to that of the object beam, each measured separately at the photographic plate using a photocell detector.

Control of object vibration amplitude is necessary because of the non-linear Bessel function relationship between fringe numbers and

actual displacement values. Since the successive maximums of the zero-order Bessel function decrease in amplitude with increasing argument, the bright fringes between adjacent dark fringes also decrease in amplitude with increasing fringe number. With vibration amplitudes of more than 20 or 30 constructive and destructive fringes, it becomes impossible to separate these higher numbered bright and dark fringes. Since the adjacent bright and dark fringes are roughly  $1/4$  wavelength apart, a limitation in vibration amplitude occurs at about five wavelengths of the laser beam.

Suppression of the relative motion between all optical components and the vibrating object base-plane is an absolute necessity. In the laboratory, all the equipment including the vibrating object was placed on a block of polished granite 10 inches thick. The block itself was isolated from the concrete laboratory floor by the use of three air-spring mounts. All optical instruments were solidly housed in massive holders with three-point support. A similar technique was used at the water tower, except that the granite block was solidly connected to the concrete apron surrounding the tower.

The optical arrangement employed in the laboratory to make the initial holograms is shown in figure 10. The Coherent Radiation, model 52, argon gas laser has a wavelength of 0.5145 micron ( $\mu$ ). This green-blue light is very close to the  $0.49\mu$  wavelength that penetrates water with the least attenuation, i.e., the "blue-green window." An electronic shutter was attached to the end of the laser to provide careful control of exposure time. Figures 11 and 12 are double-exposure photographs of the optical instrumentation and the laser



beam<sup>4</sup>. The shutter can be seen at the end of the buff-colored laser near the top-left in figure 11. The green laser beam passed through this shutter, was reflected by a mirror at the corner of the granite slab, and entered the beam-splitter. (The path of the laser beam is most readily apparent in figure 10, where the direction of energy flow is indicated by dark arrows.) The splitter is designed to provide a 9 to 1 intensity ratio between the object and reference beams, respectively, and ascertains that the two coherent beams are synchronous. The reference beam passed through a variable attenuator (actually a round variably silvered mirror) to further control its intensity. To maximize coherency it is good practice to keep the reference beam and object beam path lengths roughly equal; thus, the reference beam was directed back down the table to be reflected forward again by another mirror, and directed toward the photographic plate in its heavy U-shaped holder. When the beam was about 2 feet from the plate, it entered a 10-power lens which expanded it from the original pencil beam and caused it to spread its energy uniformly around the 4-inch by 5-inch photographic plate.

The object beam, after passing through the splitter, was reflected by a mirror toward the object to be studied. Similar to the reference beam, the object beam was also expanded, this time by a 20-power lens, to irradiate the object. This object was the 6-inch by 9-inch radiating surface firmly attached to the heavy square steel ring. The yellow ring is readily visible in figure 11. The ring was

---

<sup>4</sup> Double exposure was necessary because light from the flash-bulb completely obliterated the low off-axis intensity of the laser beam. The beam was superimposed on the normal photograph by a time exposure.

placed in a long water-filled trough that had a large porthole on the end. In figure 11, the expanded object beam can be seen as it entered through this porthole and illuminated the radiating surface. Light was reflected from the radiating surface (the object beam) and it also engulfed the photographic plate. A portion of the radiating surface can be seen in figure 12 by looking through the photographic plate holder. At the plane of the photographic plate, the entire radiating surface was visible. The object beam intensity is considerably lower than the reference beam (about  $1/3$ ). For optimum photographic purposes, the reference beam is adjusted by means of the variable attenuator to provide this proper bias level for the emulsion.

The uniformity of the intensity over the plate from each separate beam was measured. Small adjustments could be made by moving the expanding lens. To reduce any laser light scattered from the optical apparatus from reaching the photographic plate, additional opaque barriers and shades were employed. A final intensity reading at the photographic plate, with both beams present, provided the information necessary to establish (with knowledge of the emulsion speed) the proper exposure time,  $1/2$  second in this instance.

The radiating surface was continuously excited by an oscillator-amplifier-transducer chain. The AN/SQS-23 transducer was located behind the ring; its top is barely visible in figure 11.

An unexposed photographic plate was removed from its light-proof box (with no light in the room) and placed in the U-shaped holder. The electronic shutter was triggered providing exactly  $1/2$  second of laser illumination of the object. The photographic plate was then returned to another light-proof box, ready to be developed.

The developing of a batch of plates took place shortly thereafter in an adjacent dark room. After drying, the plates were illuminated from the rear by the expanded reference beam alone. The hologram could then be seen and, if desired, could be photographed using conventional cameras and film.

In the search to find a classical resonant mode between 8-10 kHz, the first radiating surface studied was an aluminum plate 1/16 inch thick. The classical resonances of this plate were very low in frequency (about 1-3 kHz). The aluminum plate was removed from the ring and a stainless steel sheet, 1/8 inch thick, was glued to the ring. Both the increase in thickness and the increase in elastic modulus would tend to raise the resonant frequencies. For this plate, the (5, 5) mode seen in figure 9 was found at 9220 Hz by use of the laboratory setup shown in figure 10. This concluded the initial holographic studies.

## B. Acoustic-Holographic Experiment at the Water Tower

This portion of the investigation is most important since only at the water tower could the acoustic and holographic measurements be taken consecutively. Although better holograms can be obtained in the laboratory, and more detailed acoustic measurements can be made at conventional under-water acoustic calibration facilities, in neither of these locations can both types of measurements be performed simultaneously nor consecutively. The mounting of the radiating surface at the bottom of the tower and the operation of the rotator at the top of the tower have been covered in section II. Likewise, the acoustic measurement technique and its associated instrumentation have been discussed in detail. This subsection will deal primarily with the hydrodynamic calibration of the hydrophone cable, establishment of the measurement contours, and the actual performance of this experiment.

A plumb line, attached to the heavy vertical shaft on the rotator, was dropped from the surface to mark the center of rotation at the top of the tripod (which was resting on the bottom of the tower). The radiating surface and its attached box were placed on the tripod such that the center of rotation coincided with the center of the radiating plate. A wire-covered wooden frame work called the "retrieving platform" normally rested on the bottom of the tower (see figure 1). This platform could be raised at any time by means of heavy steel cables attached to four synchronous electric winches. The retrieving platform was utilized to raise and lower the tripod in order to make minor position adjustments of the sound box resting upon it. Before the platform was raised, the drawbridge was elevated to about a 45° angle. This allowed unencumbered access to

the center of the raised platform. Note should be made that holes were cut in the retrieving platform to allow the feet of the tripod to rest firmly on the bottom of the tower. The concrete base, underlying the tower and forming the apron outside, acted as a huge inertia block and served to tie the tripod to the granite optical table with little relative motion between the two.

First, the cable length was calibrated. The hydrophone was suspended directly in front at the middle of the radiating surface. At the point where the cable passed over the carriage on the rotating arm the cable was marked with white tape. Other tape marks were placed on the cable at 1-foot intervals both above and below this reference mark. These marks provided for rapid changes in  $\Delta h$  during the experimental runs.

Figure 13 indicates the "drag" and "kiting" angles referred to in this discussion of the hydrodynamic calibration procedure. When the weighted hydrophone cable was suspended from the arm, without the rotator energized, the cable acted as another plumb line. Then, when the rotator was energized, the hydrophone began to move but, with a certain spatial delay or "drag angle." The maximum drag angle is associated with maximum cable velocity. Since the angular velocity was constant (1 revolution in 4.25 minutes), maximum cable (tangential) speed occurred at the greatest radius (8 feet). The carriage was moved to the 8-foot position on the arm. The arm was carefully positioned so that the plumb line formed by the hydrophone coincided with the plumb line attached to the shaft when viewed through the narrow vertical slot formed by two pieces of masking tape on a port-hole at the base of the tower. The angle of the arm in this position

was inscribed on the top of the rotator. The rotator was then energized. After one revolution, another line was inscribed on the top of the rotator, denoting the arm position at the instant when the hydrophone was again aligned with the porthole slot and the shaft plumb line. The angular difference between the two inscribed lines was  $12^\circ$  and is an accurate measure of the drag angle. The test was repeated to ensure the results. Similar tests were run allowing less than 1 revolution for drag angle build-up. The results showed that the full  $12^\circ$  drag angle was established in as little as  $1/4$  revolution of the arm.

A surveyor's transit was used to determine the amount of "kiting" (i.e., swing-in or swing-out) that accompanied cable motion. Depending upon the many parameters involved (e.g., hydrophone and cable mass, cable length, and hydrodynamic damping), a weight on the end of a line can be made to swing out much farther than the radius about which it is being rotated at certain speeds. The same mass can also be made to circumscribe a much smaller circle than the radius at its driven end merely by changing the angular velocity (usually increasing it). At the extremely low speed employed at the water tower, and with the very light hydrophone mass compared to the weighted cable mass, it was impossible to predict (in any reasonable length of time) the degree of kiting. The in situ calibration of this parameter provided the answer; there was no kiting at all! The transit was set up at a porthole and adjusted so that its crosshairs bisected the hydrophone, with the carriage at 8 feet, the rotator stationary, and with a  $90^\circ$  angle between the arm and the transit orientation. The arm was slowly moved back and forth to guarantee that the transit was truly

aligned tangential to the hydrophone's static circle of rotation. The rotator was subsequently energized and, after allowing a few revolutions to establish steady-state conditions, the hydrophone was tracked with the transit. The angle corresponding to the hydrophone's most horizontal excursion was noted. This angle was identical with that recorded for the stationary condition, i.e., the kiting angle equals zero. Repetitions of this test yielded data which differed at most by  $0.1^\circ$ , the accuracy limitation of the transit.

These tests completed the calibration of the measurement sphere. The hydrophone's position in space can be completely determined by (1) the amount of cable above or below the reference mark ( $\Delta h$ ), (2) the distance of the carriage from the shaft ( $\Delta r$ ), and (3) the maximum drag angle of  $12^\circ$ . A linear interpolation of this drag angle as a function of  $\Delta r$  will produce contour alignment well within the angular accuracy necessary to demonstrate the feasibility of this dissertation's hypothesis.

The optical table was enclosed by a plywood structure at the bottom of the tower. Figure 14, a photograph taken inside this structure, shows the laser and the various splitters, mirrors, lenses, etc., necessary for making the holograms. The same holographic technique described earlier in this section was employed; the only significant difference was the long (roughly 30 feet) distances between some components. To keep the reference beam path length nearly equal to that of the object beam, the former was directed through one porthole to a "corner cube" mounted on the tripod. This cube has the property of reflecting the laser beam back in exactly the same direction as it came from: only 1 inch lower in space. Scrutiny of figure 15 will

reveal a second thin beam just below the predominant reference beam in the photograph. The funnel-shaped object beam, illuminating the radiating face of the sound box, can be seen entering the tank from the second porthole. The photographic plate holder was positioned near the larger (reference beam) porthole. The alignment of the radiating surface with this porthole is apparent in figure 15. As is the usual practice, several holograms were made at 10-20 Hz intervals about the desired frequency (9220 Hz), as well as several holograms at that frequency using different exposure times, excitation voltage levels, etc. When developed, most of these plates produced acceptable holograms. The hologram shown in figure 9, the classical (5, 5) mode, was one of these, but it occurred at 9240 Hz. The slight increase in frequency of the (5, 5) mode is attributed to a slight increase in elastic modulus of the stainless steel plate due to the cooler water in the tower compared to that in the laboratory trough, and to the change in hydrostatic pressure. More will be said of this later in section III C.

The desired hologram having been obtained, the electronic instrumentation was calibrated at this latest frequency. Polar patterns were run at 1-foot intervals over the measurement sphere. The  $\Delta h = -7$  foot and  $\Delta h = -8$  foot contours could not be obtained due to the presence of the retrieving platform. In all, 15 patterns were obtained plus calibration runs at the start and at the completion of the experiment. Analysis of these contours will be covered in section IV.

The most noteworthy event in this portion of the experiment was the last-minute failure of the backup (automatic data reduction) subsystem. With only a few hours remaining before mandatory experiment



termination, a failure occurred in the tape recorder on channel 4, the raw acoustic data shown in figure 7. Attempts at correcting the failure proved fruitless. Fortunately, the primary hard-copy polar recordings were being produced in fine fashion. Regardless of this failure, the remaining channels were recorded to demonstrate the time-stationarity of the experiment. The redundancy of the independent measurement techniques was greatly appreciated in these final hours. As a result of this failure, and of the fine operation of the primary (polar recorder) measurement technique, the automatic data reduction phase of this experiment was not utilized.

#### C. Comprehensive Investigation of the Various Plate Resonances

The shift in the (5, 5) mode resonant frequency from 9220 Hz in the laboratory to 9240 Hz at the water tower initiated an investigation of the complete spectrum of the radiating plate resonances. In order to simulate all of the conditions present at the water tower (with the exception of hydrostatic pressure), the laboratory holography arrangement was modified as shown in figure 16. A large 80-gallon aquarium was substituted for the long trough. The radiating surface and its ring were bolted to the box to provide the same acoustic excitation as was employed at the water tower. Ice was used to lower the water temperature within the aquarium.

Two different methods were used to scan the frequency spectrum in the search for resonant modes: real-time observation, and the use of a fiber-optic displacement measurement instrument. Johnson and LeBlanc (3) discuss the theory behind the real-time holographic observation of vibratory motion. Basically this technique relies on the

creation of constructive and destructive fringe patterns over the surface of the object, formed by the interference of the object beam when viewed through a previously developed hologram of the stationary object. First, a conventional hologram is taken of the object in its stationary condition (i.e., no excitation or other motion). After development, the hologram can be viewed in coherent light, yielding a three-dimensional image of the object. This stationary hologram is then carefully returned to the photographic plate holder in exactly the same position as when the plate was exposed. The radiating plate is then excited, and the reference beam is blocked from the plate. The object beam, coming from the vibrating surface, forms interferometric fringe patterns by interaction with the diffraction pattern recorded on the stationary hologram. When this stationary hologram is viewed in the (vibrating) object beam, a condition similar to figure 17 will be observed. The whole reference-plane is covered by vertical fringes. This is partially caused by minute changes in the position of the stationary hologram, and mostly by contraction of the emulsion during the development process. Superimposed on these vertical stripes are nine distinct regions of fringe smearing; 3 rows of 3 columns, i.e., the (3, 3) mode. Figure 18, a hologram of the (3, 3) mode, was taken at the same frequency (3195 Hz). As the plate excitation frequency was changed, the regions of fringe smearing also changed. Thus by making a slow frequency sweep, each plate resonance could be observed and its frequency recorded. This technique is limited by the experimenter's experience since some low-amplitude modes are difficult to discern, especially those at the higher frequencies.

The fiber-optic technique gives a much stronger indication of resonance throughout the frequency range of interest. However, it is sensitive to the probe position and also considerably more time is required to determine resonant frequencies with this method. Figure 19 indicates the arrangement of electronic and optical instrumentation necessary for this technique. The essence of this method lies in the amplitude modulation of a reflected light beam--the light beam being conducted through a fiber-optic probe. This light crosses a small gap and impinges on a small square of flexible mirror tape glued to the vibrating surface. The light reflected from this mirror is received by the same probe and conducted to the Fotonic Sensor fiber-optic receiver. As the vibrating surface moves, the gap distance changes slightly and causes amplitude modulation of the light reflected from the small mirror. This small degree of modulation is detected and amplified in the Fotonic Sensor.

The output of this device is a low amplitude ac signal with components at the frequency of the surface vibration. Being of low amplitude, this signal is prone to contamination by noise from both electromagnetic and optical sources. Optical noise results from, among other things, the 60 Hz modulation of the ambient light in the laboratory due to the fluorescent lamps. This optical noise enters the system at its most vulnerable point, the tip of the fiber-optic probe. To clean-up this signal, a Burr-Brown ac amplifier raised the level of both signal and noise. A Krohnkite band-pass filter then eliminated all frequencies below 2000 Hz and above 8000 Hz. The filter output was displayed on an oscilloscope. As the plate excitation frequency was slowly varied, the sine wave seen on the

oscilloscope would change both in wavelength and in amplitude. As the frequency approached a fundamental plate resonance, the amplitude of the signal would usually increase significantly then decrease as the excitation passed through this resonance. This would happen provided that the probe and mirror were not located in a node of the particular resonant mode. Thus, not all resonances could necessarily be observed with the probe at one location, necessitating several runs in different locations. A further complication arises at off-resonant frequencies. Since the vibration at these frequencies is composed of the interaction of two or more fundamental modes, certain areas on the vibrating surface will pass through a sharp increase in amplitude as excitation frequency is varied, due solely to changes in these interactions. If the probe was located in one of these areas, the oscilloscope trace would produce a false indication of a resonant condition. A large number of these false resonances would be recorded during each run. By a judicious selection of probe locations, the fundamental resonances can often be deduced from the large number of possibilities. For example, if one is searching for a mode which has an even integer, e.g., (2, 3) or (4, 2), there should have been no resonant condition recorded when the probe was located directly in the center of the plate, and yet, at this same frequency, high amplitudes should have been recorded for probe locations slightly removed (an inch or so) from the center. Thus, by using knowledge of the node positions of expected resonances, many of the false resonances could be eliminated.

By utilizing both the real-time and the fiber-optical techniques, the complete frequency spectrum of fundamental plate resonances was explored up to 6600 Hz. Above this frequency, the modal density

is so large that hundreds of holograms must be taken at close intervals to find just a few more classical resonances.

The primary resonances, i.e., the low order modes, were photographed. A few examples of these modes can be seen in figures 20 and 21. Figure 20, the (2, 3) mode, occurred at 2633 Hz, and figure 21, the (4, 2) mode, was found at 2677 Hz. Figure 18, the (3, 3) mode shown previously, was found at 3195 Hz. These fine examples are the result of a large number of exposures with slight changes in excitation frequency and amplitude at each resonance. Table 2 contains the modal frequency information. In order to consolidate all of the mode number and frequency information, figure 22 was drawn. In this graph, the mode numbers are plotted as a function of the frequency of the resonant mode (the abscissa) and the first modal identification number (the ordinate). This number corresponds to the number of peaks and valleys one would see if he viewed a horizontal section through the plate vibrating in that mode. The curves on the graph represent those modes with common second numbers. The second modal identification number is associated with the vertical peaks and valleys at that resonance. This family of curves can be extrapolated to indicate the approximate frequencies at which other modes might be found. For example, if one extrapolates the  $m = 3$  curve, he would find that the (6, 3) mode should occur at about 6000 Hz. Some modes exist over a broad frequency range; an example is the (6, 1) where the same mode produced good holograms at both 3880 Hz and at 4175 Hz. This broad resonance explains why the (5, 2) mode was not found. The (5, 2) should have occurred at about 3750 Hz, but the stronger amplitude (6, 1) mode dominated that frequency region as well. Similarly, the (1, 4) mode could not be found at its

TABLE 2

**MODAL FREQUENCIES FOR A CLAMPED-EDGE  
PLATE VIBRATING IN WATER AT 68°F**

**Plate Parameters:**

**Material:** 18-8 stainless steel  
**Dimensions:** 6 inches wide by 9 inches long by  
 0.125 inch thick

**Excitation Method:** water-coupled acoustic tones

**Modal Designation:** (n,m); (n) denotes the number of  
 antinodes along the 9-inch length;  
 (m) denotes the number of antinodes  
 along the 6-inch width

Mode Identification	Frequency in Hz
(1, 1)	500
(1, 2)	1100
(1, 3)	2300
(1, 5)	6000
(2, 1)	660
(2, 2)	1350
(2, 3)	2633
(2, 4)	4332
(3, 1)	1155
(3, 2)	1945
(3, 3)	3195
(3, 4)	4997
(4, 1)	2038
(4, 2)	2677
(4, 3)	3961
(4, 4)	6190
(5, 1)	2900
(5, 3)	5028
(6, 1)	3880-4175
(6, 2)	4890
(7, 1)	5555

**Estimate of Accuracy:** Approximately  $\pm 10$  Hz

expected 4000 Hz because of the strength of the (3, 3) and (6, 1) modes. This region (4000 Hz) is one of the bands of high modal density. In general, as frequency increases, so does modal density, thereby making it more difficult to identify the classical resonant modes.

Figure 22 and table 2 actually apply for only a single water temperature, 68°F. When ice was added to the aquarium to drop the temperature, the frequencies of the classical modes increased an average of 30 Hz. A decrease in temperature causes an increase in the plate's modulus of elasticity; i.e., the plate becomes stiffer. Drucker (10) shows graphs of the modulus for several metals as a function of temperature. All the common materials have the same general shape, with steel increasing by  $12(10^3)$  psi per Fahrenheit degree from its nominal  $30(10^6)$  psi value. This slight increase in modulus, interacting with even smaller changes in density and Poisson's ratio, produces a slight increase in frequency for a given modal resonance. Table 3 shows the actual increase for five different modes. Considering the accuracy limitation of about  $\pm 10$  Hz (for this experiment) in determining the exact center frequency of the resonant modes, these shifts can be considered to be quite uniform. It can be stated that an increase in water temperature of 26 Fahrenheit degrees causes an increase in modal resonant frequencies of about 30 Hz. Thus temperature changes can account for the 20 Hz increase observed at the water tower. Apparently, the slight (1/50 of 1 percent) increase in water density due to 100 feet of hydrostatic head affects the shift in modal resonances by less than the accuracy limitation of  $\pm 10$  Hz.

TABLE 3  
SHIFT IN RESONANT FREQUENCIES DUE TO  
CHANGES IN WATER TEMPERATURE

Mode Identification	Resonant Frequency (Hz)		Deviation (Hz) Warm to Cold
	68°F	42°F	
(4, 2)	2677	2715	+38
(3, 3)	3195	3220	+25
(4, 3)	3961	2997	+36
(9, 1)	9021	9050	+29
(5, 5)	9219	9240	+21

D. Broad Spectrum Acoustic Measurement of the Radiating Surface

To complement the broad spectrum holographic investigation, a similar acoustic investigation was undertaken at the NUSC/NL Dodge Pond Field Station. Dodge Pond is equipped with the most up-to-date machinery and instrumentation for the accurate determination of underwater acoustic intensities and radiation patterns. This phase of the study had the following specific goals:

1. verification of the acoustic patterns measured at the water tower,
2. calibration of the LC-10 hydrophones used at the water tower,
3. additional acoustic measurements to cover the entire frequency band from 200-12,000 Hz.

Three large enclosed barges are permanently anchored in the deepest portion (48 feet) at the 33-acre fresh-water pond. In normal usage, the underwater projector is attached to the end of a 6-inch-diameter stainless steel shaft and lowered into the water until the projector is about 20 feet below the surface. A Naval standard hydrophone is lowered on aluminum pipe to the same depth and horizontally displaced up to 30 feet from the projector. After calibration



of the instrumentation in either the continuous wave (CW) or the pulse mode, the projector is slowly rotated about its vertical axis. The resulting acoustic intensity seen by the hydrophone as a function of rotation angle is recorded on standard polar charts. In order to verify the water tower contours, it was necessary to vary the horizontal distance ( $\Delta h$ ) between the projector (the sound box with its radiating surface) and the receiving hydrophone (type H-23). Simultaneously, the depth of the receiving hydrophone ( $\Delta r$ ) was changed as a function of  $\Delta h$  in accordance with the table shown in Appendix A. Since more accurate control of the hydrophone position relative to the projector was available at Dodge Pond than was possible by dangling a moving hydrophone through 100 feet of water at the water tower, more contours (every 1/2 foot) were taken at Dodge Pond. Also, the lowest contours could be measured at Dodge Pond but not at the water tower because of the tripod and retrieving platform.

A problem arose as to how one could easily compare the 33 contours measured at Dodge Pond with the 15 contours obtained at the water tower for the same excitation level and frequency. The solution employed was to stack all the contours of a set vertically in the proper order of  $\Delta h$  (i.e.,  $\Delta h = -8$  feet on the bottom,  $\Delta h = +8$  feet on the top), and with all corresponding radials vertically aligned. The individual polar plots were first glued to thin wooden sheets and then cut along the recorded intensity line except for the backward-pointing 120° segment. These wooden contours were stacked with all contour center points also in a vertical line. Figure 23 compares the montage of the Dodge Pond contours with that assembled from the water tower contours.

With this type of model, the simplest acoustic point source, radiating equally in all directions, would appear as a squat vertical cylinder. This interpretation can be explained as follows. Since the sound intensity measured over any sphere about the simple source would be constant everywhere, all contours would be identical and a stack of these would form a cylinder. At first glance, it is evident that the two models are quite similar in their broad forward-pointing major lobes. This type of radiation is characteristic of monopole sources. It is only in the fine detail associated with secondary lobe structure that the Dodge Pond model (with more than twice as many contours) differs significantly with that made from the contours measured at the water tower. If one looks closely at the low points of these secondary lobes on the Dodge Pond model and observes their relative locations, one can, with some reservations, find these same low points on the upper half of the water tower model. The lower half of this latter model suffers from loss of contours and from the contamination of the acoustic signal by interactions with the tripod and the bottom of the water tower.

At the base of each model is a calibration graph denoting acoustic intensity in decibels as a function of radial distance from the center of the contour. All contours in a single model have identical calibrations. To facilitate visual comparison, that band of intensity from 60 dB to 70 dB/l<sub>μ</sub>bar was colored blue, and that from 70 dB to 80 dB was colored red on each calibration sheet. The horizontal and vertical beamwidth of each model can be determined from the individual contours and knowledge of the test geometry given in Appendix A. Kinsler and Frey (17), page 173, indicate that there is

presently no established standard for measuring beamwidths. Intensity ratios of 0.5 (down 3 dB), 0.25 (down 6 dB), and 0.1 (down 10 dB) are mentioned. This dissertation will use the middle value. The horizontal beamwidth for the Dodge Pond model (down 6 dB) is  $92^\circ$ , whereas that of the water tower model is  $120^\circ$ . The vertical beamwidths are identical,  $93^\circ$  for both models. The on-axis intensity level of both models is also identical (+77 dB// $\mu\text{bar}$ ). Considering the physical and temporal constraints placed on the experimenter at the water tower, it is felt that water tower contours are a close representation of the actual three-dimensional pressure pattern produced by the plate vibrating at 9240 Hz with its attached sound box.

The LC-10 hydrophones used in the water tower experiment were calibrated with the same 140 feet of cable that was used in that experiment. The data hydrophone had a sensitivity of -114dB//1Vrms/ $\mu\text{bar}$  (i.e., 114 dB below 1 Vrms would be present at the end of the cable for an acoustic pressure intensity of  $\mu\text{bar}$  at 9240 Hz). The manufacturer's calibration for this hydrophone with about 30 feet of cable was -108dB//1Vrms/ $\mu\text{bar}$ . The 6 dB loss in sensitivity due to the additional capacitance contained in 110 feet of cable is quite reasonable. The manufacturer claims that hydrophone sensitivity is flat from 1000 Hz to 40,000 Hz. Radiation patterns made at Dodge Pond show the hydrophone to be omnidirectional  $\pm 0.5$  dB at 9240 Hz in the horizontal plane. The vertical plane pattern was influenced by the nearness of the 6-inch shaft, but even so, the pattern showed omnidirectionality  $\pm 2$  dB. The reference LC-10 hydrophone was also calibrated, yielding similar results. These tiny (a little longer than an inch) hydrophones provided excellent service throughout the experiment.

To complement the broad spectrum holographic investigation described in section III C, a correspondingly broad spectrum acoustic investigation of the radiating surface was conducted. This study was performed in two overlapping parts due to the inability of the SQS-23 transducer to generate sufficient acoustic pressures below 3000 Hz. A Navy standard J-9 transducer was used to cover the region from 200-5000 Hz. The H-23 hydrophone was positioned 8 feet in front of the radiating surface at a depth of 20 feet. The excitation frequency was automatically swept through the appropriate frequency band. The received acoustic signal strength was displayed as a function of frequency on a strip-chart recorder. Figure 24 is a typical graph taken under these conditions. A great dip in acoustic intensity is evident at 1730 Hz with several smaller dips occurring at 850 Hz, 1260 Hz, and 2300 Hz. Horizontal patterns at each of these dips revealed monopole radiation, although the great dip was very surprising. The horizontal pattern at this frequency showed that the sound box was radiating 15 dB more from its back end than from its open front! Analytical investigations (in section V) show this to be a result of cancellation of the forward propagating wave, by reflections from the material at the back of the box. Another surprising find was that the normal-mode acoustic frequencies of the interior of the box did not coincide with any of the predominant features in figure 24. These puzzling observations led to further investigations using the same sound box and transducer, but with the radiating surface and its heavy clamping ring removed. Figure 24 is, in fact, the graph associated with this condition. The only change in acoustic intensities between these plate-on vs plate-off conditions was a sharpening of the dips

and a slight lowering of their frequencies due to the extra two inches of length added by the heavy steel ring, when it was attached to the box. The box-transducer combination completely dominated the far-field acoustic pressure!

Similar results were obtained with the SQS-23 transducer in the box. Figure 25 was obtained with this combination and with the radiating surface attached. Several sharp dips and peaks are seen following the gradual rise in frequency from 3000-4700 Hz. This same rise is observed for the identical frequency band in figure 24, thus tying the two graphs together. When the radiating surface was removed, the graph intensity became much smoother (the same condition seen before) but the characteristic shape and level remained. Patterns taken at the major dips and peaks showed general monopole radiation similar to that observed at the lower frequencies, although the front-to-back ratio increases (as expected) with increasing frequency.

Since the transducer-box combination was dominating the entire frequency spectrum it only remained to demonstrate that all measurements have been taken in the far-field condition. Figures 26 and 27 show the results of these tests taken at 1731 Hz (the big dip frequency) and 9240 Hz (the water tower frequency). Theoretically, sound pressure level should fall off at the rate of 6 dB per doubling of distance if far-field spherical spreading is occurring. A line of this slope was drawn on each graph, aligning the more distant points. It can be seen that at the nominal 8-foot measuring distance, far-field conditions existed at both 1731 Hz and at 9240 Hz. We can assume it holds for all frequencies between these limits, as the far-field condition is limited by low frequencies in normal measurement environments. It is interesting

to note that the far-field condition existed as close as 2 feet from the radiating surface at 9240 Hz.

#### IV. ANALYTICAL PREDICTION OF THE ACOUSTIC PATTERN USING A HOLOGRAPHIC INPUT

##### A. Introductory Remarks

This section will detail the technique used to predict the acoustic far-field radiation pattern of a complex vibrating surface by utilizing displacement information available through interferometric holography. The first item requiring attention is the conversion of the holographic fringe data into actual displacement values. Having done so, the classical technique employed by Morse (11) to predict the acoustic pressure at an arbitrary point due to a finite-sized radiator is modified to use this displacement data. An algorithm is developed and programmed on the UNIVAC 1108 computer to yield results directly comparable to the acoustic measurements made at Dodge Pond and at the water tower. Finally, these analytical predictions are compared with the actual measured patterns.

##### B. Converting the Holographic Data into Displacement

Figure 9, the hologram of the (5, 5) mode obtained at the water tower, will serve as the input data for the analysis in this section. As was explained in section II, this hologram shows the peak local displacement over the plate. Where the plate was cemented to the stiff backing ring, the hologram is solid white with no fringes and, therefore as expected, no motion occurred in these areas. Similar "node" or no motion areas can be found on the vibrating surface itself, usually at the intersection of four adjacent "antinodes" which

correspond to mountains on a topographic map. As was also explained previously, for any particular instant of time, the motions of each antinode in any contiguous pair must be in opposite directions; i.e., one must be "going out" while the other is "going in." The task at hand is to reduce this two-dimensional photograph into a series of numbers that will describe this peak displacement everywhere on the radiating surface.

The first consideration is that of accuracy. It is obvious that the local displacement cannot be measured any closer than the degree to which the fringes can be resolved. The maximum number of dark fringes that can be discerned in this hologram for any single antinode is 7. Two adjacent antinodes could range in numbers from +7 to -7 dark fringes. These dark fringes correspond to destructive interference; the bright fringes between them correspond to constructive interference. For any particular spot on the hologram, the only definite conclusion which can be reached is that this spot had an amplitude of so many black and white fringes above or below the node or base-plane. If we count the dark fringes as whole numbers and the bright fringes between them as halves, then our accuracy limitation is  $1/2$  the displacement between two adjacent dark fringes. With this limitation in mind, the hologram was divided into a grid work of small squares, the width of each square corresponding to  $1/2$  the distance between the two closest dark fringes on the hologram. The end result was a division of the 6-inch by 9-inch radiating surface into 47 rows and 67 columns for a total of 3149 individual blocks.

Before an actual value could be given for the local displacement of each of these blocks, an arbitrary decision was required



regarding the relative phase, i.e., the "in-going" or "out-going" direction, of each antinode. By assuming that the top left antinode was "going out" at our particular measurement instant, and calling this phase "+," all other antinodes were assigned + or - designations. The second antinode from the left on the top row at this same time must have been "going in," i.e., its phase is "-", because it was contiguous to the arbitrary reference antinode. Similarly, the left-most antinode in the second row must have a "-" phase because of its position adjacent to the reference antinode. In like fashion, all antinodes were labeled alternately + and -.

To aid in digitizing the holographic data, a thin sheet of plexiglass was used as a screen. The glass was scored to form the desired gridlines and then taped to a 16-inch by 20-inch photographic enlargement of the central portion of figure 9. The taped edges of the screen were marked to indicate the row and column numbers of the hologram.

The slow process of "reading" the hologram began. A value of + or - some integer number of dark fringes was assigned to each block on the screen which was over a predominately black area of the hologram. If the hologram under the block on the screen was predominately white, a value of  $1/2$  more than the lowest order dark fringe adjacent to that block was assigned. Nodal positions were recorded as "0." An example of the data listed for the start of row 5 will serve to illustrate this technique. Row 5 passes through the maximum points of the top row of five antinodes. The data starting from the left are as follows:

column	1	2	3	4	5	6	7	8	9	10	11
data	0	1	1.5	2	2.5	3	3.5	4	4	4	3.5

As can be seen, the local displacement had 0 value at the edge and steadily rose to a broad peak spanning columns 8 through 10. The remaining 56 columns of data in this row show the decline to a node and then the beginning of a negative phase of increasing magnitude with a negative peak between columns 21 and 22. Within the 67 columns of data, the values went from + to - to + to - to +, thereby indicating the relative phase and amplitude of the local displacement across the plate at row 5. To minimize the possibility of error in the designation of the fringe number for any particular square, the data were first tape-recorded to allow the writer to keep his hands and eyes continuously affixed onto the hologram. The tape recorded data, with frequent column identification checks, were then listed on a standard 80-column FORTRAN coding sheet during replay of the recording. The slowly changing rise and fall of the data was closely watched to further assure that no errors in phase notation occurred. These coding sheets, containing 25 rows of 80 columns, are filled out by the computer user with either FORTRAN programming information or data. The professional key-punch operators type a standard 80-column punched card for each row on the coding sheet. Allowing a clear space between adjacent data on a single row on the coding sheet and the subsequent computer card, a maximum of 17 columns of data were recorded per card. Four consecutive cards of 17, 17, 17, and 16 data items respectively, constituted one row of holographic data (67 columns). The complete data for row 5 are presented in Appendix B. A 3-digit identification

number was punched into the last columns of each card to aid in deck sorting should the cards become misarranged for any reason.

Powell and Stetson (12) provided the mathematical equation used for converting fringe numbers into actual displacement values. For the case of sinusoidal vibration,

$$I(X_1, n Y_1) = J_0^2 \left[ \frac{2\pi}{\lambda} (\cos \theta_1 + \cos \theta_2) \cdot m(X_0, Y_0) \right] I_{st}(X_1, Y_1), \quad (11)$$

where

$I(X_1, n Y_1)$  = image intensity of the n'th fringe of the hologram

$I_{st}(X_1, Y_1)$  = image intensity of the stationary object

$J_0[\alpha]$  = zero order Bessel function

$\lambda$  = wavelength of laser light in the media

$\theta_1$  and  $\theta_2$  = angles associated with the experimental setup

$m(X_0, Y_0)$  = the dynamic displacement at the point of interest.

Horvath and Wallach (13) indicate the important portion of this formula is the argument of the Bessel function:

$$\left[ \frac{2\pi}{\lambda} (\cos \theta_1 + \cos \theta_2) m(X_0, Y_0) \right]. \quad (12)$$

When this argument is one of the roots of the zero order Bessel function squared, a dark fringe will be produced, i.e., equation (11) equals zero. Figure 28 shows the roots of  $J_0^2[\alpha]$  to be identical to those of  $J_0[\alpha]$ ; thus a definite displacement  $m(X_0, Y_0)$  is associated

with each root of the Bessel function. By tabulating these roots and knowing the values of  $\lambda$ ,  $\theta_1$ , and  $\theta_2$ , the displacement associated with each fringe number can be determined. The first dark fringe corresponds to the first root; the second dark fringe to the second root; etc. The bright fringes between the dark fringes are associated with the magnitudes and arguments of the maximum values between successive roots of  $J_0^2 [\alpha]$ . These peaks are always exactly between two adjacent roots. Since the displacement associated with a bright fringe lies midway between the displacements of the two adjacent dark fringes, they need not be considered at this time.

Shortley and Williams (14) define the relative index of refraction of water to air ( $I_{WA}$ ) as

$$I_{WA} = \frac{c_A}{c_W}, \quad (13)$$

where

$c_A$  = speed of light in air

$c_W$  = speed of light in water.

On page 380, they list the classical relationship between wavespeed and wavelength as

$$c = f \lambda, \quad (14)$$

where

$f$  = wavefrequency

$\lambda$  = wavelength.

Substituting equation (14) into equation (13), we obtain

$$I_{WA} = \frac{f \lambda_A}{f \lambda_W} = \frac{\lambda_A}{\lambda_W} . \quad (15)$$

The wavelength in water ( $\lambda_W$ ) is equal to the wavelength in air divided by the relative index at refraction:

$$\lambda_W = \frac{\lambda_A}{I_{WA}} . \quad (16)$$

The value of  $I_{WA}$  for fresh water at 20°C (the conditions at the water tower) can be found in the "Handbook of Chemistry and Physics" (15) as 1.33299. Since the laser wavelength in air is known to be  $0.5145(10^{-3})$  cm, the wavelength in water is

$$\lambda_W = \frac{0.5145(10^{-3})}{1.33299} = 0.3860(10^{-3}) \text{ cm.} \quad (17)$$

The angles  $\theta_1$  and  $\theta_2$  in equation (12) correspond to angles of deviation from the perpendicular to the photographic plate for the object beam and the reference beam, respectively. Both of these angles were equal to 0 at the water tower. Using the above parameters in equation (12) and setting this expression equal to 2.405, the first root of the zero order Bessel function (as listed by Watson (16)), we obtain the displacement  $m(X_0, Y_0)$  for the first dark fringe:

$$\frac{2\pi}{\lambda_W} (\cos \theta_1 + \cos \theta_2) m(X_0, Y_0) = 2.405 \quad (18)$$

$$\frac{2\pi}{0.386(10^{-3})} (1 + 1) m(X_0, Y_0) = 2.405 \quad (19)$$

$$m(X_0, Y_0) = 7.39(10^{-5}) \text{ cm} \quad (20)$$

$$m(X_0, Y_0) \approx 29.1(10^{-6}) \text{ inches.} \quad (21)$$

The same technique can be used to obtain the displacement values of all the other dark fringes of interest. Table 4 shows these displacements and the root of the Bessel function associated with them. The displacement value of the first dark fringe is 29.1 microinches ( $73.9(10^{-6})\text{cm}$ ). The displacement of each successive dark fringe is 37.9 microinches ( $96.2(10^{-6})\text{cm}$ ) added to the value associated with the preceding fringe. The average displacement for the first five dark fringes is 36.1 microinches ( $91.7(10^{-6})\text{cm}$ ) per fringe. Figure 29 is a graph of displacement versus dark fringe number. The high linear correlation stems from the nearly periodic behavior of the roots of the zero order Bessel function, if the zeroth root is ignored. A non-linear equation that related displacement in cm directly to dark fringe numbers was fitted to the data on this graph, and to an identical graph for negative fringe numbers:

$$\xi = [.09615(N) \mp .02265](10^{-3}) \text{ cm,} \quad (22)$$

where  $\xi$  = local displacement in cm

$N$  = a positive or negative dark fringe number, i.e.,

$N = \pm 1, 2, 3 \dots$

$N \neq 0$

The minus sign is to be used with positive fringe numbers and the positive sign with negative fringe numbers.

Equation (22) was developed in a manner which minimizes the error within the fringe band of interest. The displacement error was kept at or below  $5(10^{-7})$  cm for dark fringe values up to the fifth fringe. This is two orders of magnitude less than the displacement at

the first fringe and about three orders of magnitude less than that of the fifth fringe! At the seventh fringe, this accuracy is only 1/2 as good as for the first five fringes. Since the first five fringes account for an estimated 99% of all the data taken from the (5, 5) hologram, the accuracy of the linear relationship is certainly ample.

This non-linear equation also holds true for the bright fringe values if they are indicated as being a certain number of dark fringes above the base-plane plus (0.5). For example, the third bright fringe would be denoted by ( $N = 3.5$ ). For all fringes of negative phase, a minus sign will proceed the fringe number (e.g.,  $N = -3.5$ ). The displacement value of the negative fringe numbers can be computed using the non-linear relationship with a change in the sign of the constant offset value (0.02265).

TABLE 4

RELATIONSHIP BETWEEN DARK FRINGE NUMBER, ROOT OF THE BESSEL FUNCTION, AND DISPLACEMENT

Dark Fringe Number	$J_0$ Root	Displacement ( $10^{-3}$ cm)
1	2.405	0.0739
2	5.520	0.1695
3	8.654	0.2658
4	11.792	0.3622
5	14.931	0.4586
6	18.071	0.5551
7	21.212	0.6516
8	24.352	0.7480
9	27.493	0.8445
10	30.635	0.9410
11	33.776	1.0375
12	36.917	1.1340

### C. Predicting the Acoustic Pressure at an Arbitrary Point in the Far Field

The method used to predict the acoustic pressure due to the vibrating surface follows the classical technique employed by Morse (11) in the prediction of the radiation from a round piston in a plane wall. Figure 30 illustrates the geometry utilized in his approach. Morse assumed the flat piston surface to be vibrating sinusoidally in time along the axis of the piston. He considered each element of surface area on the piston to be a simple source of sound. The acoustic pressure at any point in the far field was the sum of the pressures from each separate element. The summation was accomplished through a two-step integration over the disk-shaped radiating surface. The resulting integral has the form of the first order Bessel function,  $J_1(X)$ , giving the total pressure at the arbitrary point as

$$p \approx -\pi i f \rho \mu_0 a^2 \frac{e^{ik(r-ct)}}{r} \left[ \frac{2J_1(ka \sin \theta)}{(ka \sin \theta)} \right] \quad (23)$$

where

$p$  = total acoustic pressure at point P

$i = \sqrt{-1}$

$f$  = frequency of piston vibration

$\rho$  = density of the medium in the far field

$\mu_0$  = maximum piston velocity

$a$  = piston radius

$k$  = wavenumber =  $2\pi/\lambda$

$\lambda$  = acoustic wavelength =  $c/f$

$c$  = speed of sound in the medium



$r$  = distance from piston center to point P

$t$  = time

$J_1(X)$  = first-order Bessel function

$\vartheta$  = angle of P from the piston axis (see figure 30).

The expression in brackets,  $\left[ \frac{2J_1(X)}{X} \right]$ , is called the "directivity function" of the piston by Kinsler and Frey (17). At points along the axis of the piston the angle ( $\vartheta$ ) is zero, ( $ka \sin \vartheta$ ) is zero, and the directivity function is unity. Kinsler and Frey plotted this directivity function against the argument ( $X$ ). The shape of the resulting curve is similar to that of the zero-order Bessel function,  $J_0[\alpha]$ , in figure 28: i.e., unity at zero, nearly unity until  $X$  is about  $\pi/2$ , and eventually going through zero at  $1.2\pi$ . For fractional values of ( $X$ ), they propose the following relationship:

$$\left[ \frac{2J_1(X)}{X} \right] \approx 1 - \frac{X^2}{8} . \quad (24)$$

Although Morse assumed each element of area to be a simple source, we shall consider each block on our hologram to be a flat-topped piston, to guarantee the accuracy of our computations. Equation (23) is the base from which the acoustic pressure in the far field due to a single holograph block radiator will be computed. Since these radiators are square-shaped rather than round, a modification must be made to equation (23). Because we have assumed the surface of the block is moving uniformly at a constant sinusoidal velocity, we can also assume the only effect on the far-field near-axis pressure will be a slight increase in intensity due to increased radiating surface area. If

(a) is the radius of a disk enclosed in a square block,  $(\pi a^2)$  is the area of that disk while  $(4 a^2)$  is the area of the enclosing block. Thus, an increase of  $(4/\pi)$  can be expected for the additional radiating area.

On page 328, Morse (11) explains the effect of the large baffle is to double the acoustic pressure in the far field from that which would be present if no baffle existed. To have this doubling effect, the baffle must be several wavelengths long in each direction. Since the front of the radiating box had dimensions of  $2.06\lambda$  by  $1.58\lambda$  (i.e., 13 inches by 10 inches, respectively) the baffle condition can hardly be assumed to exist. Thus, equation (23) will be further modified by a factor of  $(1/2)$  to account for the absence of baffling.

The increased area correction factor was based upon near-axis pressures. It will now be shown that, because of the small size of the individual radiating blocks, the entire directivity function can be ignored; i.e., the blocks radiate equally in all directions.

The argument of the Bessel function in equation (23) is  $(ka \sin \theta)$ . This argument has a minimum value of zero when  $(\theta)$  equals  $90^\circ$ .

$$k = \frac{2\pi}{\lambda} = \frac{2\pi}{c/f} = \frac{2\pi f}{c} \quad (25)$$

$$k = \frac{2(3.1416)(9240) \text{ 1/sec}}{(1481 \text{ m/sec})} = 39.2 \frac{1}{\text{m}} \quad (26)^5$$

---

<sup>5</sup>The value 1481 m/sec is taken from Kinsler and Frey (17), p. 503, fresh water,  $20^\circ\text{C}$ .

$$k = \left(39.2 \frac{1}{m}\right) \left(0.3048 \frac{m}{ft}\right) = 11.95 \frac{1}{ft}. \quad (27)^6$$

The radius of the enclosed circular piston (a) within one holographic block was determined by measurements on the photographic enlargement of the central portion of figure 9. There were 81 blocks between the centers of the two bolt heads on the ends of the three-bolt row holding the top of the ring to the box. Since this distance was known to be exactly 11 inches and since the width of each block is (2a), then

$$81 (2a) = 11 \text{ in} \quad (28)$$

$$a = 0.0679 \text{ in} \left(\frac{1}{12} \frac{ft}{in}\right) = 0.00566 \text{ ft}. \quad (29)$$

Therefore,

$$ka = \left(11.95 \frac{1}{ft}\right) (0.00566 \text{ ft}) = 0.068. \quad (30)$$

The argument of the Bessel function in equation (23) goes from a minimum of zero to a maximum of (0.068). By use of the truncated series approximation (valid for small values of the argument) shown in equation (24), the directivity function for (ka) is

$$1 - \frac{(ka)^2}{8} = 1 - \frac{(0.068)^2}{8} = 0.9994. \quad (31)$$

The directivity function varies between unity and 0.9994 for all angles of ( $\theta$ ); thus, each block radiates omnidirectionally.

---

<sup>6</sup>The value 0.3048 m/ft is taken from Beranek (3), p. 465.

Combining this last conclusion with the modifications for increased area and lack of baffling, equation (23) reduces to

$$p \cong \left(\frac{4}{\pi}\right)\left(\frac{1}{2}\right) (-\pi i f \rho \mu_0 a^2) \left(\frac{1}{r}\right) e^{ik(r-ct)} \quad (32)$$

$$p \cong -i(2f\rho a^2)\mu_0 \left(\frac{1}{r}\right) e^{ik(r-ct)}. \quad (33)$$

We now modify the equation to enable the use of the holographic displacement data. For the case of steady-state sinusoidal vibration,

$$\xi_0 = \left(\frac{\mu_0}{i\omega}\right), \quad (34)^7$$

where

$\xi_0$  = peak displacement

$\mu_0$  = peak velocity

$i = \sqrt{-1}$

$\omega$  = angular frequency =  $2\pi f$ .

Therefore,

$$\mu_0 = i\omega \xi_0 = i(2\pi f)\xi_0. \quad (35)$$

Substituting equation (35) into equation (33), we obtain

$$p \cong 4\pi f^2 \rho a^2 \xi_0 \left(\frac{1}{r}\right) e^{ik(r-ct)}. \quad (36)$$

Equation (36) expresses the acoustic pressure at point P as a function of time (t). For the determination of acoustic pressure

---

<sup>7</sup>Beranek (6), p. 39.

patterns we are interested in the time average of this pressure.

Equation (36) will be modified accordingly.

Since

$$Ae^{+i\phi} = (A \cos \phi + iA \sin \phi), \quad (37)^8$$

$$e^{ik(r-ct)} = \cos [k(r-ct)] + i \sin [k(r-ct)]. \quad (38)$$

The exponential form is used only for mathematical convenience.<sup>9</sup>

In the real world we need consider only the real part of equation (38).

$$\text{Re}[e^{i\alpha}] = \cos (\alpha) \quad (39)$$

$$\text{Re}[e^{ik(r-ct)}] = \cos [k(r-ct)]. \quad (40)$$

Since

$$k = \frac{2\pi}{\lambda}, \quad (41)$$

$$k(r-ct) = \frac{2\pi}{\lambda} (r-ct) \quad (42)$$

$$k(r-ct) = 2\pi \left( \frac{r}{\lambda} - \frac{c}{\lambda} t \right). \quad (43)$$

And because

$$\lambda = \frac{c}{f}, \quad (44)$$

$$k(r-ct) = 2\pi \left( \frac{r}{\lambda} - ft \right). \quad (45)$$

Then

$$\text{Re}[e^{ik(r-ct)}] = \cos \left[ 2\pi \left( \frac{r}{\lambda} - ft \right) \right]. \quad (46)$$

---

<sup>8</sup>Morse (11), p. 8

<sup>9</sup>Morse (11), p. 9

Because we are not interested in the rapid (9240 oscillations per second) changes in (p) due to time, we can ignore this (ft) perturbation in equation (46).

$$\langle \text{Re}[e^{ik(r-ct)}] \rangle = \cos[2\pi\left(\frac{r}{\lambda}\right)] , \quad (47)$$

where

$$\langle X \rangle = \text{time average of } (X).$$

Substituting the result of equation (47) into equation (36), we obtain

$$\langle p \rangle \cong 4\pi f^2 \rho a^2 \xi_0 \left(\frac{1}{r}\right) \cos[2\pi\left(\frac{r}{\lambda}\right)] . \quad (48)$$

Equation (48) relates the time-averaged acoustic pressure at any arbitrary point (due to the vibration of a single block on the hologram) to the peak displacement of the block, as a function of the distance between the point and the block, the frequency of the vibration, the size of the block, and the density of the fluid medium. This equation is valid for any consistent set of units.

#### D. Development of the Algorithm

As was mentioned in the opening remarks of this section, the algorithm was developed to yield results which are directly comparable to the acoustic patterns measured at both Dodge Pond and the water tower. As a first attempt, the NUSC/NL UNIVAC 1108 computer was programmed to predict the acoustic pressure on the seventeen 1-foot-spaced contours of the 8-foot measurement sphere, detailed in Appendix A, similar to those obtained at the water tower. The choice of 17 contours proved adequate for the conclusions to be drawn from

this analysis. The acoustic pressure was computed at 36 points, spaced  $10^\circ$  apart, on each contour. The total number of points computed (612) consumed over 12 minutes of computer time when performed in floating-point arithmetic, and over 35 minutes when computed in double precision! Before delving into the more complicated details of the program, a brief overview of the chain of computations will be given.

For any given point on any given contour, it was necessary to compute the total acoustic pressure at that point. This total pressure ( $\phi$ ) is the vector sum of 3149 partial pressures. Each of these partial pressure vectors ( $d\phi$ ) was computed using the displacement value of one of the 3149 blocks on the hologram of the radiating surface. Both the magnitude and relative phase (either "+" or "-") of this displacement ( $\xi_0$ ) were stored in the computer memory in terms of fringe numbers. This later value was converted to displacement in centimeters by means of the equation (22) developed in section IV B. The partial acoustic pressure at the given point due to the single radiating block was computed using equation (48) of the preceding subsection. This equation utilizes the distance between the block and the point ( $r$ ) in two separate places. This distance changed for each block at each point and, therefore, needed to be computed 3149 times for each point on a contour. With the exception of the displacement ( $\xi_0$ ) and the distance ( $r$ ), all the remaining terms in equation (48) were constant throughout the analysis.

There were few analytical shortcuts which could be utilized in this lengthy computation. As a result, a standard flow chart of the program would reduce to a single long column of boxes showing 4

nested "DO LOOPS." To simplify matters, the program format will be listed below without the use of boxes and arrows. The "DO LOOPS" will, however, be indicated by "return" statements.

1. Start.
2. Read in the necessary physical constants such as frequency, speed of sound, distance between contours, etc.
3. Read in the holographic fringe data by rows (47 rows of 67 data points).
4. Compute the patterns for 17 evenly spaced contours, (J = 1 to 17).
5. Compute the total pressure for 36 points (every 10°) on the contour, (M = 1 to 36).
6. Select every row of the hologram, (K = 1 to 47).
7. Select every radiating block on the row, (L = 1 to 67).
8. Calculate the displacement in centimeters of the block from the holographic fringe data.
9. Compute the distance between the block on the radiating surface and the measurement point.
10. Compute the acoustic pressure at the point due to the radiating block.
11. Resolve this acoustic vector into its three Cartesian components.
12. Sum the resolved vector with the sum of the previous vector components.
13. Return to 7.
14. Return to 6.



15. Convert the three components of the total pressure at the point into a single vector.

16. Convert this linear vector into its decibel equivalent (referenced to 1  $\mu$ bar).

17. Print out this logarithmic value.

18. Return to 5.

19. Return to 4.

20. Stop.

Appendix C contains a listing of the FORTRAN IV program used on the UNIVAC 1108 computer. To speed up the processing, a few modifications were made to the straight line flow diagram simulated above. Since the contours at the very top and at the very bottom of the sphere are actually single-point measurements, that 1 point was computed, and the remaining 35 identical points on those contours were by-passed. Also, if the value of the displacement of a block was zero, that block could contribute no energy to the total pressure vector; thus all further calculations on that particular block were skipped. The only remaining modification was to compute the multiplication of the constant terms in equation (48) only once for the analysis.

Figure 31 illustrates the location of a selected measurement point  $P(X_P, Y_P, Z_P)$  with respect to a typical radiating block  $Q(X_Q = 0, Y_Q, Z_Q)$ . The first task at hand is to identify these two points in three-dimensional space. The height of point (P) above the equator of the measurement sphere was constrained to be an integral number of feet determined by the value of the "DO" variable (N) in step 4.

$$Y_p = N \cdot B, \quad (49)$$

where

$B$  = contour spacing interval in inches.

It is also known that the distance from the center of the vibrating plate to the measurement point ( $R$ ) must be exactly 8 feet. Figure 31 shows this distance as a vector ( $R$ ). The vector can be resolved into two components: one lying within the Cartesian ( $X, Z$ ) plane ( $R'$ ), and the other in the ( $Y, Z$ ) plane ( $R''$ ).

It is evident in figure 31 that ( $R''$ ) is equal to ( $Y_p$ ), which was computed in equation (49). ( $R'$ ) can now be computed:

$$R' = \sqrt{(R)^2 - (R'')^2} \quad (50)$$

$$R' \text{ (in inches)} = \sqrt{9216 - (N \cdot B)^2}, \quad (51)$$

where

$B$  = contour spacing in inches.

When pattern measurements were made at both Dodge Pond and the water tower, the starting point was taken in the direction of the back of the box. This was done purposely to allow uninterrupted recording of the acoustic pattern as the hydrophone passed in front of the radiating surface. For this reason, the angle of the measurement point with respect to the radiating surface ( $\theta$ ) was taken to be zero in the negative ( $X$ ) direction. This implies ( $\theta = 180^\circ$ ) directly in front at the box. This angle ( $\theta$ ) is easily calculated from the "DO" variable ( $M$ ) in step 5.

$$\theta \text{ (in radians)} = (M \cdot 10^\circ) \left( \frac{\pi \text{ radians}}{180^\circ} \right). \quad (52)$$

Having obtained  $(\theta)$ , we can resolve the vector  $(R')$  into its two Cartesian components  $(X_P)$  and  $(Z_P)$ :

$$X_P = R' \cos (\theta - \pi) \quad (53)$$

$$Z_P = R' \sin (\theta - \pi) , \quad (54)$$

where

$X_P$  and  $Z_P$  = the remaining Cartesian coordinates at point P in inches.

Since the radiating surface lies with the  $(Y, Z)$  plane,  $(X_Q)$  is zero. The other Cartesian coordinates of the individual radiating block  $(Y_Q)$  and  $(Z_Q)$  are calculated from the "DO" variables  $(K)$  and  $(L)$  in steps 6 and 7, respectively.

$$Y_Q = (24 - K) \cdot \text{COR} \quad (55)$$

$$Z_Q = (34 - L) \cdot \text{COR} , \quad (56)$$

where

$Y_Q$  and  $Z_Q$  = the coordinates of the radiating block Q in inches.

COR = hologram CORrection factor (11 inches/81 blocks).

NOTE: Since the center of the plate was taken as the origin of the coordinate system, and since the "DO" variables  $(K)$  and  $(L)$  range from (1 to 47) and (1 to 67), respectively,  $(Y_Q)$  and  $(Z_Q)$  will take on negative values depending upon the location of the particular block being studied.

Now that the Cartesian coordinates at the measurement point (P) and the radiating block (Q) are known, we can compute the exact distance between them  $(R)$  in inches:

$$R = \left[ (X_P)^2 + (Y_P - Y_Q)^2 + (Z_P - Z_Q)^2 \right]^{1/2}. \quad (57)$$

Figure 32 indicates the position of the vector (R) in three-dimensional space. In order to determine the two polar angles ( $\gamma$ ) and ( $\psi$ ) which define the direction of (R), it was necessary to resolve (R) into two components, (R') and (R''). The component in the (X, Z) plane (R'), is calculated from the geometry as

$$R' = \left[ (X_P)^2 + (Z_P - Z_Q)^2 \right]^{1/2}. \quad (58)$$

Having computed both (R) and (R') in equations (57) and (58), respectively, we can now calculate the two polar angles ( $\gamma$ ) and ( $\psi$ ).

$$\gamma = \sin^{-1} \left[ \frac{Y_P - Y_Q}{R} \right] \quad (59)$$

$$\psi = \sin^{-1} \left[ \frac{Z_P - Z_Q}{R'} \right]. \quad (60)$$

These polar angles will be used to resolve the acoustic pressure vector ( $d\phi$ ) at point P due to a single radiating block into its three Cartesian components, ( $d\phi_X$ ), ( $d\phi_Y$ ), and ( $d\phi_Z$ ).

Equation (48) relating the acoustic pressure at an arbitrary point to the displacement of a single vibrating block contains a string of five terms which are constant throughout the analysis. This chain multiplication will be computed only once and defined as the constant "AMP."

$$AMP = 4\pi f^2 \rho a^2, \quad (61)$$

where

$f$  = frequency of plate vibration in Hz

$\rho$  = density of water in gm/cm<sup>3</sup>

$a$  = one-half the holographic block length in cm

The frequency used at the water tower which resulted in the hologram of interest shown in figure 9 was 9240 Hz. The density of fresh water at 20°C and 100 feet of hydrostatic head can be obtained through linear interpolation of the values given in Table In-11 of the A.I.P. Handbook (18). This density is 0.998 gm/cm<sup>3</sup>. The term COR as introduced earlier in this section specifies the size of the square holographic blocks.

$$\text{COR} = \frac{11 \text{ inches}}{81 \text{ blocks}} = 0.1358 \frac{\text{inch}}{\text{block}} \quad (62)$$

Since (a) is the radius of the circle enclosed by each block, then the sides of these square blocks are (2a) in length. Equations (28) and (29) have solved for (a) given the value of COR as above. The result was

$$a = 0.0679 \text{ in.} \left( \frac{2.54 \text{ cm}}{\text{in.}} \right) = 0.1727 \text{ cm.} \quad (63)$$

Using all the above constant values in equation (61), we obtain

$$\text{AMP} = 4(3.14159) (9240)^2 (0.998) (0.1727)^2 \quad (64)$$

$$\text{AMP} = 3.194(10^7) \frac{\text{gm}}{\text{cm sec}^2} \quad (65)$$

In order that the algorithm could be rapidly changed to investigate other holograms at different frequencies, three terms,

frequency in kHz ( $f$ ), piston radius ( $a$ ) in terms of COR, and water density ( $\rho$ ), were left as separately changeable constants. Once set at the start of the program, the above value of AMP would be calculated by using a factor of  $2.032 (10^7)$  gm/cm $\cdot$ sec $^2$  times the same values of ( $f$ ), ( $\rho$ ), and COR.

Equation (48) contains a term which indicates the number of wavelengths ( $\lambda$ ) over which the partial acoustic pressure ( $d\phi$ ) had to travel in order to reach the measurement point P. This term,

$$\cos \left[ 2\pi \left( \frac{r}{\lambda} \right) \right], \quad (66)$$

has a value ranging from (-1) to (+1) depending on the value of the argument. This full range of values is covered for each integral number of wavelengths traveled. Thus, the only important portion is the magnitude of the last partial wavelength traveled. In effect, we can subtract the integral number from the quantity ( $r/\lambda$ ) and obtain the same final value by using the fractional portion only. This technique was used to simplify the study of the effect of the term in expression (66) during the verification phase of the programming. Subtraction of the integer value of the quantity ( $r/\lambda$ ) was most easily accomplished utilizing congruent arithmetic.

$$\alpha = \text{Modulo } [(r/\lambda), 1.]. \quad (67)$$

The term ( $\alpha$ ) in equation (67) will thus be calculated to be the fractional portion of the quantity ( $r/\lambda$ ).

Since all of the constants and variables in equation (48) have now been computed, it only remains to calculate the value of ( $d\phi$ ) through:

$$d\phi = \text{AMP} \cdot \xi_0 \left(\frac{1}{r}\right) \cos \left\{ 2\pi \cdot \text{mod} \left[ \left( \frac{r}{\lambda} \right), 1 \right] \right\}. \quad (68)$$

This partial acoustic pressure ( $d\phi$ ) at point P is a true vector having magnitude and direction. Its magnitude is computed in equation (68). Its direction is identical to that of the vector (R) shown in figure 32. The vector ( $d\phi$ ) can now be resolved into its three Cartesian components, ( $d\phi_x$ ), ( $d\phi_y$ ), and ( $d\phi_z$ ), using the previously computed angles of ( $\gamma$ ) and ( $\psi$ ). Figure 33 illustrates this decomposition.

$$d\phi_y = d\phi \sin \gamma \quad (69)$$

$$d\phi' = d\phi \cos \gamma \quad (70)$$

$$d\phi_x = d\phi' \cos \psi \quad (71)$$

$$d\phi_z = d\phi' \sin \psi \quad (72)$$

The algorithm computes these components for each ( $d\phi$ ) and sums these contributions separately. The total pressure ( $\phi$ ) at point P due to all 3149 blocks is determined from

$$\phi = \left[ \left( \sum_{i=1}^{3149} d\phi_{x_i} \right)^2 + \left( \sum_i d\phi_{y_i} \right)^2 + \left( \sum_i d\phi_{z_i} \right)^2 \right]^{1/2}. \quad (73)$$

Officer, (7) on page 29, lists the following equation for converting linear values of pressure ( $p$ ) into their logarithmic equivalent in decibels:

$$\text{Intensity (dB)} = 20 \log_{10} \frac{p}{p_0} \quad (74)$$

where

$p_0$  is any arbitrary reference pressure.

In underwater acoustics it is customary to let

$$p_0 = 1 \frac{\text{dyne}}{\text{cm}^2} = 1 \mu\text{bar}. \quad (75)$$

Thus,

$$\begin{aligned} \text{Intensity} &= 20 \log_{10} p \\ \text{dB}/1 \mu\text{bar} . \end{aligned} \quad (76)$$

The final value calculated in the algorithm is

$$\text{PHIDB} = 20 \log_{10}(\phi) , \quad (77)$$

where

$\text{PHIDB}$  = acoustic intensity level at point P due to the entire radiating surface, in decibels referenced to  $1 \mu\text{bar}$ .

#### E. Comparison of the Predicted and Measured Patterns

The acoustic pressure patterns of the seventeen 1-foot-spaced contours on the 8-foot measurement sphere, as computed using the algorithm developed in the preceding subsection, were glued to thin wooden sheets and a model was constructed similar to those made for the Dodge Pond and water tower measurements. This model can be observed in two views in figure 34, entitled "Hologram." When one compares the Hologram model to the Dodge Pond and Water Tower models shown in figure 23, it is immediately obvious that the predicted patterns bear no resemblance to the measured patterns! The measured



patterns are typical of monopole acoustic radiators; one large lobe of energy in the forward direction. The predicted patterns show a null or low point of acoustic intensity near the on-axis direction. The change from contour to contour is definite but in a smoothly varying manner. This latter fact indicates a deliberate rather than arbitrary change is occurring from pattern to pattern. The grotesque shape exhibited by this model can not easily be explained by combinations of simple acoustic sources. Indeed, the one-sidedness of the model bears no correlation to the fine symmetry indicated by figure 9, the (5, 5) mode from which this model was predicted!

An explanation as to why the predicted result differed vastly from the measured patterns will be presented in the next section.

## V. WHY AN OPTICAL HOLOGRAM WAS INSUFFICIENT FOR FAR-FIELD ACOUSTIC PREDICTION

### A. Monopole Patterns at Dodge Pond

The first indication that something was amiss in this experiment occurred during the Dodge Pond broad-band acoustic measurement phase reported in section III D. Although the (5, 5) mode patterns (9240 Hz) measured at the water tower agreed very well with those measured at Dodge Pond, the broad-band testing from 200 to 12,000 Hz showed monopole-type radiation at all frequencies. It had been expected that certain frequencies such as the (1, 2) mode at 1100 Hz and the (2, 1) mode at 660 Hz should produce dipole radiation patterns. They did not. Furthermore, it was expected that certain modes such as the (4, 2) at 2715 Hz (42°F) should produce patterns characteristic of quadripole radiation. This did not happen either. Extensive duplication of testing and calibration of the instrumentation proved that monopole radiation was occurring at all frequencies!

The on-axis acoustic pressure as measured 8 feet in front of the radiating surface is shown in figures 24 and 25 for the frequency band of 300 through 12,000 Hz. When the large acoustic pressure dip at 1731 Hz in figure 24 was observed, it was assumed that this was the null point for either a dipole or quadripole radiator. Patterns at this frequency were very disturbing because they still exhibited monopole-type radiation although the back of the box was radiating 15 dB more pressure than its open front! A possible explanation of this phenomenon will now be presented.

Figure 35 illustrates the complex construction of the soundbox and its thin radiating front plate. The plate was excited by the water in the box which was being insonified by the rather large AN/SQS-23 transducer element. The exact position of the transducer is not known but, after-the-fact measurements of the transducer length place it close to 13 inches from the rear wall of the box. This distance is referred to as ( $l_{back}$ ) in figure 35.

The SQS-23 element is a broad-band tuned-circuit device. It has a relatively flat ( $\pm 2$  dB) response from 3900 through 10,500 Hz. When this transducer was placed within the sound box, its frequency response, figure 25, was altered by the acoustical resonant modes of the transducer-box combination. The peaks in figure 25 are indications of a resonance or amplification within this system. The deep valleys are indications of sharp antiresonant conditions. It can be roughly stated that the average value seen in figure 25 between 4000 and 10,000 Hz is very close to the response measured with the transducer alone. The sharp roll-off with decreasing frequency below 4000 Hz is a result of the tuned circuit within the transducer element. In order to study the acoustics of this system below 4000 Hz it was necessary to change to the Navy standard J-9 transducer. This transducer is of cylindrical shape, 13 inches long, with its cable penetration coming out of the side rather than the end. Thus, the diagram shown in figure 35 holds for the J-9 transducer as well as for the SQS-23 element.

The J-9 transducer has a very flat response ( $\pm 1$  dB) from 300 to 3000 Hz. Above 3000 Hz its response raises a few dB up through 6000 Hz. The combination of the J-9 with the SQS-23 completely covers the frequency band of interest. Figure 24 has a couple of small

resonant peaks but the effect of those is almost insignificant compared to the large antiresonance evident at 1731 Hz. If the sound-box were constructed of a single common material and if the acoustic impedance of this material in water at 1731 Hz were known, and, furthermore, if the cavity were large with respect to the transducer, and the wall thickness was at least a significant portion of a wavelength; then, we could calculate at what frequency this antiresonance should occur. As one can presuppose, this is not the case with the box-transducer system shown in figure 35. The best that we can do is work backward from the known antiresonance frequency (1731 Hz), the dimension ( $l_{\text{back}}$ ), and the speed at sound ( $c = 1481 \text{ m/sec}$ ), and calculate the acoustical characteristic which the composite material (foam, steel, damping tile) appears to exhibit in this situation.

Using equations and constants previously introduced in section IV, we can determine the acoustic wavelength at 1731 Hz.

$$\lambda = \frac{c}{f} = \left( \frac{1481 \frac{\text{m}}{\text{sec}}}{1731 \frac{1}{\text{sec}}} \right) = 0.8556 \text{m} \quad (78)$$

$$\lambda = 0.8556 \text{m} \left( \frac{39.37 \text{ in.}}{\text{m}} \right) = 33.68 \text{ in.} \quad (79)$$

Acoustic energy leaves the face of the transducer shown in figure 35 and some of this energy propagates backwards into the box. After undergoing a phase change due to travel over the distance ( $l_{\text{back}}$ ), the energy impinges on the rear wall of the box. There it undergoes another phase change associated with the type of reflecting surface, and again travels over the distance ( $l_{\text{back}}$ ) to arrive at the face of the transducer. In the first antiresonant condition, this

reflected energy will be exactly  $180^\circ$  out of phase with the radiated energy at the face of the transducer, thereby significantly reducing the acoustic radiation in the forward direction. We know all of the necessary parameters of the box-transducer system except for the apparent acoustical impedance presented by the rear wall. We can, however, solve for the phase angle associated with the reflection from the composite surface.

$$l_{\text{back}} = 13 \text{ in.} \left( \frac{\lambda}{33.68 \text{ in.}} \right) = 0.3860 \lambda \quad (80)$$

at 1731 Hz

$$= 0.3860 \lambda \left( \frac{360^\circ}{\lambda} \right) = 138.9^\circ \quad (81)$$

$$2(l_{\text{back}} \text{ in deg}) + \angle_R = 180^\circ \quad (82)$$

where

$\angle_R$  = Angle of the Reflection coefficient.

$$2(138.9^\circ) + \angle_R = 180^\circ \quad (83)$$

$$\angle_R = 180^\circ - 277.9^\circ \quad (84)$$

$$\angle_R = -97.9^\circ \quad (85)$$

This reflection angle appears to be a realistic number if one considers that  $(\angle_R)$  for reflection from an infinitely solid surface is  $(0^\circ)$  (thereby causing pressure doubling at this surface), and for reflection from a perfect vacuum it is  $(-180^\circ)$ . Stephens and Date (19) show this angle to be the phase lag of the reflected wave compared to the incident pressure wave. Since  $(\angle_R)$  must lie between  $(0^\circ)$  and  $(-180^\circ)$ , the calculated angle of  $(-97.9^\circ)$ , being approximately half-way

between these extremes, is quite reasonable. Moreover, since this angle is not ( $0^\circ$ ) or ( $180^\circ$ ), then some energy absorption and/or transmission must have taken place within the material. The 1-inch-thick layer of viscoelastic damping tile can easily account for any apparent absorption of energy.

The other antiresonant conditions and, indeed, the resonances also, could be predicted if one only knew the apparent acoustical impedance of this composite layer which, most certainly, will vary with frequency. The gathering of such data would require extensive laboratory testing, time, and expense. In the end, such knowledge would not contribute to the basic premise of this dissertation, i.e., to determine if an optical hologram is sufficient for far-field acoustic prediction.

Returning to the main theme of this section, it may be said that acoustic patterns were made at at least a dozen frequencies within the range of 300 to 12,000 Hz. All of these patterns exhibited monopole radiation. The patterns at the lower frequencies approached omnidirectionality while those at the higher frequencies had as much as 30 dB front-to-back directionality. In essence, the transducer-box system behaved exactly like a closed-end organ pipe throughout the broad frequency range.

#### B. Equivalent Plane Wave Motion

In trying to assess why the patterns generated from the holographic input bore no resemblance to those actually measured, it was convenient to start in an area where everything was well defined and measured, i.e., the far field. In the far field, the relationships

between acoustic pressure, sound velocity, particle displacements, etc., are well established. Since we had measured the far-field pressures, and subsequently calibrated the hydrophones, we could determine the absolute acoustic pressure in the water within the accuracy of our hydrophone calibration ( $\pm 1$  dB).

The on-axis acoustic pressure level (L) at 9240 Hz, measured at 8 feet in the water tower was 38 dB on the polar recorder. The Ithaco gain ( $G_I$ ) had been set at +30 dB. Using equation (9) from section II C we can calculate the voltage on the cable ( $V_C$ ).

$$V_C + G_I = L - 45 \text{ dB} \quad (86)$$

$$V_C + 30 \text{ dB} = 38 \text{ dB} - 45 \text{ dB} \quad (87)$$

$$V_C = (38 - 45 - 30) \text{ dB} \quad (88)$$

$$V_C = -37 \text{ dB}/1V_{rms} \quad (89)$$

The voltage sensitivity of the LC-10 hydrophone which made this measurement was determined at Dodge Pond to be  $-114 \text{ dB}/1V_{rms}/\mu\text{bar}$ . (In an acoustic pressure field of strength 1  $\mu\text{bar}$ , this hydrophone will produce a voltage of 114 dB below 1  $V_{rms}$ .) This hydrophone calibration data agrees well with that sent by the manufacturer ( $-108 \text{ dB}/1V/\mu\text{bar}$ ) when one considers that the factor calibration included 30 feet of cable whereas the Dodge Pond calibration included the entire 140 feet of cable used at the water tower. The hydrophone sensitivity is flat ( $\pm 1$  dB) from 1 kHz through 40 kHz. The difference between the hydrophone output ( $-114 \text{ dB}/1V_{rms}$ ) for a 1  $\mu\text{bar}$  field,

and the measured level (-37dB//1Vrms) is a direct measurement of the acoustic field strength ( $\phi_8$ ) above 1 $\mu$ bar, i.e.,

$$\begin{array}{l} |114 - 37| \text{ dB} = \phi_8, \text{ in dB} \\ //1\text{Vrms} \quad //1\mu\text{bar} \end{array} \quad (90)$$

$$\phi_8 = +77 \text{ dB//1}\mu\text{bar} . \quad (91)$$

From figure 27, the Far-Field Test at 9240 Hz, it can be seen that the acoustic pressure dropped by 15 dB between the 1-foot and 8-foot positions. The pressure loss between the radiating surface and the 1-foot position was estimated to be a maximum of 5 dB, giving a total estimated propagation loss between the radiating plate and the 8-foot measurement point of 20 dB. Adding 20 dB to the pressure measured at the 8-foot distance gives an estimate of the acoustic pressure at the radiating surface ( $\phi_0$ ).

$$\phi_0 = +77 + 20 = +97\text{dB//1}\mu\text{bar} . \quad (92)$$

This logarithmic value can now be reduced to its linear equivalent pressure (p) in dynes/cm<sup>2</sup>.

$$\begin{array}{l} \phi_0 = 20 \log_{10} \frac{p}{1 \text{ dyne/cm}^2} \\ \text{in dB} \end{array} \quad (93)$$

$$97 \text{ dB} = 20 \log_{10} p \quad (94)$$

$$4.85 = \log_{10} p \quad (95)$$

$$p = \text{antilog}_{10}[4.85] = 7.08(10^4) \text{ dynes/cm}^2 \quad (96)$$



Bartberger (20) lists the following relationship for sinusoidal waves,

$$\xi = \frac{p}{\omega \rho c} \quad (97)$$

where

$\xi$  = particle displacement in cm

$p$  = acoustic pressure in dynes/cm<sup>2</sup>

$\omega = 2\pi f$

$f$  = frequency in Hz

$\rho$  = density of the medium

$c$  = wave speed in the medium.

Using our known values for the constants and pressure we get

$$\xi = \frac{7.03(10^4) \text{ dynes/cm}^2}{2\pi(9240 \text{ 1/sec})(.998 \text{ gm/cm}^3)(1.481 \times 10^5 \frac{\text{cm}}{\text{sec}})} \quad (98)$$

$$\xi = 8.25(10^{-6}) \text{ cm} . \quad (99)$$

The value of  $\xi$  above is an estimate of the equivalent plane-wave displacement at the radiating surface, which would produce an acoustic pressure of +77dB//1μbar when measured 8 feet away. Another way of looking at this statement is to say that if a very large plane surface, located in the plane of the vibrating plate were driven at 9240 Hz with an rms displacement of  $8.25(10^{-6})$  cm, then an acoustic pressure of +77dB//1μbar would be expected at a measurement point 8 feet distant.

The value of displacement given in equation (99) was inserted

into the UNIVAC 1108 program in lieu of the holographic data. This, in effect, implies that the whole 6-inch by 9-inch vibrating surface was moving as a rectangular piston of constant displacement. The results were very impressive; the patterns had the general monopole appearance seen in the actual measured data. A second computer run was made with the displacement increased by a factor of ten, i.e.,

$$\xi_{\text{new}} = 8.25(10^{-5}) \text{ cm} . \quad (100)$$

This correction factor is partially justifiable since the smaller displacement value was predicted for a large radiating surface, whereas the computer program was calculating pressures due solely to the limited 6-inch by 9-inch radiating surface.

A model was constructed using the patterns obtained with ( $\xi_{\text{new}}$ ) above. The result can be seen in two views in figure 34. The model shape is similar to those made from the measured data at both Dodge Pond and the water tower (shown in figure 23). Moreover, the on-axis acoustic pressure predicted by ( $\xi_{\text{new}}$ ) is +76dB//1 $\mu$ bar. This is within our accuracy limitation ( $\pm 1$  dB) of the measured on-axis pressure of +77dB//1 $\mu$ bar!

We know that the whole 6-inch by 9-inch area could not be vibrating with the uniform displacement ( $\xi_{\text{new}}$ ) because of the clamped edge condition. In order that the whole surface might have an average value of ( $\xi_{\text{new}}$ ) would imply that the center portion of the plate must move at considerably greater amplitude. Thus we might estimate a doubling of displacement value at the center to give

$$\xi_{\text{center}} = 1.65(10^{-4}) \text{ cm} . \quad (101)$$

Returning to figure 29, the graph of Displacement vs Fringe Number, the value of the second dark fringe is  $1.7(10^{-4})$  cm. Clearly, the in situ hologram at this frequency (the (5, 5) mode at 9240 Hz, figure 9) shows that a plane-wave bias level of about 2 dark fringes was not apparent near the center of the plate. Close analysis of figure 9 can show that if there were any plane wave bias present near the center of the plate, it must have been considerably lower than the value of the first dark fringe. This conclusion stems from the fact that one can trace several paths of null or no motion through the plate from top to bottom and from side to side.

On the other hand, the patterns generated by the modified equivalent plane-wave excitation agree very well with the measured results. In fact, Morse and Ingard (21) state that the expected beam pattern from a rectangular piston should be similar to that from a cylindrical piston; however, the pattern beamwidth should be greater in the direction of the smaller dimension. The equivalent plane-wave model seen in figure 34 matches this requirement since its greater beamwidth (the vertical) was in the direction of the shorter (6-inch) dimension. The plane-wave model also serves to verify the suitability of the algorithm and the resulting FORTRAN program developed in section IV D for the prediction of far-field acoustic patterns.

To summarize; the measured results appear to be highly correlated with the monopole radiation pattern predicted by a plane-wave displacement of magnitude equal to that corresponding to 2 dark fringes of holographic displacement near the center of the plate. However, analysis of the in situ hologram for this condition shows no such plane-wave motion existed. Clearly, something else was

happening. The next subsection will give a plausible explanation for this apparent controversy.

### C. Fresnel Diffraction Region

The preceding subsection introduced the paradox that plane-wave motion appeared to be occurring at the radiating surface, yet holograms of that surface indicate that plane-wave displacements of sufficient amplitude did not exist there. The key to this riddle can be found in figure 35. The radiating surface is shown placed a finite distance ( $\approx 3$  inches) in front of a finite-sized transducer. Kinsler and Frey (17), pages 176-7, address this problem for a circular piston and display a graph of the on-axis acoustic intensity versus distance from the transducer. Classical spherical spreading of acoustic waves does not begin until one reaches a certain distance in front of the transducer face. This distance is a function of the wavelength ( $\lambda$ ) and the piston radius ( $a$ ). Between this calculatable distance and the transducer face, the acoustic intensity varies between zero and a constant level, this level being the magnitude at the point where spherical spreading begins. As one proceeds from this point back toward the transducer, the intensity decreases until it actually becomes zero at a point which is referred to as the "last null." As one proceeds even closer the intensity increases rapidly to the constant value, then drops off sharply to another null. More and more peaks and nulls occur, separated by smaller and smaller distances as one approaches the face of the transducer. The region between this face and the point of spherical spreading is called the Fresnel Diffraction Region.

This phenomenon is common in the fields of acoustical,

optical, and electromagnetic radiation. It is a result of constructive and destructive interference along the on-axis line, due to interference from the separate regions of the finite-sized radiating source. If one measures pressure sufficiently far from the radiator, the distances between the measurement point and all of the separate radiating portions of the transducer appear approximately equal and thus the radiation from each segment is in phase with that from all of the others. In close proximity to the transducer, these distances become quite different. The outermost segments of the radiator being considerably more distant from the measurement point than the central portions of the radiator. These differences in distances cause corresponding differences in acoustic phase at the measurement point. The closer one gets to the surface, the more pronounced is the effect of phase interference.

In order to use the formula presented by Kinsler and Frey (17) for the distance to the last null, we must first obtain an approximation for the radius of an equivalent circular piston ( $a'$ ) because this experiment definitely had a rectangular source.

Kinsler and Frey (17) indicate that the beamwidth due to a circular piston is also a function of the radius ( $a$ ) and the wavelength ( $\lambda$ ).

$$\sin \theta = .61 \frac{\lambda}{a} \quad (102)$$

where

$\theta = 1/2$  the total beamwidth between nulls of the major lobe.

From the plane-wave patterns computed in the previous subsection, it can be found that the full beamwidth of the major lobe is

100°. Thus,

$$\theta_{\text{rectangle}} = 50^\circ. \quad (103)$$

Using this value in equation (102) we obtain the equivalent radius ( $a'$ ),

$$\sin \theta_{\text{rectangle}} = .61 \frac{\lambda}{a'} \quad (104)$$

$$\sin 50^\circ = .766 = .61 \frac{\lambda}{a'} \quad (105)$$

$$a' = \lambda \frac{.61}{.766} = .796 \lambda. \quad (106)$$

Using previously introduced values, we can obtain the wavelength ( $\lambda$ ) at 9240 Hz.

$$\lambda = \frac{c}{f} = \frac{1481 \text{ m/sec}}{9240 \text{ 1/sec}} = 0.1603 \text{ m} \quad (107)$$

$$\lambda = 0.1603 \text{ m} \left( \frac{39.37 \text{ in.}}{\text{m}} \right) = 6.31 \text{ inches} \quad (108)$$

Therefore, the equivalent circular radius ( $a'$ ) is:

$$a' = .796\lambda = .796(6.31 \text{ in.}) = 5.02 \text{ in.} \quad (109)$$

Kinsler and Frey (17), page 176 state that "The last null occurs in the vicinity of

$$r = \frac{a^2}{2\lambda}."$$
(110)

For our case,

$$r = \frac{(a')^2}{2\lambda} = \frac{(5.02)^2 \text{ in.}^2}{2(6.31) \text{ in.}} = 2.00 \text{ inches} , \quad (111)$$

For the sake of completeness we will also calculate the distance at which spherical spreading can be presumed to exist ( $r_{ss}$ ). Again from Kinsler and Frey (17), page 176,

$$r_{ss} = 2 \frac{(a')^2}{\lambda} \quad (112)$$

$$r_{ss} = 2 \frac{(5.02)^2 \text{ in.}^2}{6.31 \text{ in.}} = 7.99 \text{ inches} . \quad (113)$$

In summary, the 6-inch by 9-inch rectangular opening in the clamping ring appeared to behave similar to a circular piston of radius 5.02 inches. Using this value we can calculate that the last null of the Fresnel diffraction region in front of the transducer should have occurred in the vicinity of 2 inches in front of the transducer. Spherical spreading from this transducer is expected to begin at about 8 inches from the face. Since our radiating surface happened to be placed approximately 3 inches in front of the transducer face, it was located in a low intensity region of the monopole source providing the plate excitation. Thus, although a large amount of monopole energy was being produced by the transducer-box-radiating plate system, the location of the plate was such that it could not sense the presence of this energy.

#### D. Monopole Domination of the Far-Field Patterns Over-rides the Holographic Contribution

It was stated that the fine model generated by the computer analysis using plane-wave excitation is an indication of the

suitability of the computer program. If so, then the unbalanced patterns generated from the holographic input are probably true representations of the actual energy radiated from this (5, 5) mode excitation of the 6-inch by 9-inch clamped-edge plate. The total pressure in the far field should then be the sum of the monopole contribution and the contribution from the vibrating plate.

In all, four wooden models were constructed for this dissertation; these appear in figures 23 and 34. Below each model is a calibration chart. The 20° center sections of these charts were colored blue for the acoustic pressure range of 60 to 70dB//1μbar. The adjacent red band covers the range from 70 to 80dB//1μbar. The intersection of the colored sections is the 70 dB line. Each model has a different calibration level, primarily because the data was obtained from different sources, e.g., Dodge Pond, water tower, or computer output. It can be seen in figure 34 that the on-axis acoustic pressure of the Plane Wave model is considerably greater than that from the Hologram model. In fact, the monopole energy is 20 dB higher at this point. Since both the Dodge Pond model and the plane wave model are highly symmetrical, one can be fairly assured that the monopole component dominates the entire acoustic far field.

This experiment clearly demonstrates that an optical hologram of a vibrating surface is insufficient, by itself, for the prediction of acoustic far-field pressure patterns. There is a very important piece of information that is missing in a single hologram. In the prediction of far-field acoustic patterns from near-field pressure measurements, it is necessary to include the spatial gradient of these pressures in the calculations. Possibly, what is needed is the spatial



gradient of the holographic displacement in order to make valid predictions. The theory behind these gradients, their actual measurement, and their subsequent incorporation into the algorithm would be the subject of another large scale investigation.

Much was learned during this experiment which could serve as a guide for continued effort. At the present time, the writer envisions another rectangular cavity as the excitation source; only, this cavity would have perhaps 6 feet of length. The plate would again be bolted to the front of the cavity. The transducer inside would, however, be movable. Such motion should be remotely controllable with great accuracy. The material of the cavity should be solid steel on the inside surrounded by steel-reinforced concrete to provide the necessary wall stiffness with sufficient damping so that the whole structure would not vibrate, and to provide for the accurate calculation of the cavity resonant modes.

Holograms could be taken with the transducer at different distances from the radiating plate. Analysis of the change in holographic displacement with excitation distance could possibly provide the missing input data.

## VI. ANALYTICAL PREDICTION OF THE DYNAMIC BENDING STRESSES IN THE PLATE

### A. Introductory Remarks

This study was undertaken to support the claim made in Section III that the local bending stresses in the vibrating plate were well within the elastic region. In the elastic region, no permanent material deformation occurs after the removal of the disturbing forces.

An accurate calculation of all the local stresses incurred during vibration can be made using finite-element techniques with sophisticated computer programming. The implementation of these techniques requires extensive training and access to very elaborate computer facilities. Since it is only necessary in this section to demonstrate that the stress levels are below the yield point of the material, such accuracy is not needed and thus a more simplified approach can be employed. The whole 6 inch by 9 inch vibrating surface will be divided into 47 narrow horizontal bars placed side by side. The deflection at 67 points on each bar has been determined by holographic methods in the preceding sections. It will be shown that knowledge of the bar deformation, bar geometry, and the stiffness of the material is all that is required to calculate the bending stress along that bar.

The plate will also be divided into 67 narrow vertical bars placed side by side, and similar computations made for this representation. The bending stress at any point on the plate can,

therefore, be computed from two relatively independent sets of calculations. Ideally, these calculations would yield identical answers. As is to be expected, they did not yield the same answer in all cases; however, an estimate of the accuracy of this technique indicates that it is sufficient for our purpose.

#### B. Stress Prediction Along a Bar with Known Displacements

The maximum bending stress at any point on a bar occurs on the outermost fibers on the bar. This stress is related to the radius of curvature of the bar at that point. Marks (22), in his section on the "Deflection of Beams," gives the following relationship:

$$r = \frac{E \cdot I}{M}, \quad (114)$$

where

$r$  = radius of curvature at the point

$E$  = modulus of elasticity

$I$  = moment of inertia about the bar axis

$M$  = bending moment about this axis.

In the section on "Theory of Flexure" (page 431) Marks lists another expression for the bending moment.

$$M = \frac{S \cdot I}{c}, \quad (115)$$

where

$S$  = bending stress at outer fiber

$c$  = distance from the neutral (bar) axis to the outer fiber.

Substitution of the value of  $(M)$  given in equation (115) into equation (114), and re-arranging, we find

$$S = \frac{E \cdot c}{r} . \quad (116)$$

The maximum bending stress at a point is directly related to the elastic modulus of the material, and to the bar's half-width, and inversely to the radius of curvature at that point. Since  $(E)$  and  $(c)$  are constants for the entire plate, it is only necessary to calculate the radius of curvature at each point on each bar in order to predict maximum local bending stresses.

It must be remembered that this technique does not allow for deflection of the bar in the transverse direction. This fact accounts for the difference in our predicted stresses compared with those which one would obtain using finite-element techniques. If three adjacent bars had exactly the same deflections along their longitudinal axes, then the stresses predicted for the middle bar would indeed be quite accurate. This condition did exist for many sections of many bars (such as those crossing directly over broad anti-nodes), giving this simple technique considerable justification for a first-order investigation.

The radius of curvature for the arc which can be drawn through any 3 equi-spaced points is readily derived using standard trigonometric relationships. Johnson and LeBlanc (3), pages 6 through 9, present this derivation which concludes with the determination of three angles  $(\beta_1)$ ,  $(\beta_2)$ , and  $(\beta_3)$ . These angles and their relationship to the deflections of three arbitrarily selected consecutive

points are shown in figure 36. The radius of curvature at point (2) is also shown. Fortunately, the distance between points (1) and (2) is the same as that between points (2) and (3) and has been introduced earlier in this dissertation as the constant COR, where

$$\text{COR} = 11 \text{ inches/81 blocks.} \quad (117)$$

As a result, the angles  $(\beta_1)$ ,  $(\beta_2)$ , and  $(\beta_3)$  can be computed as below:

$$\beta_1 = \tan^{-1} \left[ \frac{Y_1 - Y_2}{\text{COR}} \right] \quad (118)$$

$$\beta_2 = \tan^{-1} \left[ \frac{Y_1 - Y_3}{2(\text{COR})} \right] \quad (119)$$

$$\beta_3 = \beta_2 - \beta_1 \quad (120)$$

Having determined  $(\beta_3)$ , Johnson and LeBlanc (3) show that the radius of curvature at point (2) can be computed by

$$r_2 = \frac{\text{COR}[1 + (\beta_3)^2]}{2\beta_3} \quad (121)$$

Returning to equation (116), we find that the maximum bending stress at point (2) can be computed.

$$\sigma_2 = \frac{E \cdot c}{r_2} \quad (122)$$

where

$\sigma_2$  = maximum bending stress at point (2) in lb/in.<sup>2</sup>

$E$  = plate modulus of elasticity in lb/in.<sup>2</sup>

$c$  = plate half-thickness in inches

$r_2$  = radius of curvature at point (2) in inches.

### C. Development of the Algorithm

A brief description of the algorithm will be presented, followed by more detailed explanation of some of the techniques employed. Appendix D contains a complete listing of this FORTRAN IV program.

In keeping with the simple format used in section IV D of this dissertation, the conventional flow chart will be dispensed with due to the straight line calculational procedure utilized. Again, "DO LOOPS" will be indicated by "return" statements.

1. Start.
2. Read in the necessary physical constants such as plate modulus of elasticity, plate half-width, and the number of the desired row and column to be investigated.
3. Read in the holographic fringe data by rows (47 rows of 67 data points).
4. Compute the displacement and maximum bending stress along the selected row.
  - a. Convert the holographic fringe data along the row into displacement in inches and store this information in a work vector, ( $K = 1$  to 67).
  - b. Return to 4a.
  - c. Using the work vector, compute the maximum bending stress for each of the 67 points along the row, ( $K = 2$  to 68).

d. Return to 4c.

e. Print the fringe number, the displacement, and the maximum bending stress for each element on the row.

5. Repeat all of (4.) above for the selected column, (K = 1 to 47).

6. Stop.

The only difficulty incurred in the development of this algorithm was in performing the computations for the first and last elements in the row (or column). Figure 36 indicates the geometry used to find the angles and radius of curvature for point (2). These calculations require knowledge of the displacement of point (1). When dealing with the first element of a row, there was no corresponding holographic data for the point immediately to the left, i.e., a point on the heavy clamping ring. We do know that the displacement on this ring was zero; therefore, a work vector was constructed to be 69 elements long. The first and last elements of this vector were set at zero amplitude. The amplitudes of the remaining 67 elements corresponded directly to the holographic row data. The second element, in the work vector contained the displacement in inches associated with the first element in the row. Thus

$$(\text{Vector Element})_{K+1} \leftrightarrow (\text{Row Element})_K . \quad (123)$$

After the work vector was computed, the angles ( $\beta_1$ ), ( $\beta_2$ ), and ( $\beta_3$ ), and the values of (r), the radius of curvature, and ( $\sigma$ ) the maximum bending stress could be computed for each point on the row.

In performing the calculations down the column, the only additional changes were to limit the "DO" variable "K" to 47 or 48 instead

of 67 or 68, and to set the amplitude of the 49th element of the work vector to equal zero.

The value of E, the modulus of elasticity for our 18-8 stainless steel plate, was taken from Marks (22), page 397.

$$E = 27.6(10^6) \text{ lb/in.}^2 \quad (124)$$

The value of displacement amplitude for the elements of the work vector were computed from the corresponding holographic fringe data using the non-linear equation (22) developed in section IV B, modified by the factor of 2.54 cm per inch.

$$\text{Vector}_{K+1} = [.09615(N_K) \mp .02265] \frac{.001}{2.54} \text{ inches ,} \quad (125)$$

where

$N_K$  = Holographic Fringe Number of the K'th element of the desired row or column.

The minus sign is to be used with positive values of ( $N_K$ ) and vice versa.

After calculating the displacements along the row (or column) and storing them in the work vector, the following calculations were performed for each element in the row (or column):

$$(\beta_1)_K = \tan^{-1} \left[ \frac{\text{Vector}_{K-1} - \text{Vector}_K}{\text{COR}} \right] \quad (126)$$

$$(\beta_2)_K = \tan^{-1} \left[ \frac{\text{Vector}_{K-1} - \text{Vector}_{K+1}}{2(\text{COR})} \right] \quad (127)$$



$$(\beta_3)_K = (\beta_2)_K - (\beta_1)_K \quad (128)$$

$$r_K = \frac{\text{COR}[1 + (\beta_3)_K^2]}{2(\beta_3)_K} \text{ inches} , \quad (129)$$

where

$r_K$  = radius of curvature at the K'th element of the work vector  
in inches.

And finally, we compute the maximum bending stress for the K'th element of the work vector ( $\sigma_K$ )

$$\sigma_K = \frac{E \cdot c}{r_K} \text{ lb/in.}^2 , \quad (130)$$

where

$E$  = plate modulus of elasticity in lb/in.<sup>2</sup>

$c$  = plate half-thickness in inches

$r_K$  = radius of curvature in inches.

All that remains is to print out the results. Since the (K+1)'th element of the work vector corresponds to the K'th element of the row (or column), the "DO" variable for the printing was set to range from 2 through 68 to yield the local stress for the 67 row elements across the plate. As a check, the input fringe numbers were also printed. This also allows for easy comparison of the input data with the calculated output.

#### D. Analysis of Results

The lower graphs on figures 37 and 38 indicate the predicted bending stresses along row 24 and column 34, respectively. The upper graphs show the holographic fringe numbers and their associated displacement values.

The first observation is that the graphs of fringe numbers and displacement are highly correlated. Perfect linear correlation cannot be obtained, however, due to the change of sign indicated in equation (22); the relationship between holographic fringe number and actual displacement.

The second observation is that the bending stress data are highly grouped; e.g., it appears that the calculated stress levels are either zero or  $\pm$  [1.7, 2.6, 3.5, or 4.5] Kpsi for the entire range between  $\pm 5$  Kpsi, with few intermediate values. This phenomenon occurs because the radius of curvature is dependent upon the second derivative of the bar deformation (or displacement). Timoshenko et al (23) prove that

$$\frac{1}{r_x} = - \frac{\partial^2 W}{\partial X^2}, \quad (131)$$

where

$r_x$  = radius of curvature in the x-direction

$W$  = deflection normal to the plane of the plate .

An identical equation holds for the radius of curvature in the other planar direction.

Thus, although the curves of bar displacement in figures 37 and 38 appear quite smooth, the second derivatives (and thereby the local radius of curvatures and the local bending stresses) are quite scattered. Moreover, these calculated stresses tend to fall in certain quantized levels determined by the minimum change between consecutive points on the deformation curve. This minimum change is nominally one-half of a fringe number. An exception occurs with the first half-fringe. There is no  $\pm 0.5$  fringe number. The first identifiable holographic fringe is the first dark fringe, i.e.,  $\pm 1.0$ .

This latter fact also accounts for the largest predicted stress levels on both figures! These largest stresses are all associated with the zero-crossings of the deflection curves. Since our smallest quantizing increment for deflection in this region is  $\pm 1.0$  dark fringe, the second derivative of this inaccuracy causes a highly amplified inaccuracy in stress predictions for these regions. Knowing of this limitation, one can ignore the values of predicted stresses in these regions.

Thus, not using those points known to be highly inaccurate, the largest bending stresses across row 24 were  $\pm 3.5$  Kpsi. The largest (reliable) bending stress down column 24 was  $+3.5$  Kpsi. Marks (22), page 563, lists the yield strength for 18-8 stainless steel as 30 Kpsi. It is apparent that the local bending stresses across the plate are about an order of magnitude below the yield point. This statement was further substantiated by calculations performed across row 41 and down column 60.

The intersection point of the selected row and column provides a check on the accuracy of the algorithm. If everything were perfect,

the stress predicted for the 34th element on row 24 should be identical to that predicted for the 24th element on column 34 since they are indeed the same point. These two stresses, however, were calculated from 5 different values of displacement data, only one of which was common to both calculations. In figure 37, the stress on element 34 of row 24 was zero. In figure 38, the stress on element 24 of column 34 was +1.7 Kpsi. These values differ by only one quantizing level (less than 6 percent of yield strength). The predicted stress levels for the intersection point for row 41 and column 60 were identical. This provides a reasonable estimate for the accuracy of our calculations, i.e.,  $\pm 1$  quantizing level.

It appears that holographic techniques can provide for dynamic bending stress predictions, without loading the vibrating surface, to an accuracy of better than 6 percent of yield strength. This accuracy is quite compatible with that obtained through conventional strain-gage measurements. Moreover, the strain-gage stress data has been integrated over a larger surface area, and thus this data suffers from smoothing. Strain-gage measurements are also highly sensitive to thermal gradients, and their mass can cause loading on very thin plates. It appears that interferometric holography can provide valuable stress data in experiments which could not normally employ other, more conventional stress measurement techniques.

## VII. CONCLUSIONS

This dissertation was successful in providing insight into the interrelationship of a vibrating plate, its hydraulically coupled excitation system, its holographic displacement data, and the resulting acoustic pressure patterns. In the execution of the experimental phase, modern electronic equipment was extensively employed together with sophisticated data recording and processing methods. This resulted in new applications of holography in the determination of the interaction of surface vibration with sound and the determination of dynamic bending stress. The primary conclusion of this dissertation is that a single interferometric hologram of a vibrating surface is insufficient for the accurate prediction of far-field acoustic pressure patterns. Patterns predicted using the data from a hologram of the vibrating face of a special sound box bore no correlation to the actual measured patterns. These latter patterns showed that the far field was completely dominated by monopole radiation coming from the sound box. Careful study of the hologram of the face of this source showed no evidence of the planar motion normally associated with this monopole radiation. Substitution of this piston-like planar motion into the computer program in place of the holographic displacement information yielded results comparable to those actually measured, and with the characteristic shape associated with rectangular pistons. Analytical investigations indicate that the plane of the hologram (the front of the sound box) was near the last null of the Fresnel

diffraction region of the transducer enclosed by the box. In such a location, destructive interference occurs between the separate portions of monopole energy radiated by the different areas on the finite-sized transducer face. Thus, although a large amount of monopole energy was being radiated by the sound box, the hologram could not sense this acoustic motion, because of the arbitrary position of the front face.

In order for the holographic technique to succeed, additional information will be required. Perhaps the gradient of displacement can provide this key. The measurement of such a gradient and its incorporation into a suitable algorithm will require another carefully designed, long-term experiment, suggestions for which have been given in the text.

An important aspect of this research was the prediction of the dynamic bending stresses on the vibrating plate using the holographic information. The predicted results were quite reasonable with accuracies approximating those which can be obtained by use of conventional strain-gage techniques. Plus, the holographic method predicts the stress everywhere on the plate versus the single result, averaged over a larger area, for the conventional method. Other advantages, such as the noncontacting nature of holography and relative immunity from thermal gradients, extend the applicability of the holographic method.

In the field of holography, this dissertation reduced the computational complexity of converting the holographic fringe data into displacement, when multiple calculations (such as computer applications) must be made. A non-linear equation was fitted to calculated

results in a manner that held the estimated error to less than 1 percent of the value of the displacement corresponding to a single fringe over the range of +5 to -5 dark fringes! Near-perfect correlation was demonstrated between the fringe data and the calculated displacement values using this non-linear equation.

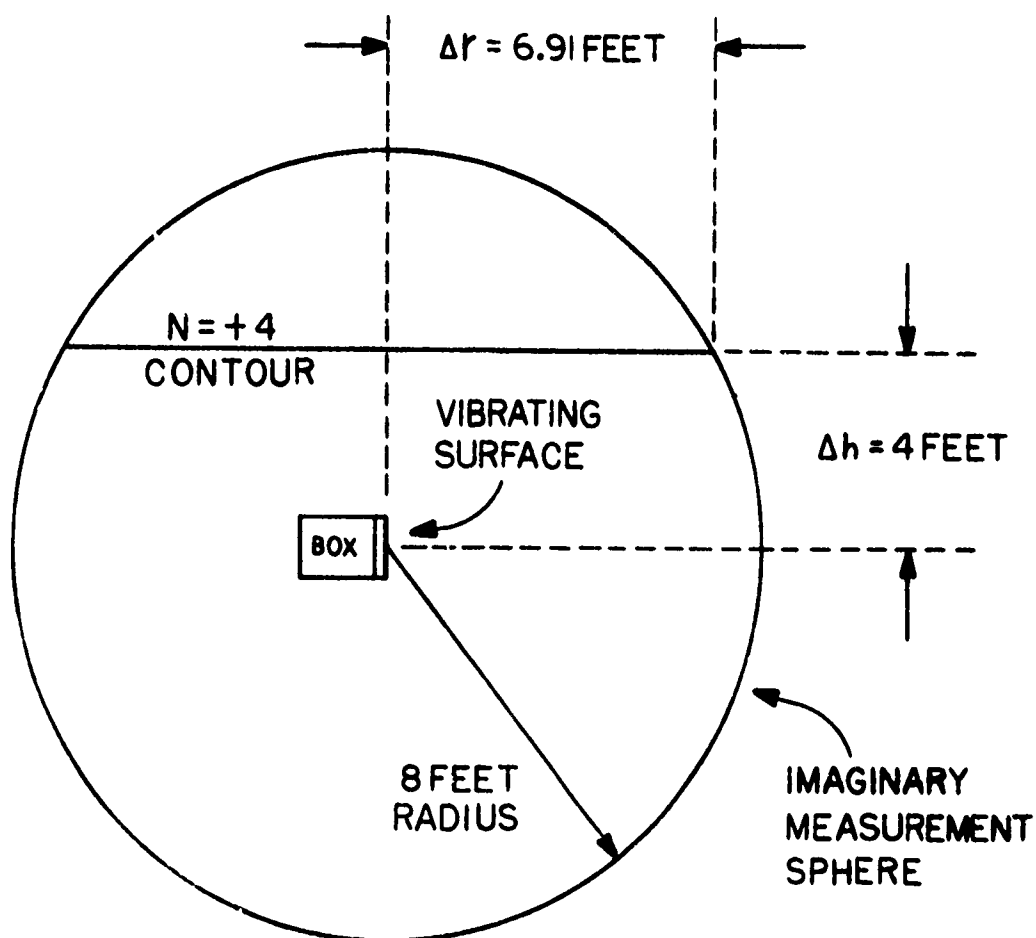
The eigenvalues or natural frequencies of the vibrating plate were determined by use of holographic techniques from zero through 6000 Hz. Changes in eigenvalues as a function of temperature can account for the observed eigenvalue shift between the laboratory measurements and similar measurements made at the water tower.

In conclusion, this research required careful experimental design. The mechanical apparatus performed flawlessly. The acoustic measurements made at the water tower, using remote control methods, compared very well with those obtained at the highly sophisticated Dodge Pond acoustic measurement facility. The primary electronic pulsed-acoustic measurement system operated reliably; however, the back-up automatic data collection system failed at the eleventh hour. The value of redundant experiment design was greatly appreciated at that particular time!

The entire experiment can form the basis for future experimental and analytical work related to the transformation of vibrational energy of complex surfaces into acoustic radiation patterns.

## APPENDIX A

## DETAILS OF THE MEASUREMENT SPHERE

POSITION OF THE  $N=+4$  CONTOUR IS SHOWN

ELEVATION VIEW



TABLE A1

HEIGHT ABOVE THE EQUATOR ( $\Delta h$ ) AND CONTOUR  
RADIUS ( $\Delta r$ ) FOR THE 8 FOOT DIAMETER  
MEASUREMENT SPHERE

$\Delta h$ (feet)	$\Delta r$ (feet)	$\Delta h$ (feet)	$\Delta r$ (feet)
-0-	8.0	-	-
+0.5	7.98	-0.5	7.98
+1.0	7.93	-1.0	7.93
+1.5	7.83	-1.5	7.83
+2.0	7.75	-2.0	7.75
+2.5	7.59	-2.5	7.59
+3.0	7.41	-3.0	7.41
+3.5	7.18	-3.5	7.18
+4.0	6.91	-4.0	6.91
+4.5	6.60	-4.5	6.60
+5.0	6.22	-5.0	6.22
+5.5	5.79	-5.5	5.79
+6.0	5.28	-6.0	5.28
+6.5	4.65	-6.5	4.65
+7.0	3.86	-7.0	3.86
+7.5	2.75	-7.5	2.75
+8.0	-0-	-8.0	-0-

**APPENDIX B**

**The Holographic Fringe Data Corresponding to Row 5**



## APPENDIX C

FORTRAN IV Listing of:

"Prediction of the Far-Field Acoustic Pattern of  
a Vibrating Source Using a Holographic Input"

1\* PRODUCTION OF THE FAR FIELD ACOUSTIC PATTERN OF A VIBRATING SOURCE US  
2\* THIS A HOLOGRAPHIC INPUT

3\* THE CONTOURS USED IN THIS ANALYSIS ARE EQUI-SPACED HORIZONTAL SLICES  
4\* 2THRU A SPHERE OF 8 FEET RADIUS, WITH THE FLAT PLATE ACOUSTIC SOURCE  
5\* BE LOCATED AT ITS CENTER

6\* THE HOLOGRAM OF THE 6 X 9 INCH VIBRATING PLATE WILL BE DIVIDED INTO 4  
7\* 47 CWS AND 67 COLUMNS, CREATING 3149 BLOCKS

8\* DIMENSION KING(47,67),PHI(36),PHIDB(36)  
9\* DOUBLE PRECISION PHI,PHIDB,PSI,LAMBDA,B,RHOC,C,FREQ,FREQSQ,COR,  
10\* CORSQ,AMP,RING,PRIME,THETA,X,Y,Z,APHIX,APHY,APHIZ,YD,IG,ZDSIG  
11\* ZKON,GMMA,RLAM,DISPL,DPHI,DPHIPR,DPHIX,DPHIY,DPHIZ,PI,R

12\* THE INITIAL PARAMETERS

13\* BE VERTICAL SEPARATION BETWEEN CONTOURS IN INCHES

14\* BE12.

15\* RHO=DENSITY OF THE FLUID IN GMS PER CC

16\* RHU=0.928

17\* CS=SPEED OF SOUND IN THE MEDIA IN METERS PER SECOND

18\* CS=1481.

19\* FREQ=ACOUSTIC SOURCE FREQUENCY IN KHZ.

20\* FREQ=9.240

21\* COR=HOLOGRAM SCALING FACTOR IN INCHES PER BLOCK

22\* COR=11./81.

23\* LAMBDA=ACOUSTIC WAVELENGTH IN CM

24\* LAMBDA=(C/FREQ)/10.

25\* FREQSQ=FREQ\*FREQ

26\* CORSQ=COR\*COR

27\* AMP=20320000\*FREQSQ\*RHOC\*CORSQ

28\* PI=DACUS(-1.2)

29\* READ IN THE HOLOGRAPHIC DATA BY ROWS

30\* READ(3,2)((RING(J,K),K=1,67),J=1,47)

31\* FORMAT(3(17D4.1/),16U4.1)

```

30*      COMPUTE THE ACOUSTIC PRESSURE, PH, AT 36 EVENLY SPACED INCREMENTS AROUND
39*      SOUND EACH OF THE 17 CONTOURS
40*      DO 104 J=1,17
41*      N=NAME OF THE CONTOUR
42*      N=-9+J
43*      RPRIME=DSQRT(9216.-(N*B)*(N*B))
44*      IF(J-1)101,101,106
45*      IF(J-17)107,101,101
46*      MMXX=36
47*      GO TO 102
48*      MMXX=1
49*      DO 103 M=1,MMXX
50*      THETA=M*10.*PI/180.
51*      X=PRIME*DCOS(THETA-PI)
52*      Z=PRIME*DSIN(THETA-PI)
53*      APXIX=0.
54*      APHIY=0.
55*      APXIZ=0.
56*      THIS SECTION COMPUTES THE CARTESIAN COORDINATES OF THE CENTERS OF THE
57*      6 INDIVIDUAL BLOCKS IN INCHES. NOTE XUSIG=0 FOR ALL BLOCKS
58*      DO 105 K=1,47
59*      DO 105 L=1,67
60*      IF(RING(K,L))108,105,108
61*      YDSIG=(24-K)*COR
62*      ZDSIG=(34-L)*COR
63*      R=DISTANCE BETWEEN THE BLOCK AND THE CONTOUR POINT IN INCHES
64*      R=DSQRT(X*X+(Y-YDSIG)+(Y-YDSIG)+(Z-ZDSIG)*(Z-ZDSIG))
65*
66*      GA=MA=DA=ASIN((Y-YDSIG)/R)
67*      PS1=DA=ASIN((Z-ZDSIG)/RPRIME)
68*      RCM= R IN CM
69*      RC4=R*1000./3937.
70*      RLAM=NUMBER OF WAVELENGTHS TRAVELED
71*      RLAM=RCM/LAMBDA
72*
73*
74*

```

```

15*      THIS SECTION CONVERTS THE RING NUMBER TO DISPLACEMENT IN CM
16*      IF(RING(K,L))109,109,110
17*      109  DI,PL=(.09615*RING(K,L)+.02265)*.001
18*      GO TO 111
19*      110  DI,PL=(.09615*RING(K,L)+.02265)*.001
20*      UPHI= ACOUSTIC PRESSURE DUE TO ONE BLOCK
21*      DPHI=(AMP*DISPL/RCM)*UCOS(2.*PI*DMOD(RLAM,1.))
22*
23*      THIS SECTION RESOLVES THE VECTOR DPHI INTO ITS THREE COMPONENTS
24*      DPHIX=DPHI*DSIN(GAMMA)
25*      DPHIY=DPHI*DCOS(GAMMA)
26*      DPHIZ=DPHI*DCOS(GAMMA)
27*      DPHIX=DPHI*DCOS(GAMMA)
28*      DPHIZ=DPHI*DCOS(GAMMA)
29*
30*      THIS SECTION ADDS THE COMPONENT VECTORS SEPARATELY, THEN FINALLY COMBINES
31*      THEM INTO THE VECTOR PHI, WHICH IS THE ACOUSTIC PRESSURE AT THE
32*      MEASUREMENT POINT, IN DYNES PER SQUARE CM, DUE TO ALL 3149 SOURCES
33*      APHIX=DPHIX+DPHIX
34*      APHIY=DPHIY+DPHIY
35*      APHIZ=DPHIZ+DPHIZ
36*      CONTINUE
37*      PHI(M)=DSQRT(APHIX*APHIX+APHIY*APHIY+APHIZ*APHIZ)
38*
39*      WE NOW CONVERT PHI INTO DB REFERENCED TO 1 DYNE PER SQUARE CM
40*      PHIDB(M)=20.*DLOG10(PHI(M))
41*      CONTINUE
42*
43*      PRINT OUT THE DESIRED RESULTS
44*      WRITE(4,1)N,(PHIDB(M),M=1,36)
45*      FORMAT(//'/ ' ACOUSTIC PRESSURE FOR 36 EVENLY SPACED INCREMENTS A
46*      ROUND THE DELTA H EQUALS '13.' FEET CONTOUR, IN DB REF 1 DYNE PER
47*      SQUARE CM.'//,12(2X,DB.3))
48*      CONTINUE
49*      STOP
50*      END

```

END OF H-IVAC 1108 FORTRAN V COMPILATION. 0 \*DIAGNOSTIC\* MESSAGE(S)

**APPENDIX D****FORTRAN IV Listing of:**

**"Calculation of the Maximum Bending Stresses Through  
Any Desired Horizontal and/or Vertical Sections  
of a Vibrating Plate, Using a Holographic Input"**



```

1* C CALCULATION OF THE MAXIMUM BENDING STRESSES THRU ANY DESIRED
2* C HORIZONTAL AND/OR VERTICAL SECTIONS OF A VIBRATING PLATE, USING
3* C A HOLOGRAPHIC INPUT
4* C
5* C
6* C THE HOLOGRAM OF THE 6 X 9 INCH VIBRATING PLATE WILL BE DIVIDED INTO 4
7* C 47 ROWS AND 67 COLUMNS, CREATING 3149 BLOCKS
8* C
9* C DIMENSION RING(47,67), VECTOR(69), SIGMA(68)
10* C
11* C SET THE INITIAL PARAMETERS
12* C II=DESIRED ROW NUMBER
13* C II=24
14* C JJ=DESIRED COLUMN NUMBER
15* C JJ=34
16* C CORE=HOLOGRAM SCALING FACTOR IN INCHES PER BLOCK
17* C CORE=11./81.
18* C C=ONE HALF OF THE PLATE THICKNESS
19* C C=.125/2.
20* C E=PLATE MODULUS OF ELASTICITY IN LBS. PER SQ. IN.
21* C E=27600000
22* C
23* C READ IN THE HOLOGRAPHIC DATA BY ROWS
24* C HEAD(3,2)((RING(J,K),K=1,67),J=1,47)
25* C FORMAT(3(17F4.1),16F4.1)
26* C
27* C COMPUTE THE BENDING STRESSES ALONG ROW II
28* C WRITE(4,6)II, (RING(II,K),K=1,67)
29* C FORMAT(//'/') THE FRINGE NUMBERS ACROSS ROW ',12, //10(3X,E8.3))
30* C VECTOR(1)=0.
31* C VECTOR(69)=0.
32* C DO 103 K=1,67
33* C VECTOR(K+1)=RING(II,K)

```

```

34* C THIS SECTION CONVERTS THE HOLOGRAM KING NUMBER TO DISPLACEMENT IN IN.
35* IF(VECTOR(K+1))105,103,101
36* VECTOR(K+1)=(.09615*VECTOR(K+1)+.02265)*.001/2.54
37* GO TO 103
38* VECTOR(K+1)=(.09615*VECTOR(K+1)-.02265)*.001/2.54
39* CONTINUE
40* WRITE(4,1)11,(VECTOR(M),M=2,68)
41* FORMAT(//)/// THE DISPLACEMENT ALONG ROW ',12,' IN INCHES'//,
42* Q10(3X,E8.3)
43* C VECTOR(K) NOW CONTAINS THE DISPLACEMENT INFORMATION ALONG THE ROW
44* C INCLUDING AN EXTRA ELEMENT, ON EACH END, OF ZERO DISPLACEMENT
45* C WHICH REPRESENTS THE CLAMPED EDGES
46* C
47* C USING THE DISPLACEMENT DATA, THE MAXIMUM BENDING STRESS, SIGMA, WILL
48* C BE COMPUTED USING RMIN, THE RADIUS OF CURVATURE AT THE POINT OF
49* C INTEREST
50* C
51* C RMIN WILL, IN TURN, BE COMPUTED FROM THREE ANGLES, BETA1,2,AND3,
52* C AS DESCRIBED IN THE TEXT
53* C DO 109 K=2,68
54* BETA1=ATAN((VECTOR(K-1)-VECTOR(K))/COR)
55* BETA2=ATAN((VECTOR(K-1)-VECTOR(K+1))/(2.*COR))
56* BETA3=BETA2-BETA1
57* RMIN=COR*(1.+BETA3*BETA3)/(2.*BETA3)
58* SIGMA(K)=E*C/RMIN
59* CONTINUE
60* C NOTE, HERE, SIGMA(K+1) IS THE STRESS ASSOCIATED WITH ELEMENT(K) IN ROW
61* C 11, SIGMA(1) IS UNUSED
62* C WRITE(4,3)11,(SIGMA(K),K=2,68)
63* C FORMAT(//)/// THE BENDING STRESSES ALONG ROW',12,' IN LBS. PER SQ.
64* C INCH'//,10(2X,E8.3)
65* C
66* C

```

```

67* C COMPUTE THE BENDING STRESSES ALONG COLUMN JJ
68* WRITE(4,7)JJ,(RING(K,JJ),K=1,47)
69* VECTOR(49)=0.
70* FORMAT(/////,' THE FRINGE NUMBERS DOWN COLUMN ',12,/,10(3X,E8.3))
71* DO 104 K=1,47
72* VECTOR(K+1)=RING(K,JJ)
73*
74* C THIS SECTION CONVERTS THE HOLOGRAM RING NUMBER TO DISPLACEMENT IN IN.
75* IF(VECTOR(K+1))107,104,102
76* 107 VECTOR(K+1)=(.09615*VECTOR(K+1)+.02265)*.001/2.54
77* GO TO 104
78* 102 VECTOR(K+1)=(.09615*VECTOR(K+1)-.02265)*.001/2.54
79* 104 CONTINUE
80* WRITE(4,4)JJ,(VECTOR(M),M=2,48)
81* FORMAT(/////,' THE DISPLACEMENT ALONG COLUMN ',12,,' IN INCHES'//
82* 0,10(3X,E8.3))
83* DO 110 K=2,48
84* BETA1=ATAN((VECTOR(K-1)-VECTOR(K))/COR)
85* BETA2=ATAN((VECTOR(K-1)-VECTOR(K+1))/(2.*COR))
86* BETA3=BETA2-BETA1
87* RMIN=COR*(1.+BETA3*BETA3)/(2.*BETA3)
88* SIGMA(K)=E*C/RMIN
89* CONTINUE
90* 110 WRITE(4,5)JJ,(SIGMA(K),K=2,48)
91* 5 FORMAT(/////,' THE BENDING STRESSES ALONG COLUMN ',12,,' IN LBS. PER
92* 0 50. IN. ',10(3X,E8.3))
93* STOP
94* END

```

END OF UNIVAC 1108 FORTRAN V COMPILATION. 0 \*DIAGNOSTIC\* MESSAGE(S)

## APPENDIX E

## References Cited

1. Eberhardt, F. J., and Andrews, F. A., "Laser Heterodyne System for Measurement and Analysis of Vibration," *J. Acoust. Soc. Am.*, 48 (1970), 603-9.
2. Chertock, G., "Sound Radiation from Vibrating Surfaces," *J. Acoust. Soc. Am.*, 36 (1964), 1305-13.
3. Johnson, C. D., and LeBlanc, C. L., *Interferometric Holography Techniques Applicable to Sonar Transducer Investigations*, U. S. Navy Underwater Sound Laboratory Report No. 876, New London, Conn., 11 April 1968.
4. Peterson, A. P. G., and Gross, E. E., *Handbook of Noise Measurement*, 6th ed., General Radio Company, West Concord, Mass., 1967, p. 19.
5. Ungar, E. E., "Highly Damped Structures," *Machine Design*, February 14, 1963.
6. Beranek, L. L., *Acoustics*. New York: McGraw-Hill Book Company, Inc., 1954, pp. 11-13.
7. Officer, C. B., *Introduction to the Theory of Sound Transmission*. New York: McGraw-Hill Book Company, Inc., 1958, pp. 28-29.
8. Deutsch, R., *Nonlinear Transformations of Random Processes*. Englewood Cliffs, New Jersey: Prentice-Hall, Inc., 1962, p. 128.
9. Telemetry Working Group, Inter-Range Instrumentation Group, Range Commanders Council, *Telemetry Standards, Revised February 1969*. New Mexico: White Sands Missile Range Document 106-69.
10. Drucker, D. C., *Introduction to Mechanics of Deformable Solids*. New York: McGraw-Hill Book Company, Inc., 1967, p. 86.
11. Morse, P. M., *Vibration and Sound*. 2nd ed. New York: McGraw Hill Book Company, Inc., 1948, pp. 326-328.
12. Powell, R. L., and Stetson, K. A., "Interferometric Vibration Analysis by Wavefront Reconstruction," *J. Opt. Soc. Am.*, 55:12 (1965), 1593-8.

13. Horvath, V. V., and Wallach, J., *Holographic Interferometry Applied to Experimental Mechanics*, General Electric Research and Development Center Report No. 70-C-352, Schenectady, New York, October 1970.
14. Shortley, G., and Williams, D., *Elements of Physics*. 2nd ed. Englewood Cliffs, New Jersey: Prentice-Hall, Inc., 1955, p. 466.
15. *Handbook of Chemistry and Physics*. 51st ed. Cleveland: The Chemical Rubber Co., 1970, p. E230.
16. Watson, G. N., *A Treatise on the Theory of Bessel Functions*. 2nd ed. Cambridge: Cambridge University Press, 1966, p. 748.
17. Kinsler, L. E., and Frey, A. R., *Fundamentals of Acoustics*. 2nd ed. New York: John Wiley and Sons, Inc., 1962, pp. 169-77.
18. *American Institute of Physics Handbook*. New York: McGraw-Hill Book Company, Inc., 1957, p. 2-153.
19. Stephens, R., and Bate, A., *Acoustics and Vibrational Physics*. New York: St. Martin's Press, 1966, p. 660.
20. Bartberger, C. L., *Lecture Notes on Underwater Acoustics*, Defense Documentation Center No. AD 468869, Cameron Station, Alexandria, Va., 1965, p. 16.
21. Morse, P., and Ingard, K., *Theoretical Acoustics*. New York: McGraw-Hill Book Company, Inc., 1968, pp. 392-3.
22. Marks, L. S., *Mechanical Engineers' Handbook*. 5th ed. New York: McGraw-Hill Book Company, Inc., 1951, p. 437.
23. Timoshenko, S. et al., *Theory of Plates and Shells*. New York: McGraw-Hill Book Company, Inc., 1959, p. 34.



FIGURE 1

Sound box on tripod at bottom of water tower

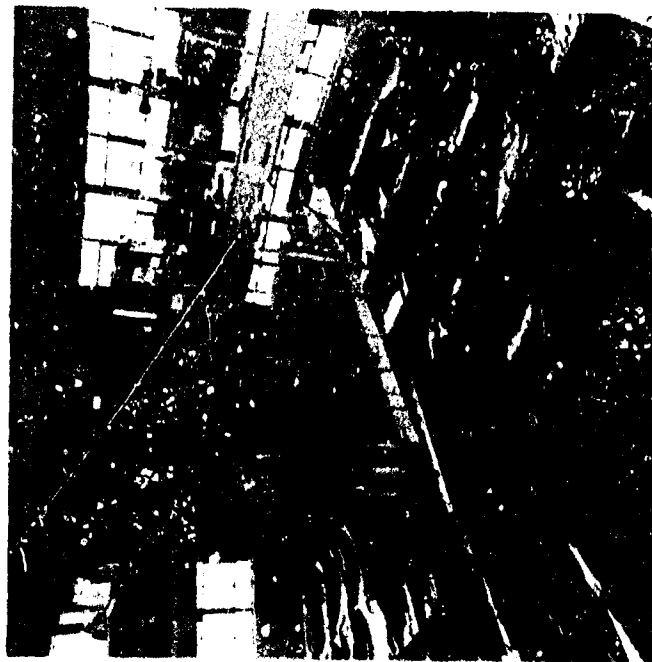


FIGURE 2

Rotator on drawbridge at top of water tower

Naval Underwater Systems Center  
NP24 - 47055 - 10 - 72

Official Photograph

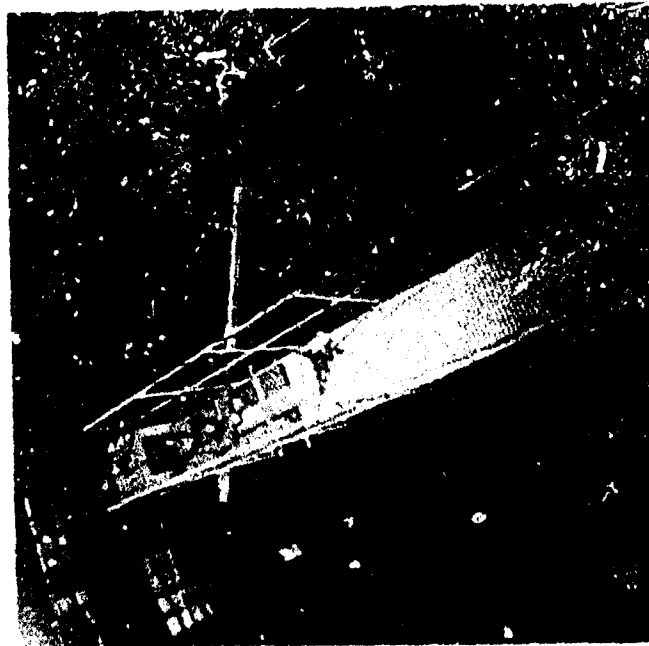


FIGURE 3

Looking down into the water tower

Naval Underwater Systems Center  
NP24 - 47057 - 10 - 72

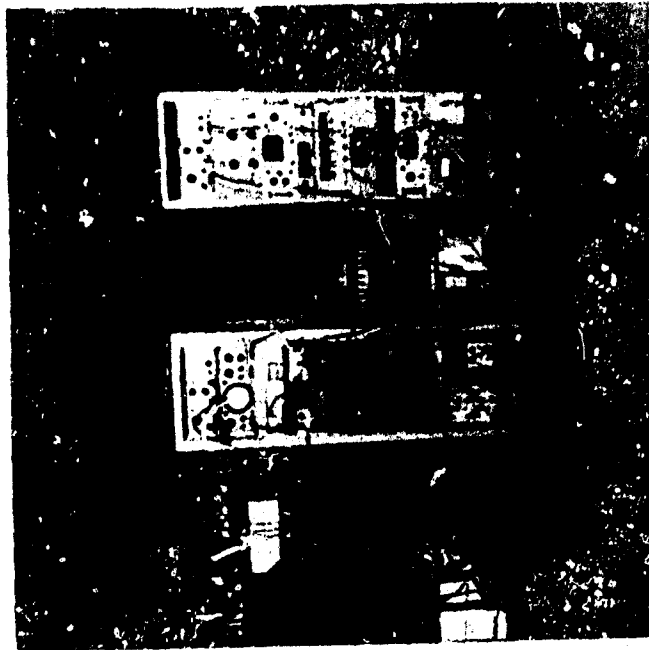


FIGURE 4

Electronic instrumentation

Official Photograph





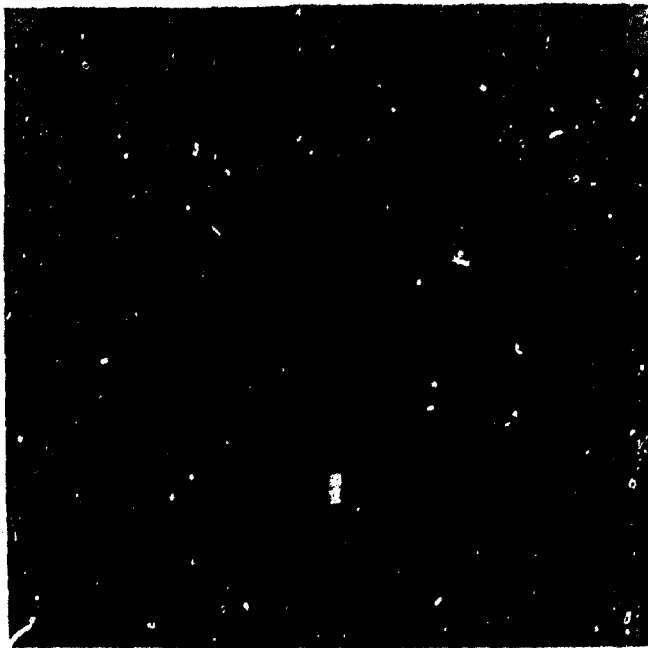


FIGURE 7

Raw acoustic data

Both figures; horizontal scale, 2 milliseconds per division

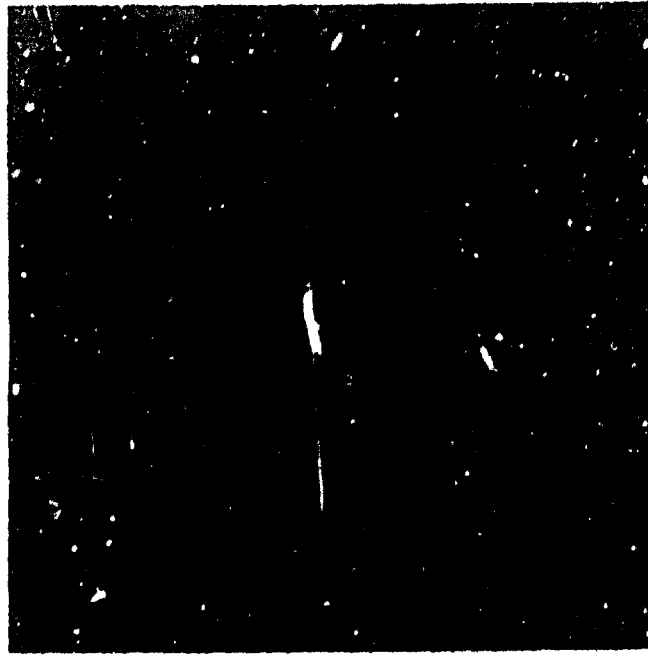


FIGURE 8

Time-filtered acoustic data

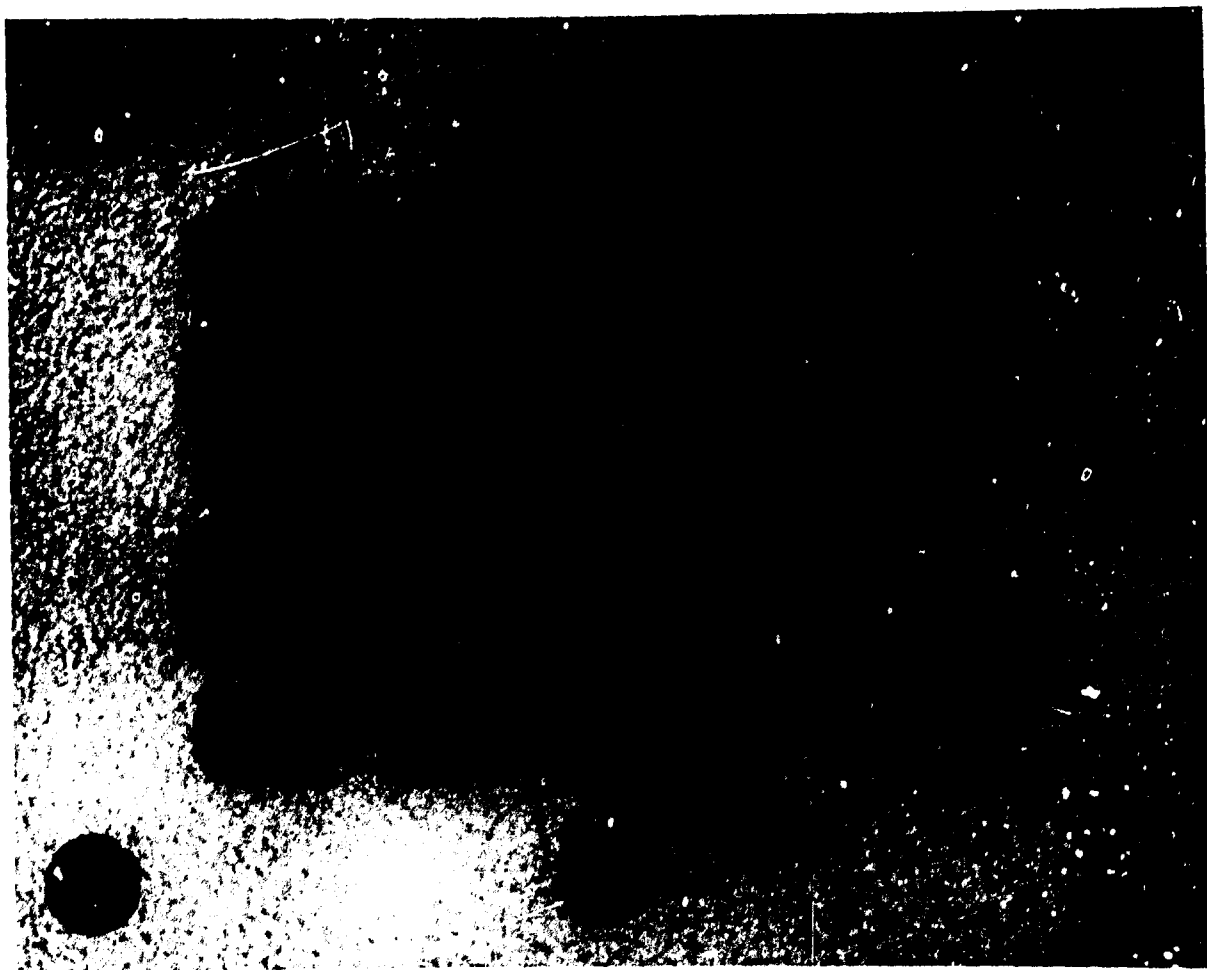


Figure 9 - (5, 5) mode, 9240 Hz, obtained at the water tower

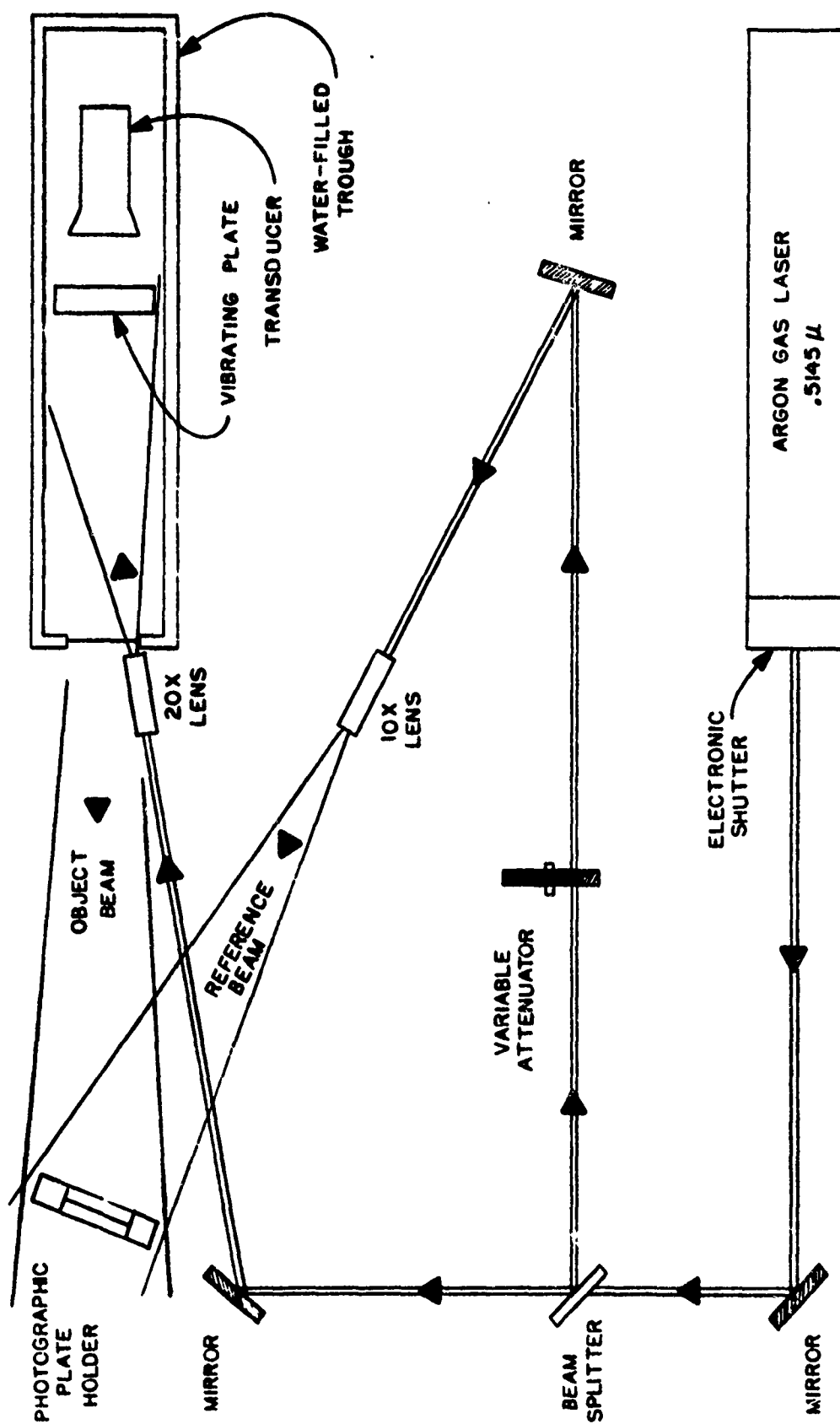


FIGURE 10 -- LABORATORY HOLOGRAPHY ARRANGEMENT

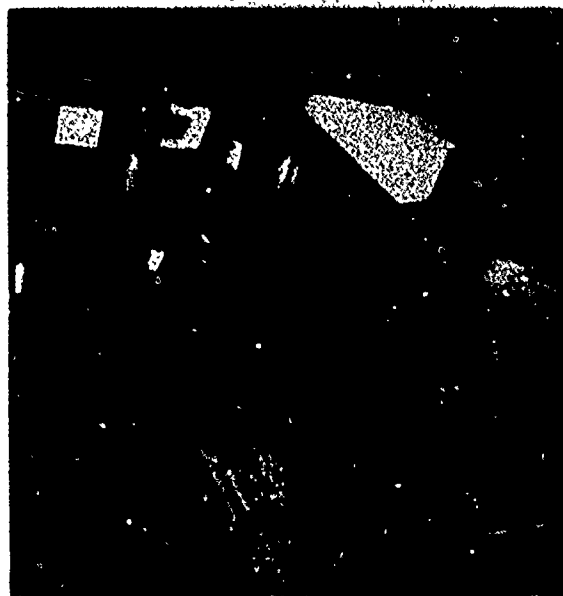


FIGURE 11

Laboratory holography arrangement,  
as viewed from above

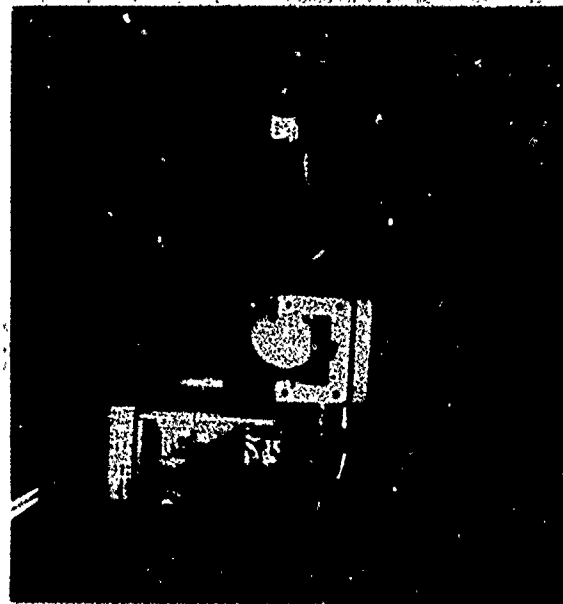
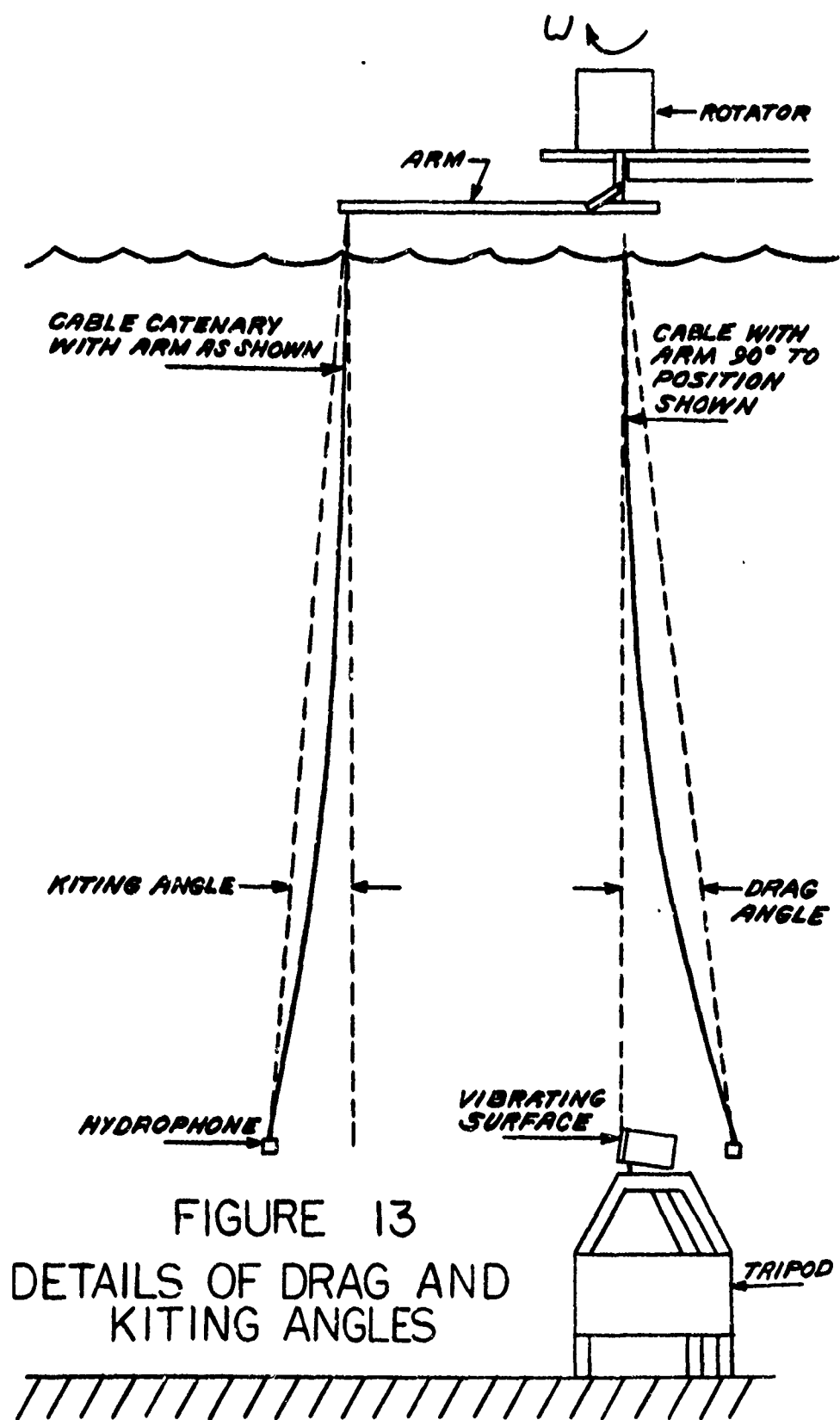


FIGURE 12

View of radiating surface as seen  
through the photographic plate holder

Naval Underwater Systems Center  
NP24 - 47061 - 10 - 72

Official Photograph



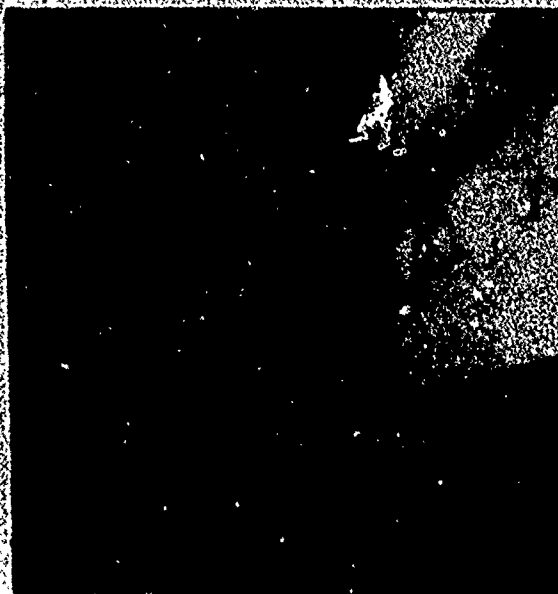


FIGURE 14

Water tower holography arrangement;  
outside of the tower



FIGURE 15

Laser illumination at the radiating surface

Naval Underwater Systems Center  
NP24 - 47063 - 10 - 72

Official Photograph

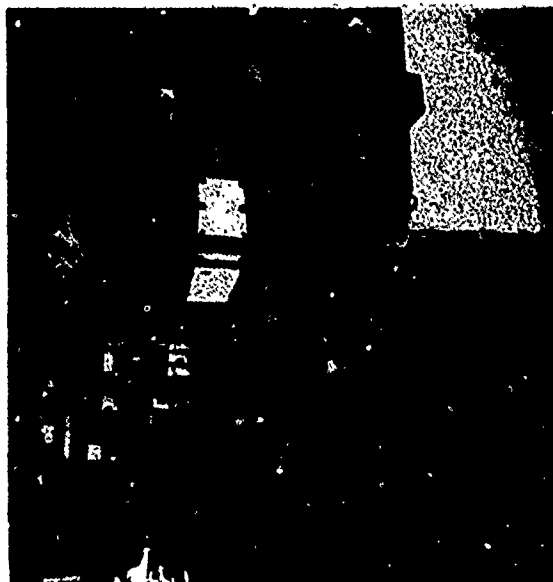


FIGURE 16

Laboratory holographic studies  
using sound box excitation

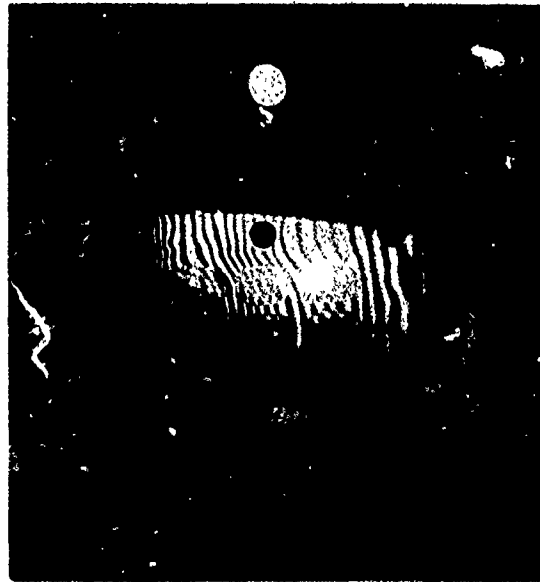


FIGURE 17

Real-time holographic investigation,  
(3, 3) mode

Naval Underwater Systems Center  
NP24 - 47065 - 10 - 72

Official Photograph

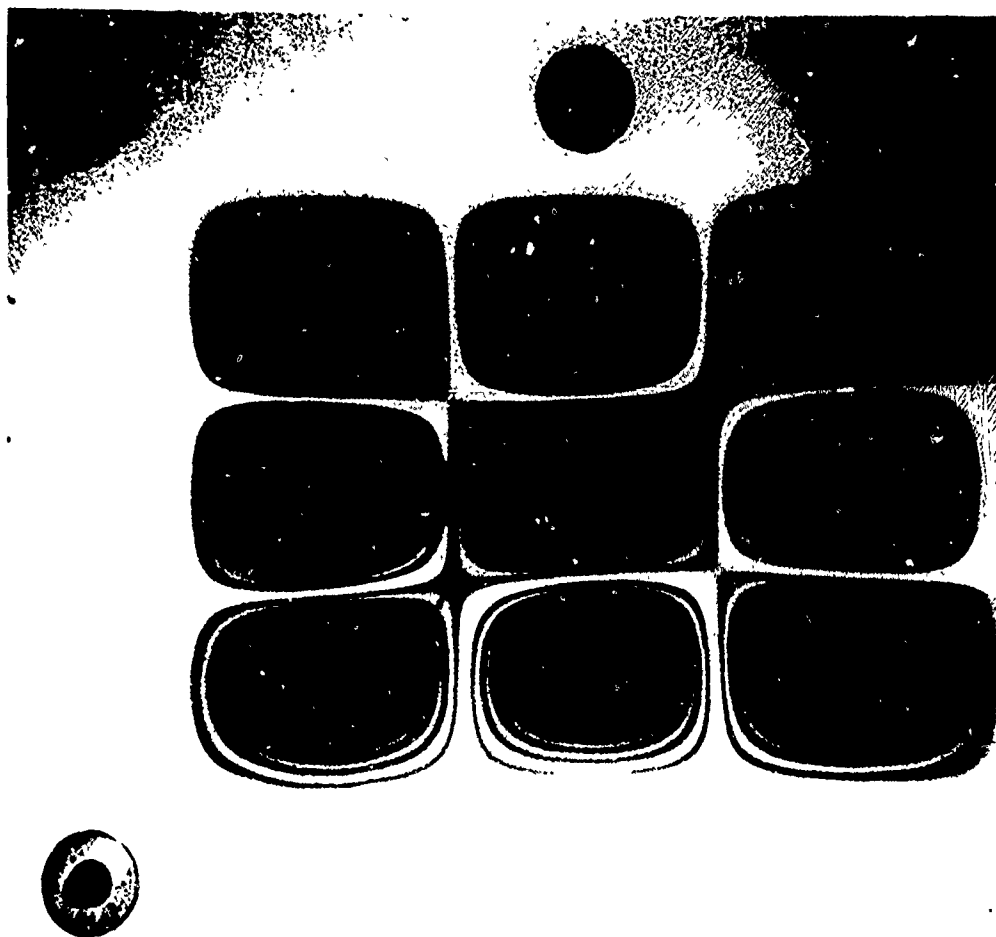


Figure 18 - (3, 3) mode, 3195 Hz, obtained at the water tower



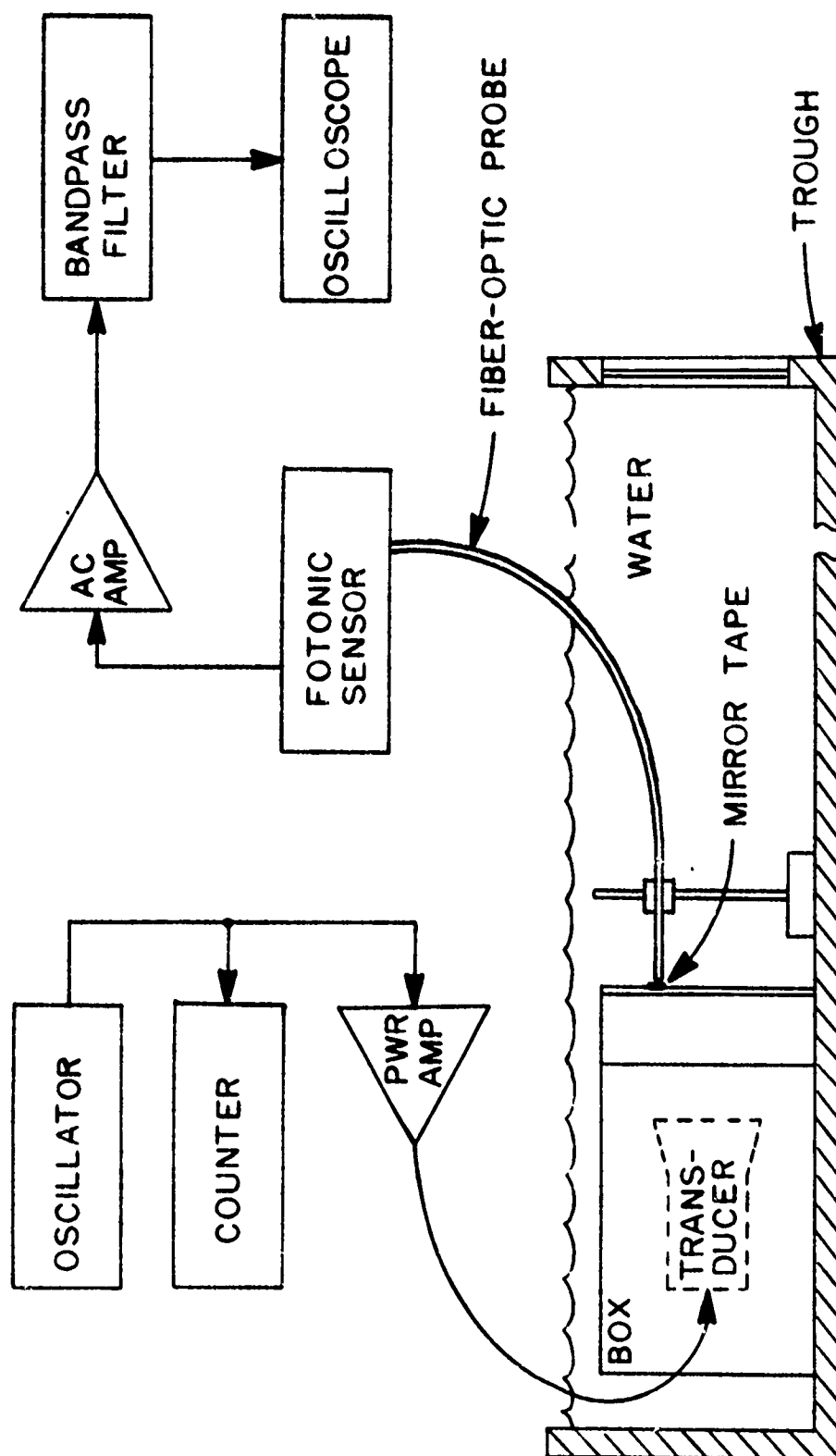


FIGURE 19 -- RESONANCE DETERMINATION USING FIBER-OPTIC PROBE

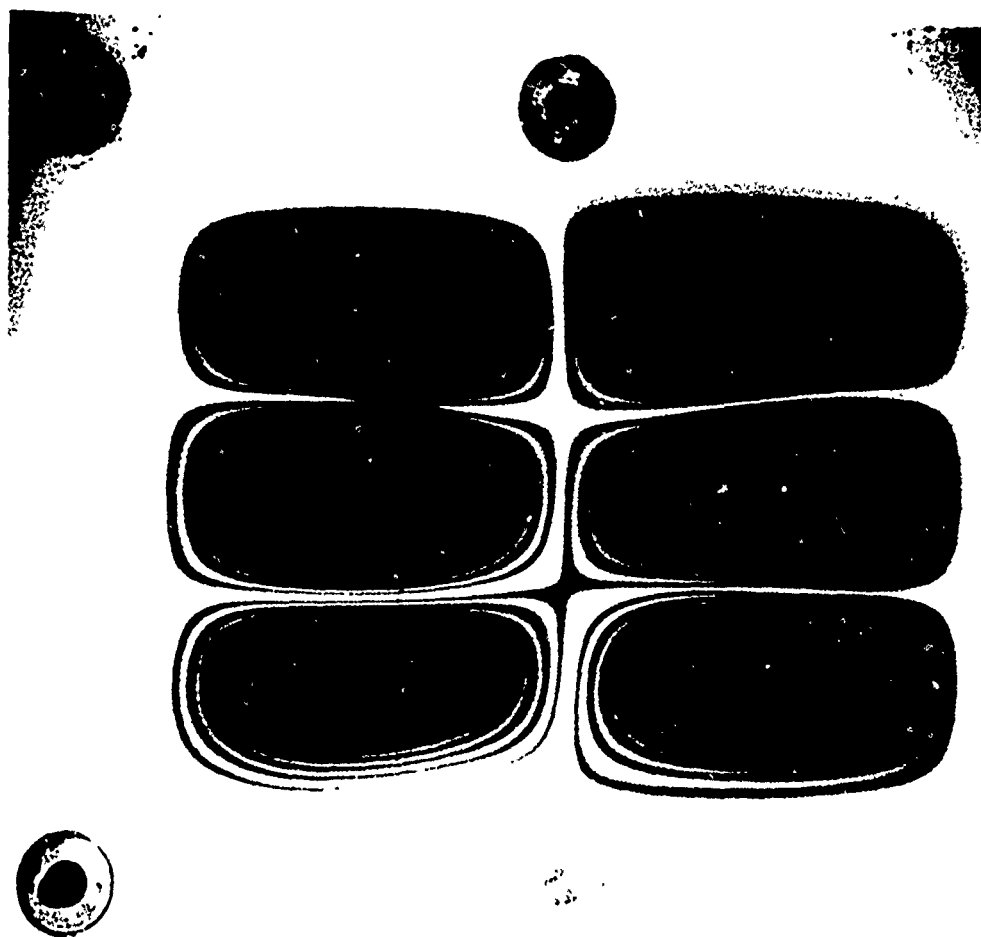


Figure 20 - (2, 3) mode, 2633 Hz, obtained in the Laboratory

Naval Underwater Systems Center  
NP24 - 36662.535A - 1 - 73

Official Photograph

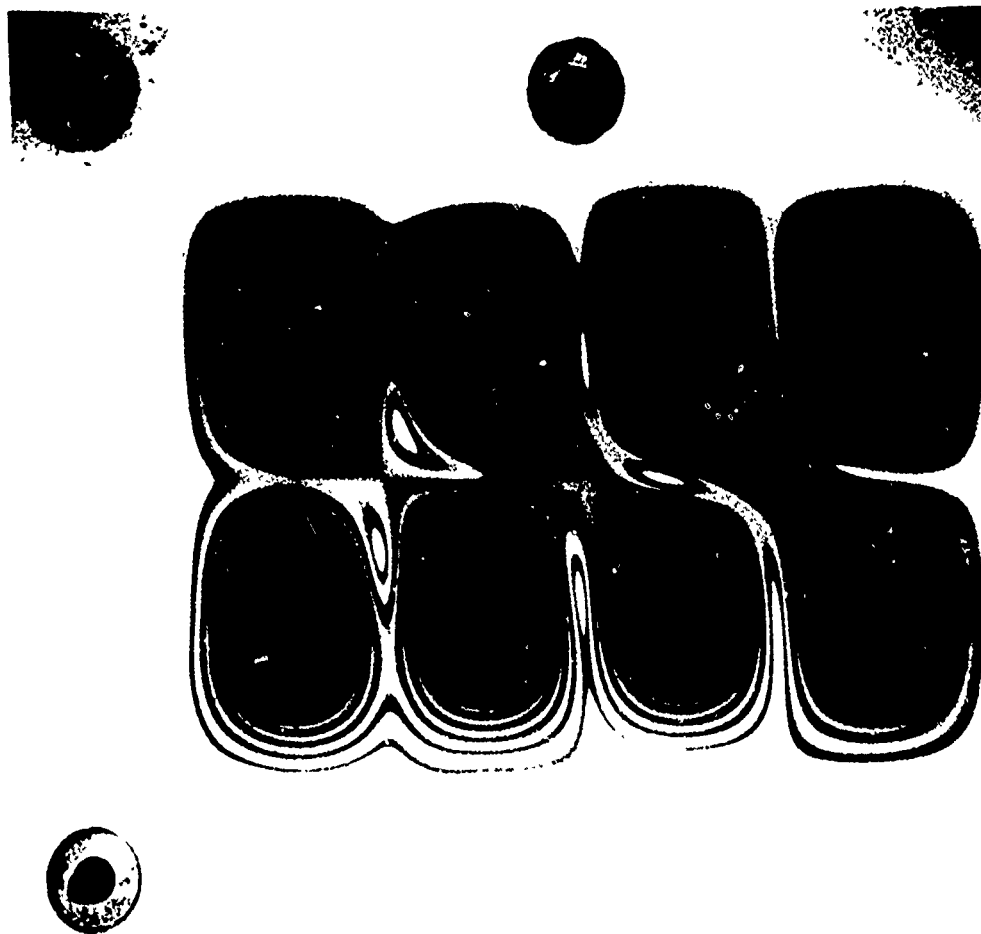
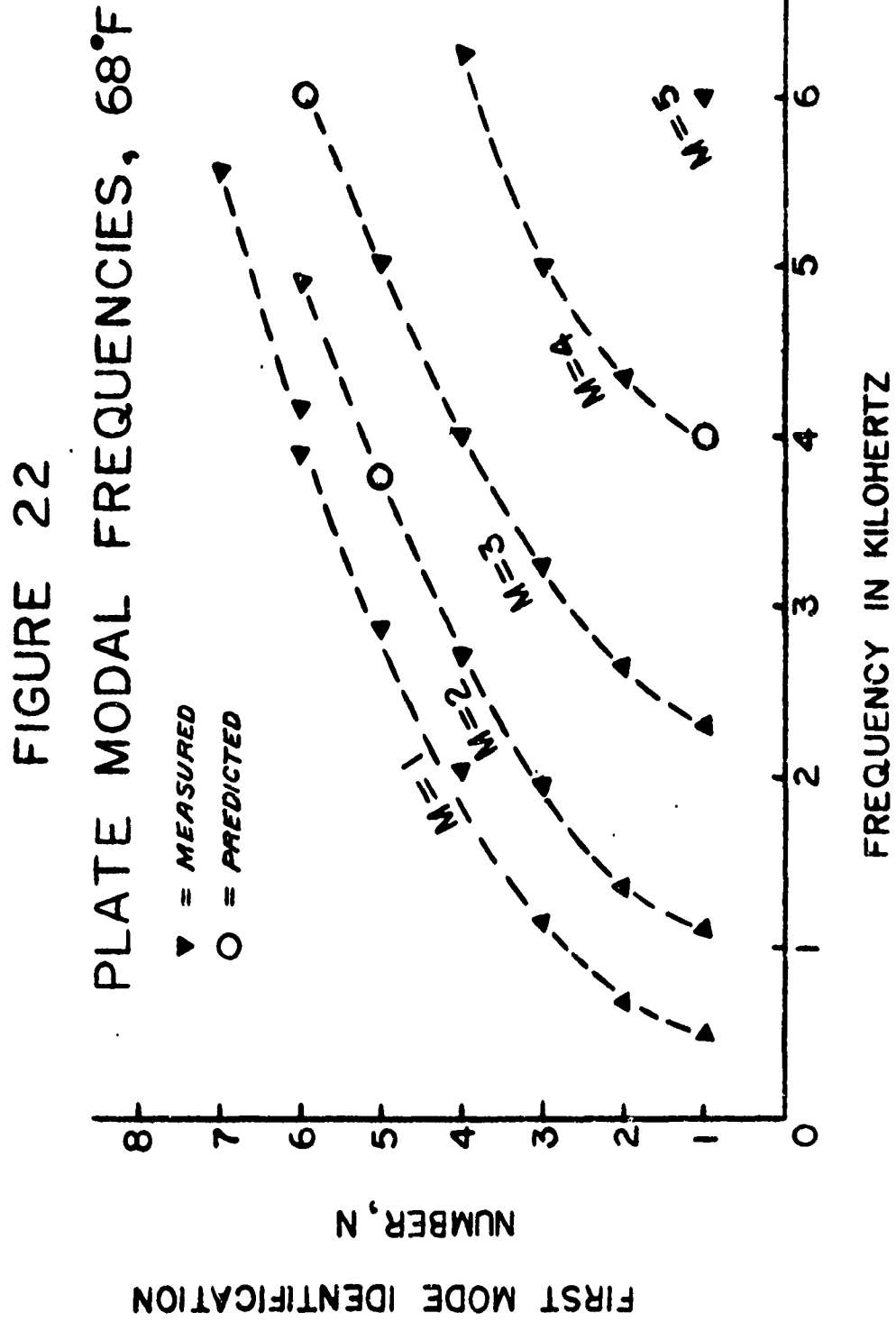


Figure 21 - (4, 2) mode, 2677 Hz, obtained in the Laboratory

Naval Underwater Systems Center  
NP24 - 36662.547A - 1 - 73

Official Photograph



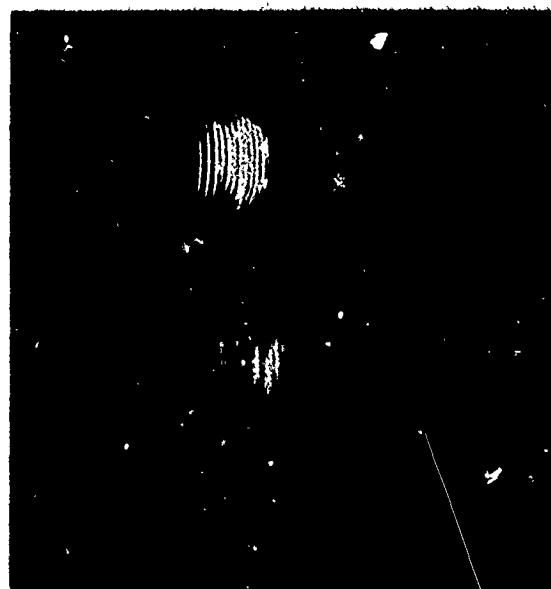
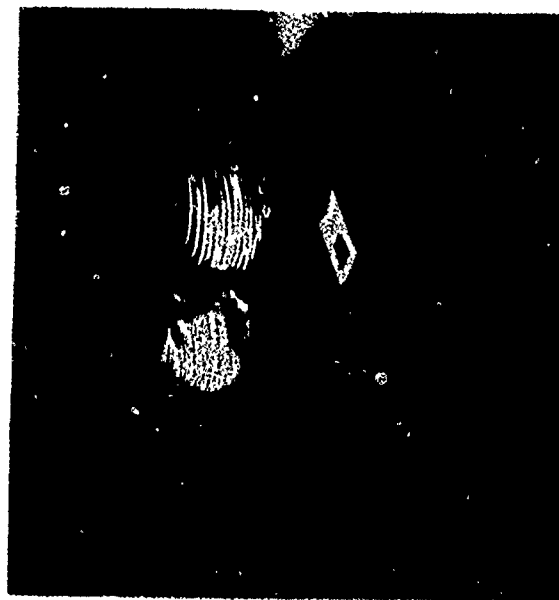
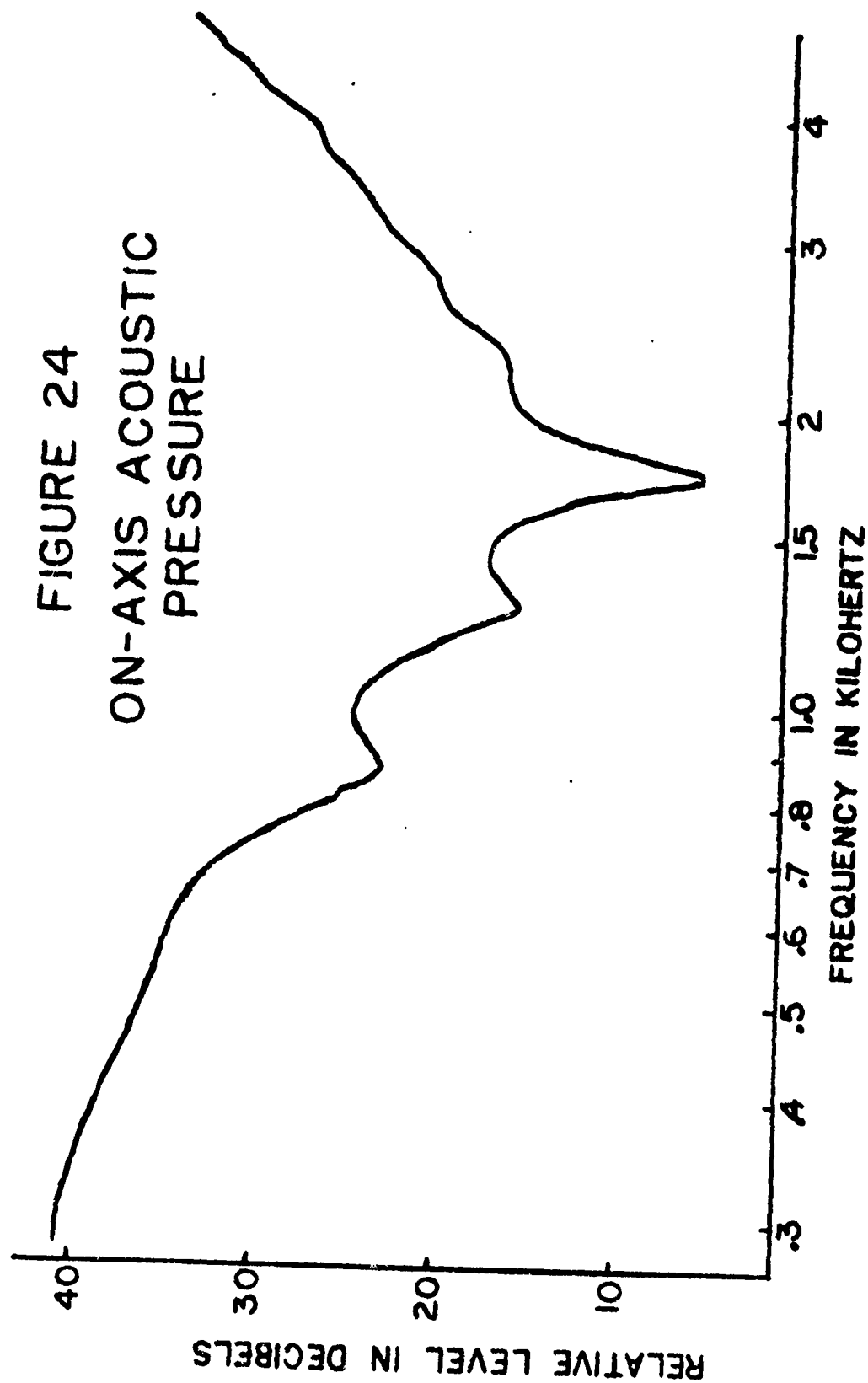


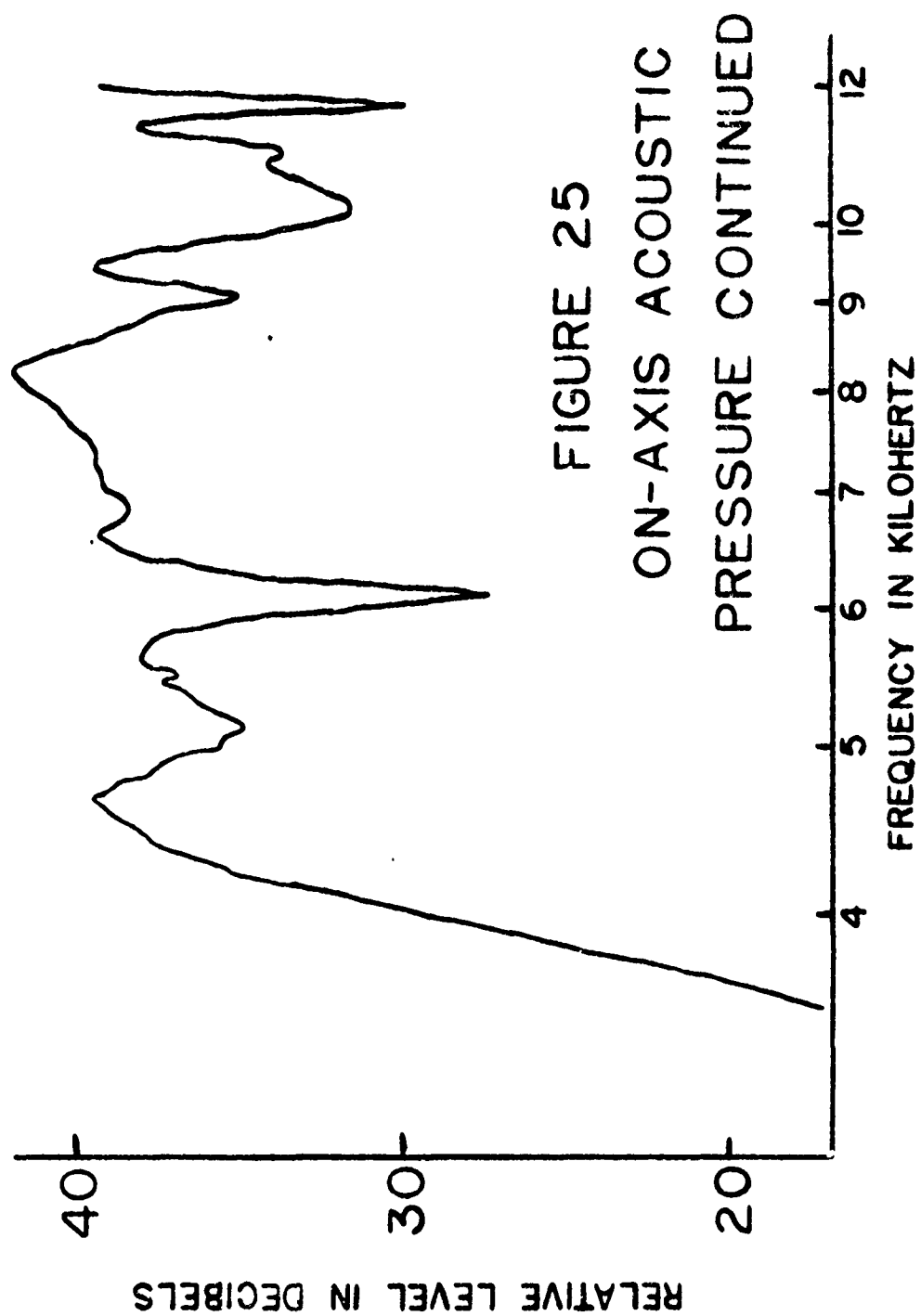
FIGURE 23

Comparison of the acoustic patterns obtained from  
the water tower with those obtained at Dodge Pond

Naval Underwater Systems Center  
NP24 - 47067 - 10 - 72

Official Photograph





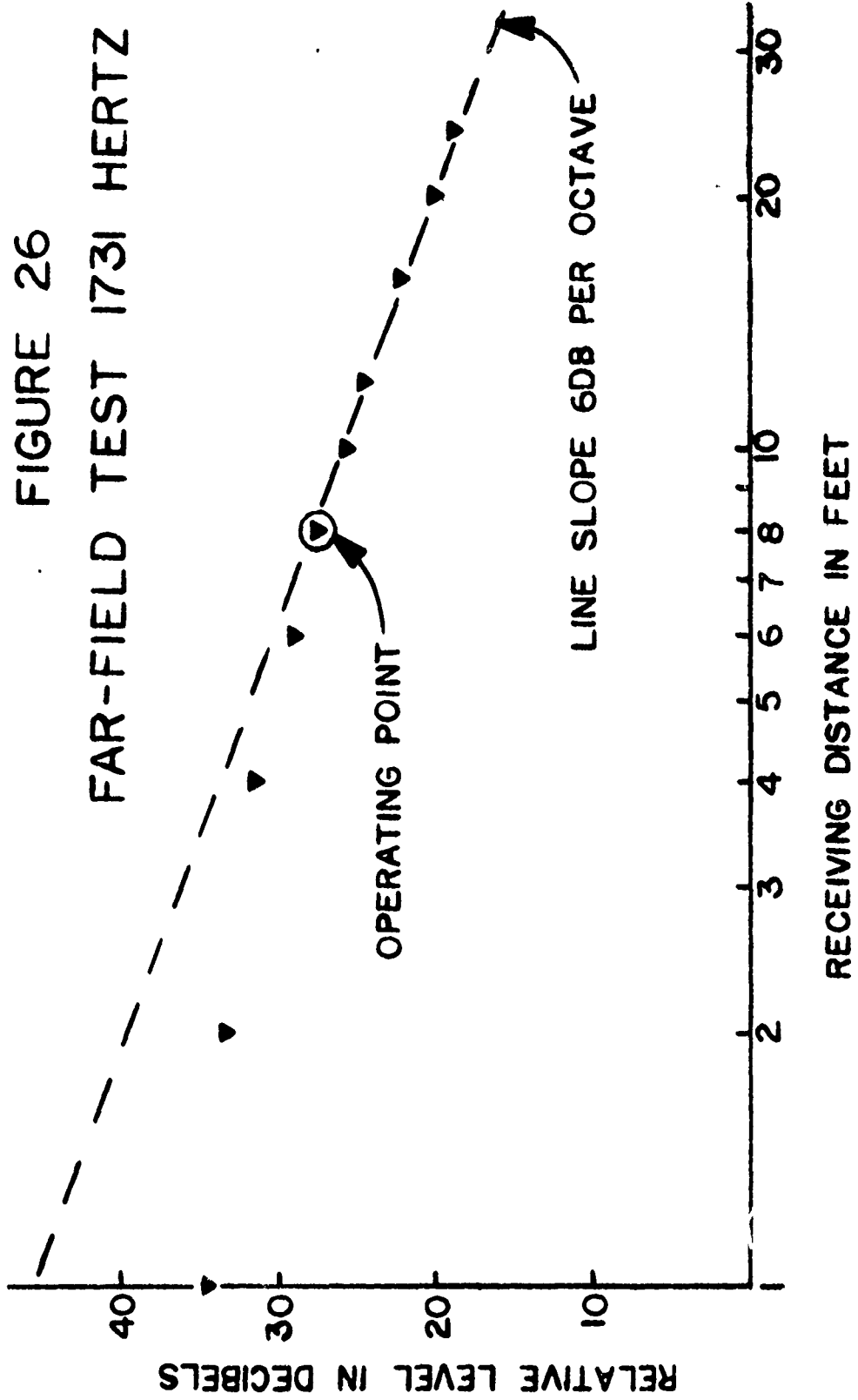
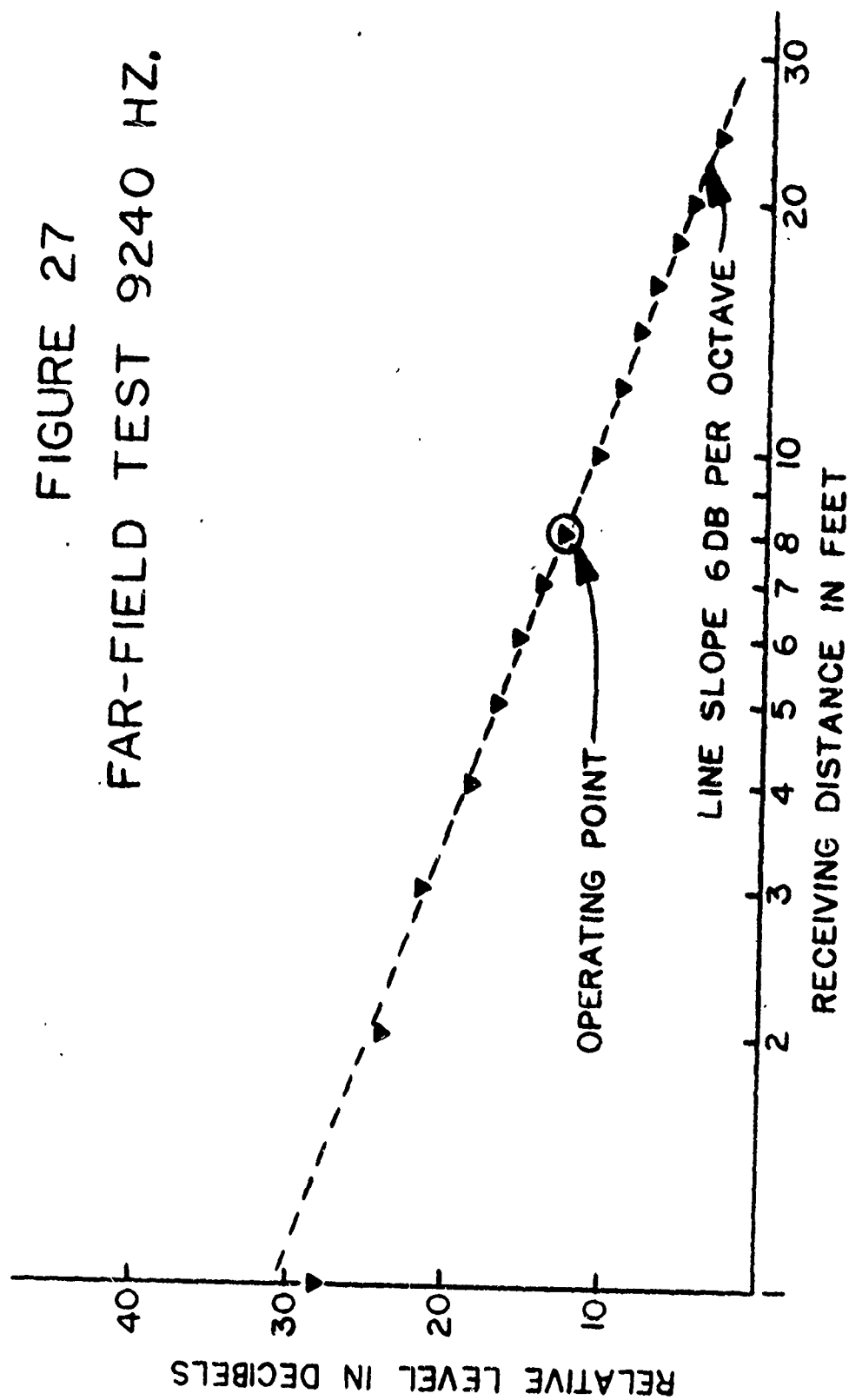




FIGURE 27  
FAR-FIELD TEST 9240 HZ.



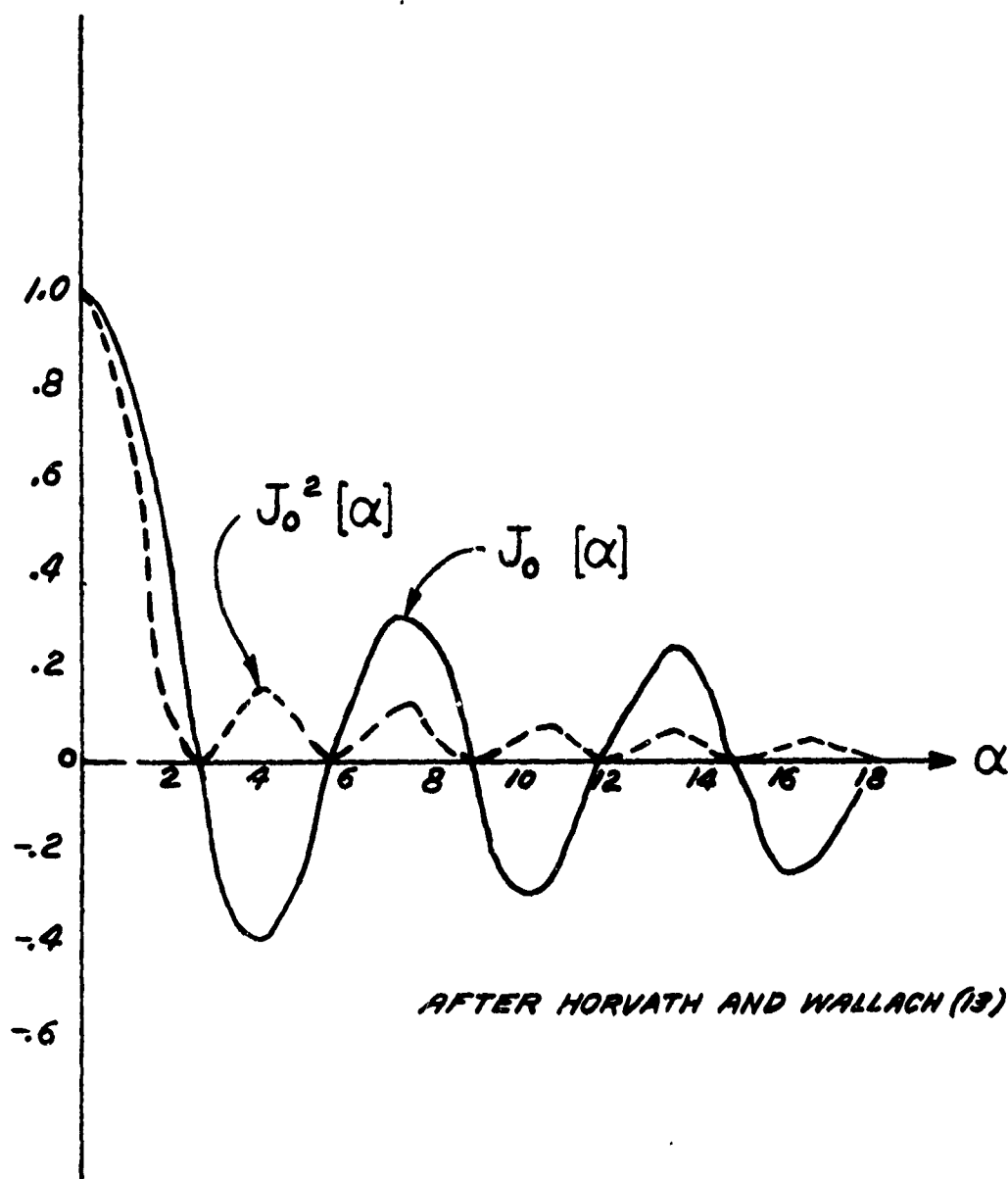


FIGURE 28  
GENERAL SHAPE OF  $J_0[\alpha]$   
AND  $J_0^2[\alpha]$

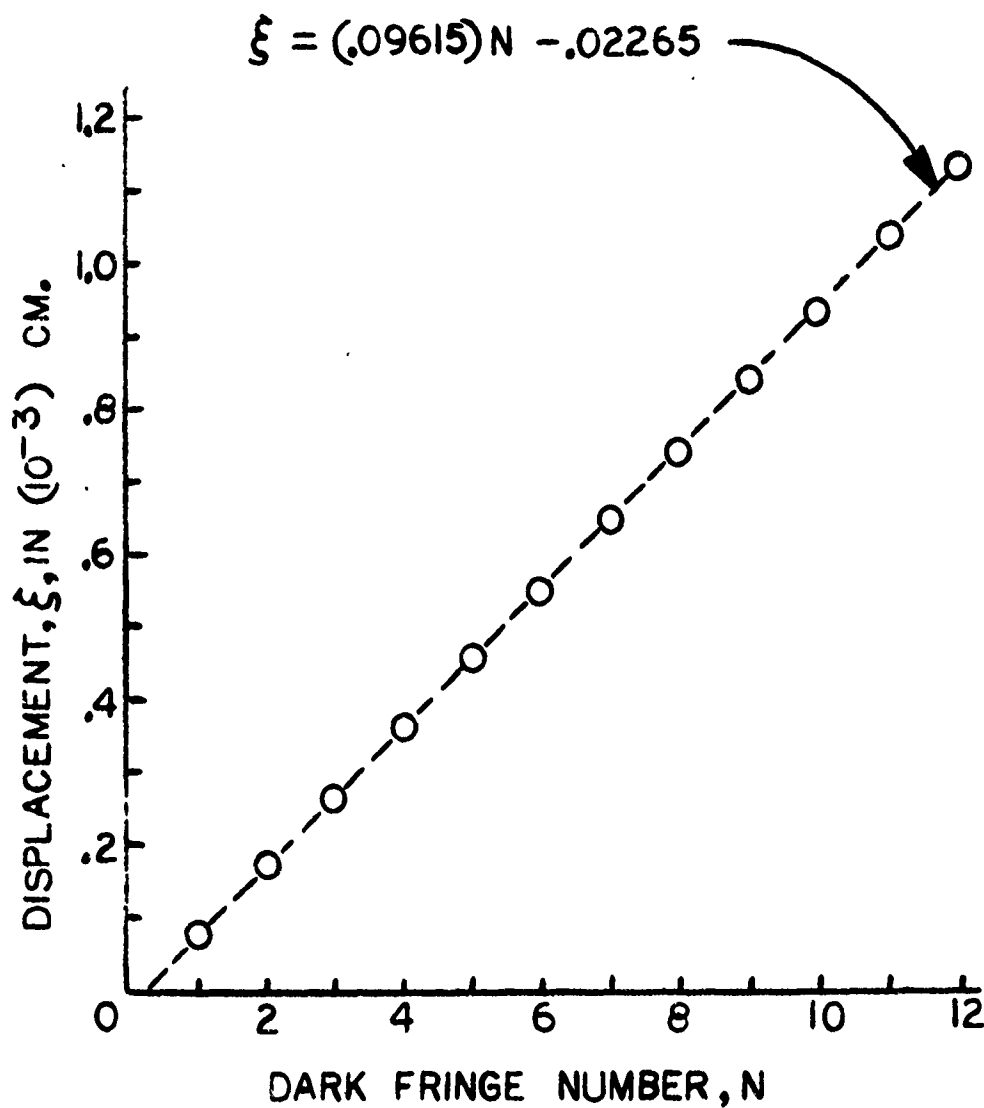


FIGURE 29  
DISPLACEMENT VERSUS  
FRINGE NUMBER

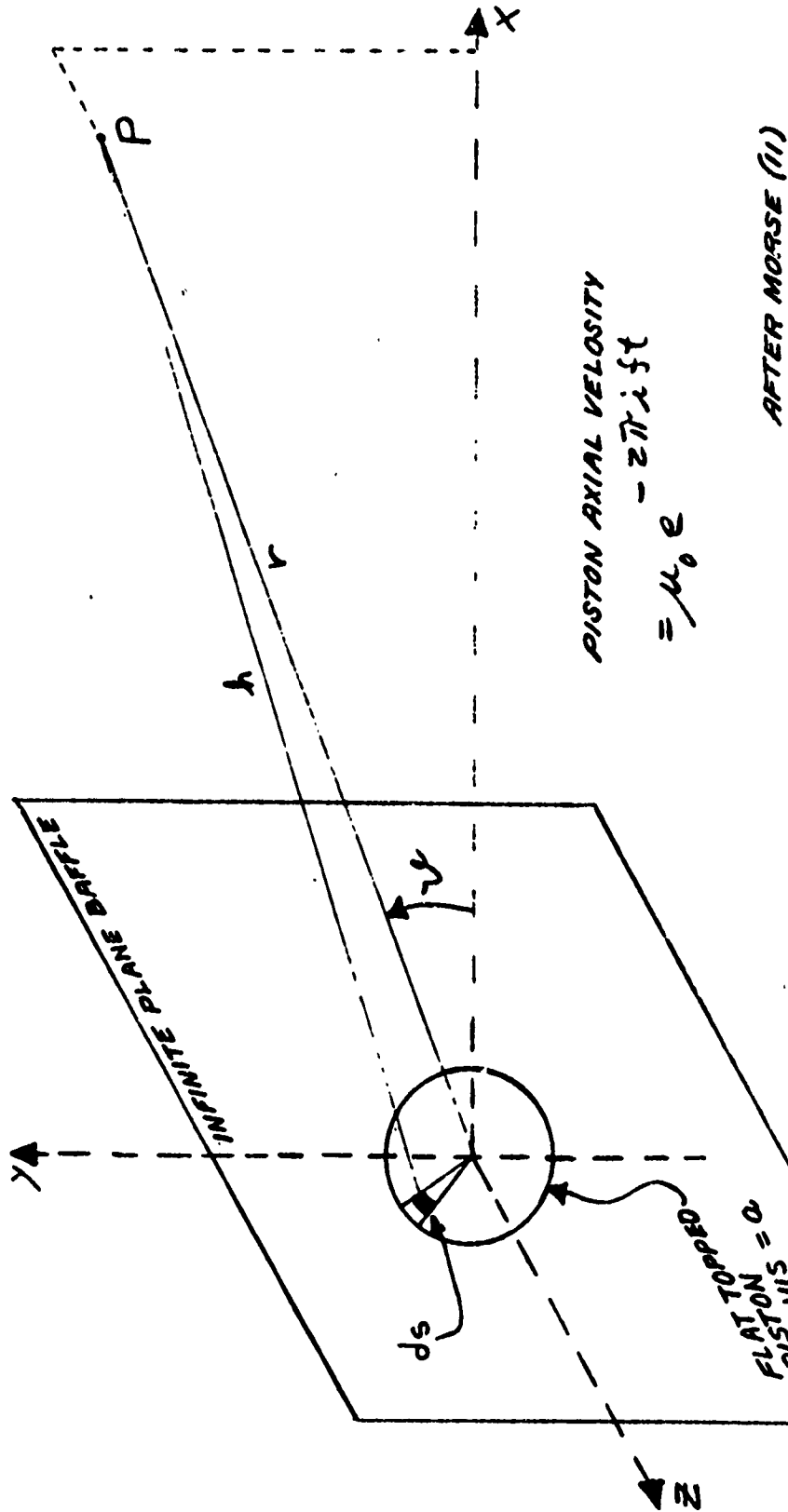
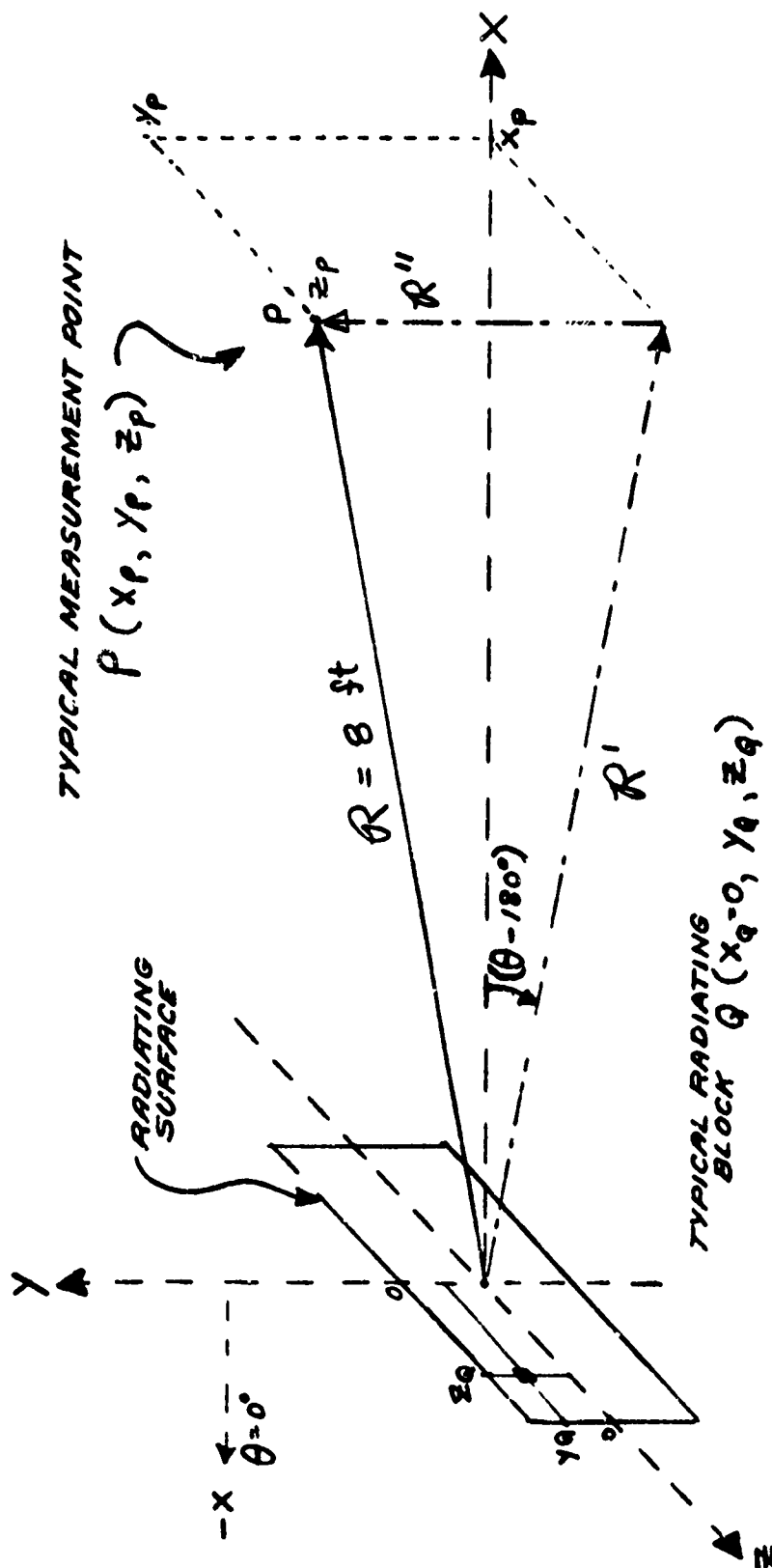
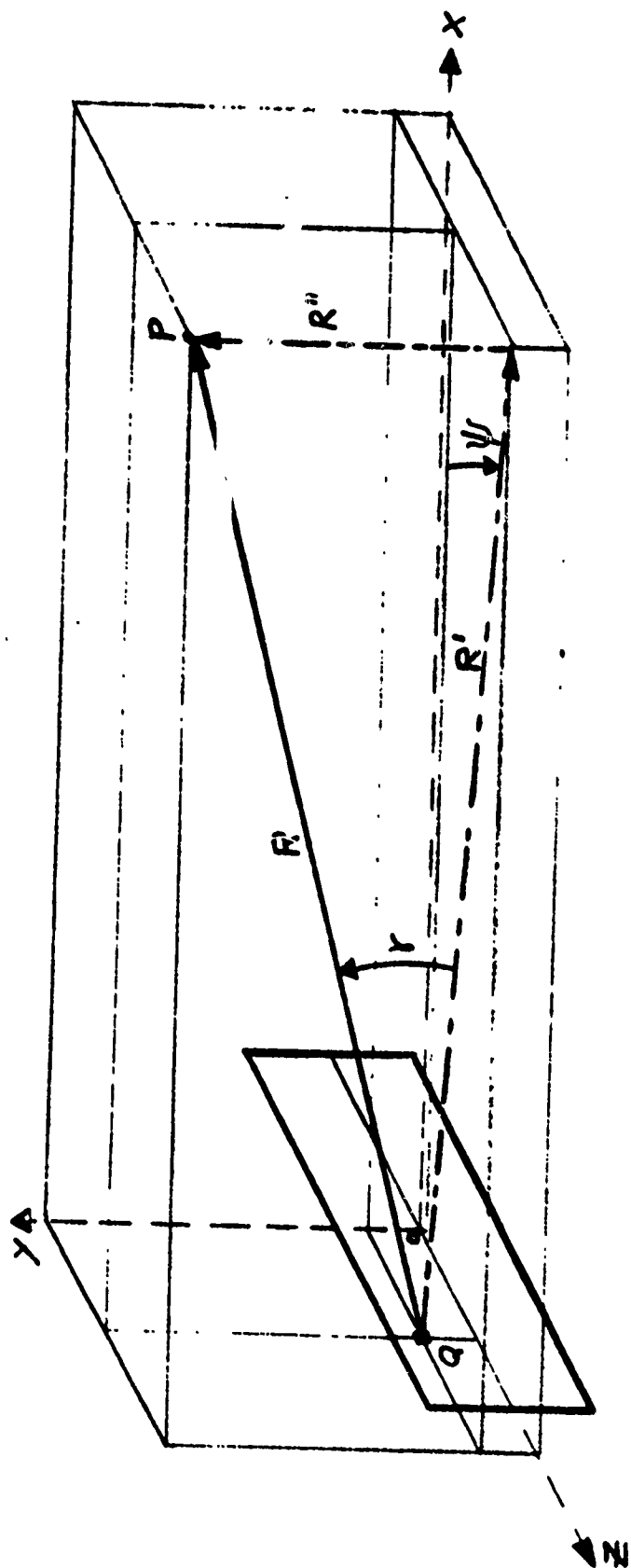


FIGURE 30  
 RADIATION FROM A PISTON SET IN A PLANE WALL

FIGURE 31  
LOCATION OF POINTS P AND Q





MEASUREMENT POINT  $P$  AT  $(x_p, y_p, z_p)$

RADIATING BLOCK  $Q$  AT  $(x_q = 0, y_q, z_q)$

$$\gamma = \sin^{-1} \left[ \frac{y_p - y_q}{R} \right] ; R' = [(x_p)^2 + (z_p - z_q)^2]^{1/2}$$

$$\psi = \sin^{-1} \left[ \frac{z_p - z_q}{R'} \right] ; R = [(x_p)^2 + (y_p - y_q)^2 + (z_p - z_q)^2]^{1/2}$$

FIGURE 32  
RESOLUTION OF THE VECTOR  $R$

$$\begin{aligned} d\phi_y &= d\phi \sin \gamma \\ d\phi'_y &= d\phi \cos \gamma \end{aligned}$$

$$\begin{aligned} d\phi_x &= d\phi' \cos \psi \\ d\phi_z &= d\phi' \sin \psi \end{aligned}$$

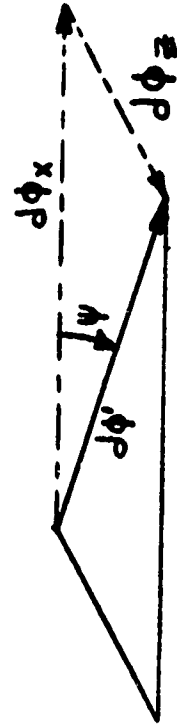
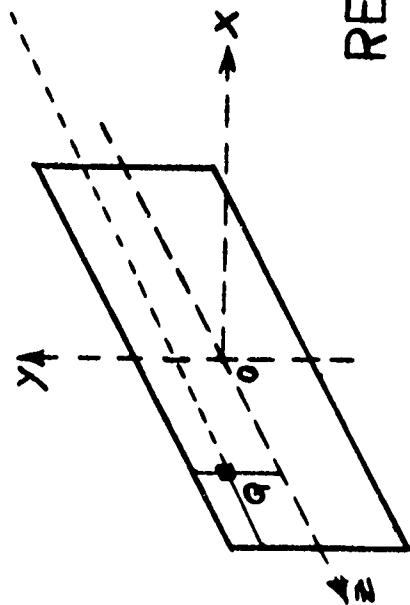
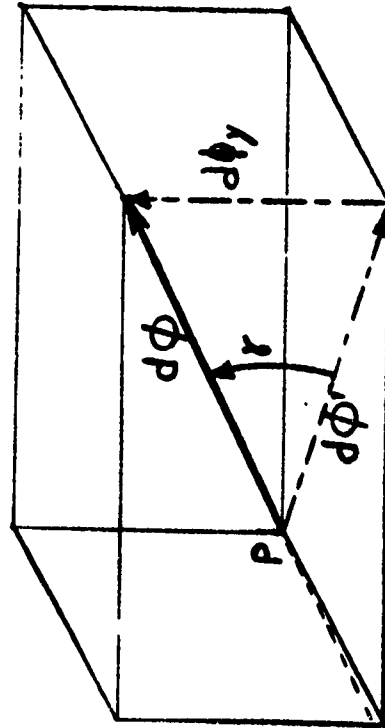


FIGURE 33  
RESOLUTION OF THE VECTOR  $d\phi$

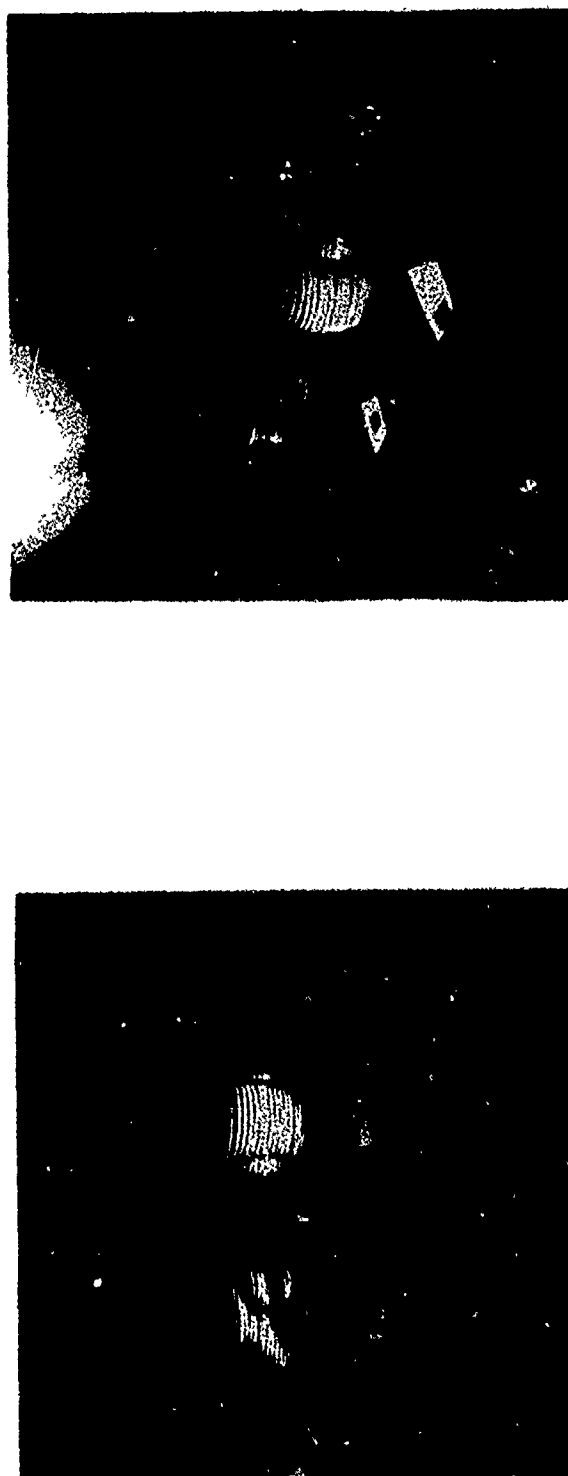


FIGURE 34

Comparison of the acoustic patterns predicted from the holographic data  
with those predicted by plane-wave behavior of the radiating surface

Naval Underwater Systems Center  
NP24 - 47069 - 10 - 72

Official Photograph



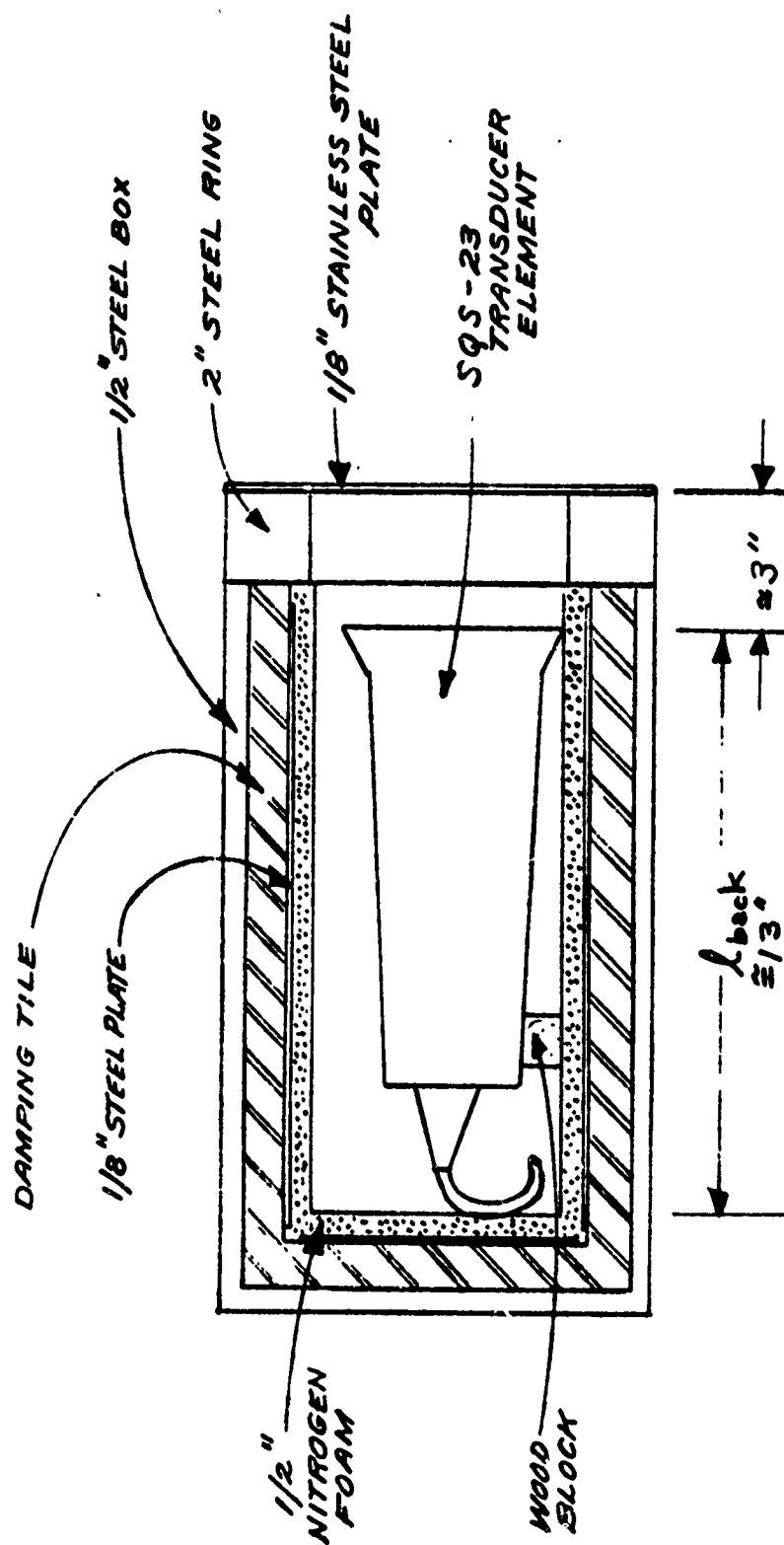


FIGURE 35  
DETAILS OF THE SOUND BOX

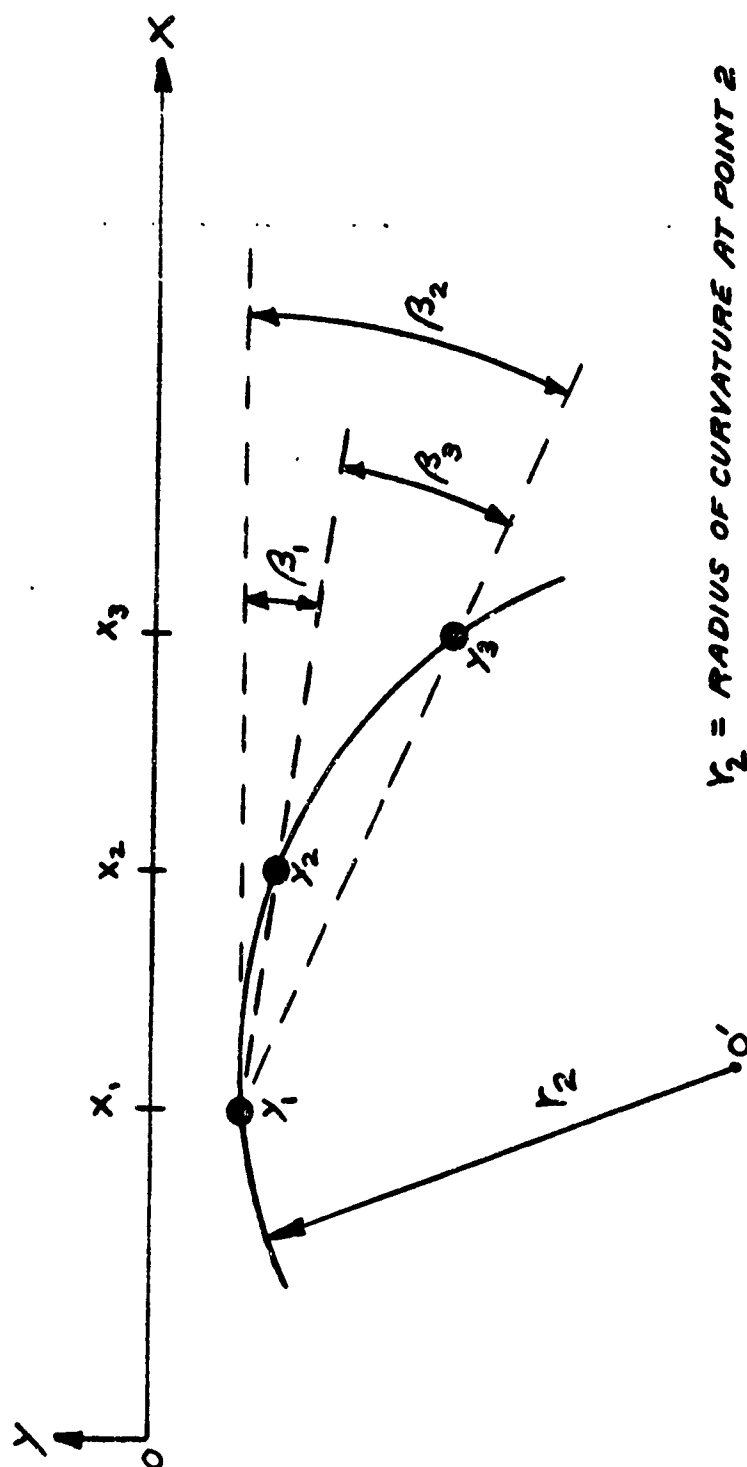


FIGURE 36  
GEOMETRY OF  $\beta_1$ ,  $\beta_2$ , AND  $\beta_3$

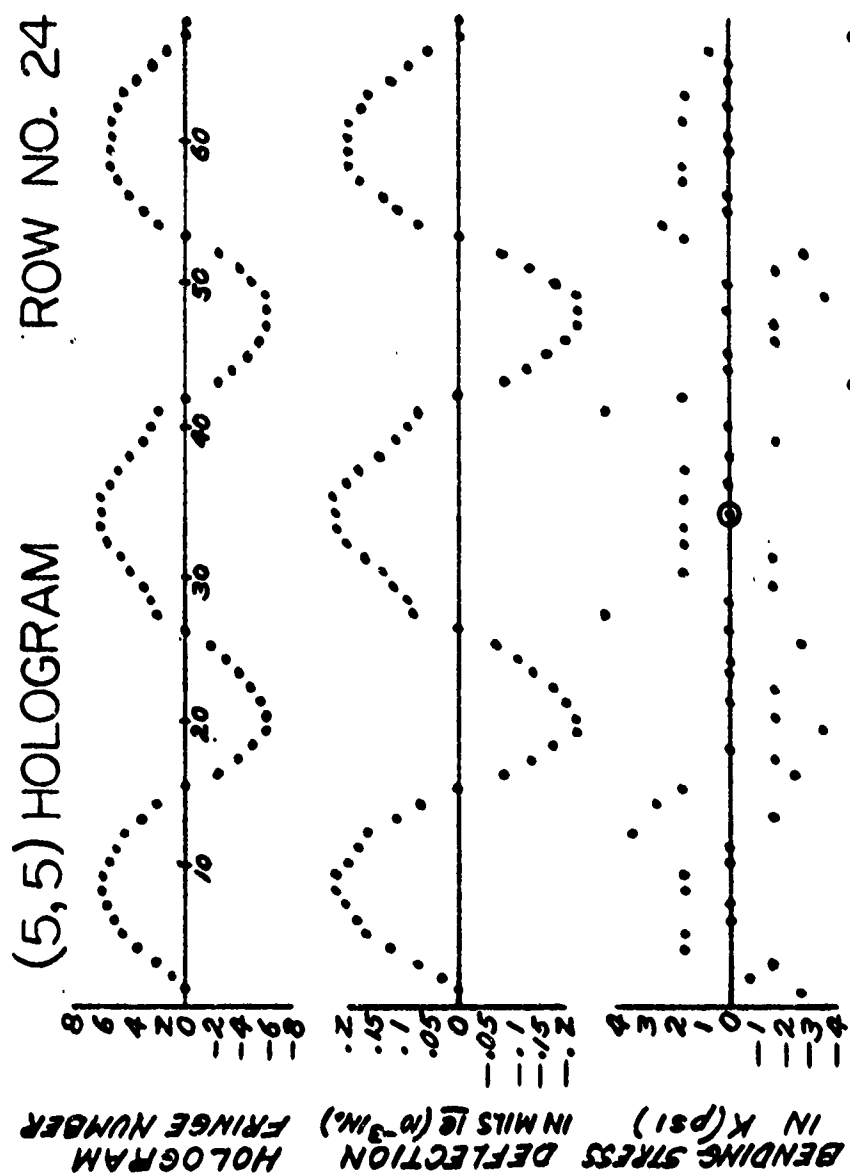


FIGURE 37  
BENDING STRESS ACROSS ROW 24

(5, 5) HOLOGRAM COLUMN NO. 34

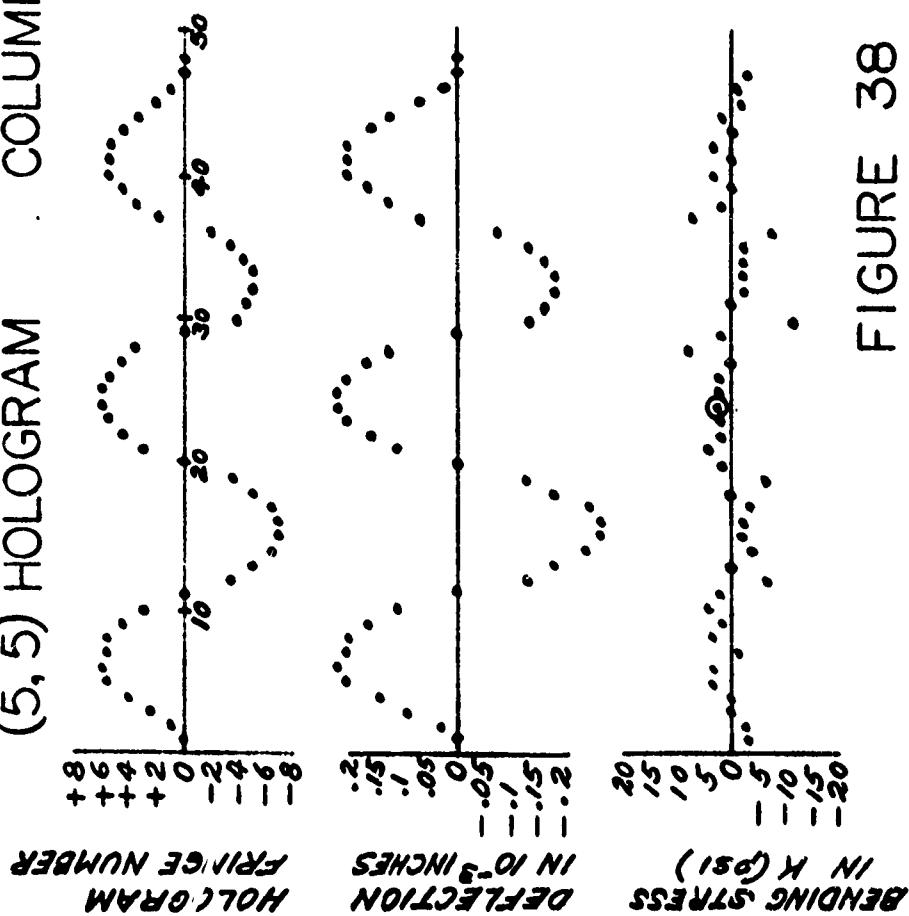


FIGURE 38

BENDING STRESS DOWN COLUMN 34